2019

Ultrafast infrared spectroscopy of nitrous oxide as a probe in salt water and supercritical sulfur hexafluoride

BOSTON UNIVERSITY

GRADUATE SCHOOL OF ARTS AND SCIENCES

Dissertation

ULTRAFAST INFRARED SPECTROSCOPY OF NITROUS OXIDE AS A PROBE IN SALT WATER AND SUPERCRITICAL SULFUR HEXAFLUORIDE

by

PARTH P. SHAH

B.A., Boston University, 2012

Submitted in partial fulfillment of the

requirements for the degree of

Doctor of Philosophy

2019

Approved by

First Reader

Lawrence D. Ziegler, Ph.D.
Professor of Chemistry
Professor of Materials Science and Engineering

Second Reader

Shyamsunder Erramilli, Ph.D.
Professor of Physics
Professor of Materials Science and Engineering
Professor of Biomedical Engineering

ACKNOWLEDGEMENTS

I would like to thank Professors Ziegler for providing me with guidance and knowledge in the pursuit of this degree. His insights and questions were invaluable in making me a better scientist and in exploring all that my research had to offer. I would also like to thank Professor Erramilli, whose experimental knowledge and collaborative efforts shaped how I approached problems which I encountered along the way.

Also, I would like to acknowledge all the former group members of the Ziegler and Erramilli group who were my teachers, Jeffery Shattuck, Alket Mertiri, Elsa Abreu. I worked under Jeffrey when I first joined the group, and he taught me most of what I know about optical setups. Alket and Elsa were a large part in passing on helpful hints and giving me a trove of knowledge regarding many different lasers and setups, as well as teaching me patience with the laser and lab.

Current and former members of the Ziegler group also require thanks. Gregory Ng Pack, with whom I developed and carried out most of the research in this dissertation. We spent many late nights together, working on the laser table, MATLAB code, and complaining about the MBTA always being late. Matthew Rotondaro, who joined the lab in the past few years brought a fresh wave of enthusiasm and helped to take some of the pressures off by carrying out the more tedious experiments. Richard Andino was also instrumental in breaking the monotony by sharing his experimental knowledge and trading questions.

I also want to thank all my other friends I have made at Boston University, Chris Wong, who I met through Richard, but quickly became one of my great friends. He was the hit of my wedding, with my family being put into stitches by him. I want to particularly thank Richard, Matthew, Greg, and Chris for attending my wedding and bachelor party, and being my groomsmen. They helped me to loosen up and it was great going to restaurants and bars to relax and unwind during this stressful period of our lives.

I have to give a special thanks to my wonderful wife, Aditi Bhende, with whom I could not imagine my life. Without you, none of this would be possible. You kept pushing me and giving me the strength and motivation to finish this degree through all the setbacks and hard times. You always believed in me and assuaged my worries.

Most importantly, I have to thank my mother and father, whose love, support, and encouragement allowed me to pursue this degree in the first place. While they may not have always understood my research or what the goals were, they were understanding and proud of all that I was accomplishing. I am blessed for having such wonderful parents who have supported my pursuit of knowledge, from undergrad, to this day.

ULTRAFAST INFRARED SPECTROSCOPY OF NITROUS OXIDE AS A PROBE IN SALT WATER AND SUPERCRITICAL SULFUR HEXAFLUORIDE

Boston University Graduate School of Arts and Sciences, 2019

Major Professor: Lawrence D. Ziegler, Professor of Chemistry

ABSTRACT

Different forms of ultrafast spectroscopy, namely two-dimensional infrared spectroscopy (2DIR) and pump probe spectroscopy, are used to determine spectral diffusion, vibrational energy relaxation (VER), and the dynamics of the solvent environments around probe molecules in various solutions. Supercritical fluids are valuable as potential green solvents, so it is important to explore and understand these dynamical processes in these solvents.

Ultrafast pump-probe spectroscopy was used to investigate the VER of nitrous oxide (N_2O) dissolved in water with different concentrations of ionic salts. Chloride salts of different cations were used to determine changes in VER and reorientation anisotropy decay (R(t)) of N_2O as a function of cation. These rates were found to be consistent with the Hoffmeister series trend of structure makers and structure breakers and showed evidence of cation effects on the water hydrogen bonding network beyond the first solvation shell.

Ultrafast two-dimensional infrared (2DIR) spectroscopy of N_2O's asymmetric stretching (ν_3) mode in sulfur hexafluoride (SF_6) gas resulted in rovibrational spectral lineshapes which show complicated behavior compared to 2DIR lineshapes of traditional condensed phase samples. There is an additional antidiagonal features which appears in

the spectra of dense state points. These observed spectra indicate that there is a quasi-free rotor population, which is captured by a model including all 36 possible rovibrational density matrix pathways originating from a specific *J*-level. The decays of these 2DIR spectral features can be attributed to the N_2O and SF_6 collisions, roughly decaying on the scale of one to two collisions.

Further 2DIR spectra were taken of the system in the supercritical regime of SF_6. Even at these supercritical state points, the frequency correlation decay is still on the order of one to two collisions and confirm that an independent binary collision model is sufficient for describing rotational relaxation in these SCF solutions. Pump-probe spectroscopic measurements offer N_2O ν_3 vibrational relaxation timescales ~10 times slower than spectral diffusion dynamics attributable to rotational relaxation. The growth of a "*Q*"-type $1 \leftarrow 0$ ν_3 transition feature in the null region of the mid-IR spectrum is observed with increasing fluid density. Analysis based on these 2DIR results indicates this feature is a sign of liquid-like character in these solutions and that both hindered and quasi-free rotors exist in the same solvent environment in the dense and supercritical N_2O – SF_6 solution. This experimental methodology enables future lineshape studies on the effects of solvent interactions on vibrational and rotational relaxation rates, dynamics from non-equilibrium states at high temperature and pressures, and critical point solvation dynamics.

TABLE OF CONTENTS

Acknowledgements iv

Abstract vi

Table of Contents viii

List of Tables x

List of Figures xi

List of Abbreviations xiv

1. N_2O as a Probe for Pump-probe and Two Dimensional Infrared Spectroscopy: Aqueous Solution and Supercritical Fluid Dynamics 1

1.1 Introduction 1

1.2 General Experimental Setup and Notes 3

2. Structure Making and Breaking Effects of Cations in Aqueous Solution: Nitrous Oxide Pump-Probe Measurements 16

2.1 Introduction 16

2.2 Experimental 26

2.3 Results and Discussion 29

2.4 Conclusion 42

3. Ultrafast Two-Dimensional Infrared Spectroscopy of a Quasifree Rotor: *J* Scrambling and Perfectly Anticorrelated Cross Peaks 61

3.1 Introduction 61

3.2 Experimental 62

3.3 Results and Discussion 64

3.4 Calculation of Ro-vibrational Response Functions 72

3.5 Conclusion 80

4. Two-dimensional Infrared Spectroscopy from Gas-Phase to liquid-phase: *J*-scrambling, Vibrational Energy Relaxation, and the Onset of Liquid Character 102

4.1 Introduction.....102

4.2 Experimental.....110

4.3 Results and Discussion 114

4.4 Conclusion 129

References.....145

Curriculum Vitae 174

LIST OF TABLES

Table 2.1: Some physical macroscopic properties of aqueous ions 59

Table 2.2: Observed N_2O v_3 parameters in 2M salt solutions and pure H_2O 59

Table 2.3: N_2O v_3 lifetimes and gaussian parameters in 2M salt solutions 60

Table 2.4: Best fit gaussian parameters for concentration dependent $MgCl_2$ 60

Table 3.1: Summary of 2DIR experimental and calculation parameters.....95

Table 3.2: List of transition frequencies for each of the 36 pathways in Fig. 3.8.....96

Table 3.3: List of transition dipoles for each of the 36 pathways in Fig. 3.8 97

Table 3.4: List of unique dephasing functions 99

Table 3.5: Numerical values of parameters used in calculations 101

Table 3.6: Parameters used in calculation of the hard sphere collision times 102

Table 4.1: Rotational equilibrium times determined by 2DIR CLS and Z_{rot}.....143

Table 4.2: N_2O ν_3 VER kinetics determined by fits 143

LIST OF FIGURES

Figure 1.1: Experimental optical layout for pump probe and 2DIR 14

Figure 1.2: Example interferogram of a 2D echo coherence 15

Figure 2.1: Absorption spectra of neat water and semilog absorption of water.....47

Figure 2.2: Absorption spectra of N_2O asymmetric stretch of 2M salts in H_2O 48

Figure 2.3: Pump probe decays of N_2O v_3 in 2M salt solutions 49

Figure 2.4: Gaussian fits to the bend-libration combination of 2M salt solutions.....50

Figure 2.5: Comparison of rates, gaussians, and continuums of salt solutions.....51

Figure 2.6: Rotational anisotropy measurements of N_2O in 2M salt solutions 52

Figure 2.7: Normalized absorption spectrum of OH stretch in 2M salt solutions.....53

Figure 2.8: FTIR spectrum of the bend-libration region of 2M salt solutions.....54

Figure 2.9: Gaussian fitting to the bend-libration combination bend 55

Figure 2.10: Absorption spectrum as a function of concentration of $MgCl_2$ 56

Figure 2.11: Gaussian fitting of the different concentrations of $MgCl_2$ in H_2O.....57

Figure 2.12: Comparison of gaussian parameters in salt solutions 58

Figure 3.1: FTIR of observed and calculated N_2O in $\rho^* = 0.30$ SF_6 82

Figure 3.2: FTIR of observed and calculated N_2O compared to liquid SF_6 83

Figure 3.3: Experimental and calculated 2DIR and CLS Decay of $\rho^* = 0.30$ SF_6 84

Figure 3.4: Experimental and calculated 2DIR of N_2O $\rho^* = 0.16$ and 0.30 SF_6 85

Figure 3.5: CLS Decay of N_2O in $\rho^* = 0.30$ SF_6 86

Figure 3.6: Rovibrational energy levels in each vibrational level 87

Figure 3.7: GSB-SE and ESA pathways 88

Figure 3.8: 36 Rovibrational-specific Liouville pathways 89

Figure 3.9: 2DIR map of the density matrix pathway signals from Fig. 3.3 92

Figure 3.10: Comparison of experimental and calculated peak positions 93

Figure 3.11: Six general type of Liouville pathways 94

Figure 4.1: Normalized absorption spectra of N_2O ν_3 in multiple SF_6 densities 134

Figure 4.2: 2DIR spectra and CLS decays of N_2O in SF_6 at representative waiting times and densities 135

Figure 4.3: Observed CLS decay times and $1/\tau_C$ for all SF_6 densities studied.....136

Figure 4.4: 2DIR spectrum of N_2O in liquid SF_6.....137

Figure 4.5: 2DIR spectra and CLS decays for N_2O in SF_6 at $\rho^* = 0.86$.....138

Figure 4.6: Normalized difference spectra between calculated gas phase and experimental FTIR spectra 139

Figure 4.7: Illustrative representation of the rotational potential barrier 140

Figure 4.8: Vibrational energy level diagram for N_2O and SF_6 for VER.....141

Figure 4.9: N_2O lifetime and bath collisions as a function of SF_6 density 142

LIST OF ABBREVIATIONS

2D ..... Two-Dimensional

2DIR ..... Two dimensional infrared

ATR ..... Attenuated total reflection

BBO ..... β-barium borate

CLS ..... Center line slope

CPU ..... Central processing unit

DAQ ..... Data acquisition

DFG ..... Difference frequency generation

DOPC ..... Dioleoylphosphatidylcholine

DOS ..... Density of states

ESA ..... Excited state absorption

FFCF ..... Frequency-frequency correlation function

FS ..... Femtosecond

FT ..... Fourier transform

FTIR ..... Fourier transform infrared

FWHM ..... Full-width at half maximum

GSB-SE ..... Ground state bleach and stimulated emission

HeNe ..... Helium neon

IR ..... Infrared

IVT ..... Intramolecular vibrational relaxation

MCT ..... Mercury cadmium telluride

MD ..... Molecular dynamics

NIST ..... National Institute of Standards and Technology

NMR ..... Nuclear magnetic resonance

OD ..... Optical density

OH ..... Hydroxide

OKE ..... Optical Kerr effect

OPA ..... Optical parametric amplifier

PE ..... Photon echo

PID ..... Proportional integral derivative

PP ..... Pump-probe

PTFE ..... Polytetrafluoroethylene

SCF ..... Supercritical fluid

SFG ..... Sum frequency generation

Ti:sapphire ..... Titanium sapphire

VER ..... Vibrational energy relaxation

WMEL ..... Wave mixing energy level

Chapter 1: N_2O as a Probe for Pump-probe and Two Dimensional Infrared Spectroscopy: Aqueous Solution and Supercritical Fluid Dynamics

Introduction

Water is one of the most abundant and important substances available in our world. It's role in biological functions has been widely researched and its unique properties are utilized in a many number of ways. Understanding the solvent dynamics associated with supercritical water is crucial for applying it to newer applications, such as chemical reactions, extractions, and as a solvent in manufacturing industries. Supercritical solvents are being utilized more frequently as green solvents since they offer controllable environments for different chemical reactions and applications, while they minimize environmental impact when compared to potentially toxic organic solvents and their waste. Water as a supercritical fluid has vastly changed properties compared to its biological form. In order to study supercritical water, which has a high critical point, in regards to both temperature and pressure, a more accessible supercritical fluid has to be studied to build up to the ultimate goal of studying supercritical water solvation dynamics.

Sulfur hexafluoride, SF_6, is a valuable supercritical green solvent that can be used as a model system for studying supercritical fluid solvation dynamics. It contains no fundamental absorptions in the mid-IR range (1000 cm^{-1} – 4000 cm^{-1}) and has a readily accessible supercritical point (T_c = 45.5°C, P_c = 37 atm). Compared to an atomic solvent, such as Xenon, which has no vibrational modes, SF_6 is of similar size and polarizability,

as well as being cheaper to use, while also being a simple molecule with few degrees of freedom. Nitrous oxide, N_2O, is a simple molecule probe used primarily as a medical anesthetic but has other uses, such as a propellant for dispensing fatty liquids in the food industry, or as a fuel additive in car racing. N_2O is a versatile probe molecule with a small dipole moment (0.16 D) and thus can be used in both polar and non-polar solvent environments. Using N_2O also has other advantages, such as being a strong infrared absorber, having peak shifts depending on solvent environment, and is a linear triatomic molecule, making MD calculations simpler. N_2O has been used in water and octanol as a molecular probe for pump-probe and photon echo studies and shows promise as a supercritical probe in many different fluids because of its ability to report on different solvent environments.

In Chapter 2, ultrafast infrared (IR) pump-probe measurements of the cation effect of chloride salts on the vibrational energy relaxation (VER) of water using N_2O as a probe are described. These effects show how solvent dynamics in water are affected by cations, which were previously thought to not have a significant effect on water dynamics. This can then be used a basis for studies of supercritical fluids (SCF) with dissolved solutes to understand cation and anion effects. In Chapter 3, two-dimensional infrared (2DIR) spectroscopy studies of dense gas phase SF_6 to investigate the solvation dynamics of N_2O. The N_2O behaves as a quasi-free rotor and the resultant perfectly anti-correlated cross peaks from J-scrambling is described. The system is then taken to the supercritical regime at various state points to describe how this J-scrambling behavior progresses through the gas phase, supercritical, and shows onset of liquid-like character.

Experimental Setup and Notes

Ultrafast Spectrometer for IR pump-probe and 2DIR experiments

A Ti:sapphire oscillator (Vitara, Coherent, Inc.) seeds the Ti:sapphire regenerative amplifier (Legend Elite Duo, Coherent Inc), which produces 7 mJ pulses centered at 800 nm with a 35 fs pulse duration at 1 kHz repetition rate. Half of that beam, 3.5 mJ, pumps a TOPAS (Light Conversion) optical parametric amplifier (OPA). Signal and idler beams from the OPA are combined collinearly in a 200 μm $AgGaS_2$ difference frequency generation (DFG) crystal resulting in 80 fs pulses centered at ~2200 cm^{-1} (~4545 nm), with a bandwidth of 300 cm^{-1} and 8-10 μJ of energy.

The beam is directed into the setup through a periscope and then through a zinc selenide (ZnSe) window in order to make the IR beam colinear with the 5 mw helium neon (HeNe), 632.8 nm, beam. This allows for a way to visualize the beam and adjust the setup for the IR pathway. The full 2DIR setup is laid out in **Figure 1.1,** adapted and modified to the setup by Helbing and Hamm.[1] The IR and the HeNe are overlapped by using two irises, near and far, into a single element MCT detector. Once the beams are overlapped, the beam is sent through a telescope to increase the beam size by a factor of 2, from 4 mm to 8 mm, to reduce divergence in the beam and enlarge the beam to allow it to focus to 100 microns at the sample. To focus the beam tightly, the incoming beam needs to be collimated such that the proper flux can be achieved at the sample to perform the experiments. The beam is subsequently split into pump and probe beams using a 1.5° barium fluoride (BaF_2) wedge to prevent spurious back reflections. The power split is about 97:3 pump:probe.

The pump beam is directed into a Mach-Zehnder/Michelson interferometer to produce two interferometrically controlled, colinear pump beams. Two 50/50 beamsplitters are used to create and then recombine the pump beam with equal power. One pathway goes to the Thorlabs DC stage used for scanning the delay between the two 2DIR pump pulses corresponding to the coherence time. The other beam is sent to a stationary arm. The two equal pump beams are then recombined on the second beamsplitter. One side of the output after the second beamsplitter is reflected into a pyroelectric detector (GenTec Inc.) to measure the pump-pump interferometric autocorrelation. The interferometric autocorrelation is used to measure pulse to pulse fluctuations and the Fourier transformed autocorrelation is used to measure the phase and bandwidth of the pulses. The autocorrelation also confirms that the alignment of the two pump beams is maximized by the previously mentioned information. There is a second HeNe beam through the interferometer, raised by ~1 cm, allowing it to follow the same path as the main beam. The HeNe is reflected into a photodiode (DET210) after the second beamsplitter to measure the interference fringes for keeping track of timing, which is needed to properly average each fast scan of the coherence time. A chopper is placed in the stationary arm and all the optics used in the interferometer are 2 inches to accommodate the raised HeNe while keeping the IR beam centered. After the interferometer, the pump beam is sent through a half-waveplate and wire grid polarizer (Thorlabs, Inc.) to ensure proper polarization for the experimental studies. The half-wave plate allows to change the polarization direction of the pump beams without the loss of power. This is later used for polarization dependent studies, such as magic angle,

perpendicular, or parallel polarized pump probes or perpendicular and parallel 2DIR. The beam is then sent down the table and combined on another 2-inch optic to allow for both the pump and probe beam to be sent in parallel into a parabolic gold mirror.

The probe beam is the front reflection from the BaF_2 wedge. The back reflection is blocked, and the front reflection is sent through the probe arm (see Figure 1.1). A UTS50PP linear stepper motor with a minimum step size of 2 fs (0.0001mm) is controlled by an SMC100PP controller (Newport, Inc.) and controls the pulse delay between the second pump pulse and the probe. This is delay time is known as the population or waiting time (T_w). A retroreflector is used on the stage for keeping the beam parallel in and out of the stage. The probe beam is also sent through a half-waveplate and wire grid polarizer (Thorlabs, Inc.) to ensure the beam is polarized vertically (0°) for the experimental studies. A flat CaF_2 window is placed in the path of probe beam to compensate for linear dispersion generated by the BaF_2 wedge in the pump beam. This window is angled such that the autocorrelation of the pump and probe beams is symmetric and short as possible, ensuring that the dispersion is minimized.

The pump(s) and probe beams are both reflected off a 1-inch gold parabolic mirror with a focal length of 4-inches on the sample. A second gold parabola, 2-inches, 4-inch focal length, directs the probe (and signal) beams onto a turning mirror which directs the probe through an f/4, 1-inch lens, into an SP2150i Acton monochromator (Princeton Instruments). The gratings are 150 grooves/mm centered at 4000 nm. The beam is dispersed on a liquid nitrogen cooled MCT 2x32 array detector (Infrared Systems

Development Corp./Infrared Associates). With this system the detection spectral resolution is 4 cm^{-1}.

2DIR Data Collection and Processing

Since the ultrafast setup is in a 2DIR pump-probe configuration, both 2DIR and pump-probe experiments can be carried out without much change to the experimental layout. The key experiments that are carried out are pump-probe, anisotropy measurements, and 2DIR measurements. To determine the pulse lengths, autocorrelations are carried out using the stationary arm of the interferometer and the probe arm. This allows for achieving dispersion balance in the arms and finding time zero for the population time (T_w). The autocorrelation is carried out using second harmonic generation using a Type I ZnGeP crystal. A piece of SiO_2 glass is used in front of the single element MCT detector to block the pump/probe scatter. The SHG autocorrelation is then collected and the CaF_2 flats are adjusted to account for any dispersion effects between the pump and probe arms. A representative autocorrelation scan of the mid-IR pulse is given in Fig 1.2. The autocorrelation is then fit to a typical gaussian beam profile. The temporal pulse duration is then FWHM/sqrt(2). The beam pulse width, after purging the box with N_2O, is ~80 fs. The transform limit for our bandwith of 250 cm^{-1} would be ~60 fs. However, due to the non-linear dispersion added by the crystals in the TOPAS, a completely transform limited pulse cannot be achieved without modification of the OPA, such as thinner and different materials of crystals used to generate the infrared beams. The TOPAS gives a minimum pulse width of 2x the pulse width of the input pump beam from the regenerative amplifier, which is ~40fs, due to limitations of the BBO crystals

used in the TOPAS. The benchmark is to achieve 80 fs pulses based on the input of 40 fs pulses from the regenerative amplifier and then confirm that the pulse bandwidth is wide for the experiments.

To measure the spectral bandwidth, we use an intensity autocorrelation from the interferometer using the pyroelectric detector. This also serves other purposes outside of the intensity autocorrelation. By using the intensity autocorrelation, the center wavelength of the pulse can be accurately determined and the extent of gaseous CO_2 interference in the spectrum before and after purging of the setup box can be measured. It also serves as a measure of how well the mid-IR beams overlap in the interferometer after being combined on the second beamsplitter. The noise in the Fourier transform and fit to a Gaussian pulse both inform on well overlapped the two pump beams are. While the HeNe can also be used to verify the overlap of the two pump arms, the pyroelectric scan gives a more reliable and quantitative way to determine overlap of the two pump arms. The baseline outside of the interferogram was also used to determine the pulse-pulse fluctuations during 2DIR scans by measuring the min and max of the baseline. If the drift or fluctuations are too high in the baseline, then the scans are retaken, as it could indicate bad alignment, outside interference in the room, or some issue in the regenerative amplifier or OPA.

The pyroelectric detector and a photodiode reading the raised HeNe are both connected to the external inputs of the data acquisition box of the multi-array detector. These are then timed with the chopping of the laser pulses by using the output trigger from the regenerative amplifier and integrated over ~500 ns of the response signal. The

raised HeNe is used for timing is thus not chopped, so there is double information to determine the stage timing, allowing for more precise determination of the coherence time. The coherence stage is run from -500 fs to 3500 fs at a speed of 0.6 mm/s. This speed allows for the HeNe to read 3-4 intensity points per fringe to determine the coherence time. To determine accurate stage timing, the HeNe fringes are counted using a peak counting code which uses a delta difference to make sure there are no false positives in the peak counting. While the inflection point/zero crossing is generally better for peak counting, the implemented code is better when the HeNe signal is noisy or weak, resulting in a much more accurate peak counting compared to other schemes. Once the interferogram peaks are found, each peak and the points in between are considered a bin of 2.11 fs, which is the peak to peak time period for the 632.8 nm HeNe wavelength.

Once these bins are created, the signal data and the pyroelectric data are then averaged into each bin based on the data points. This gives the data and pyroelectric scans an inherent resolution of 2.11 fs, which in Fourier space is approximately 4 cm^{-1}. A step scan motor could be used for the coherence stage; however, the collection time would greatly increase. The fast scanning method used here greatly speeds up collection time for each population time, allowing for less impact from power drift and room fluctuations. In junction with the pyroelectric intensity autocorrelation, the phase can also be corrected. Once the autocorrelation is also binned, it can be Fourier transformed to frequency space to determine the bandwidth of the pulse and the phase of the two pump beams relative to one another can be calculated and used for correcting the signal spectrum.

To determine the phase, bins from -25 to +25 around the max of the intensity autocorrelation are taken and the spectra is shifted around the bin. The Fourier transform is then taken and the phase angle is determined. The phase along the spectrum is taken and fit to a straight line. The slope of the line is then recorded. The next bin is then used and the whole process is repeated to get the next slope. The slopes are used to determine when a sign change occurs in the slope. This bin with the absolute value closest to zero around the sign change is then taken to be the center bin. This center bin determines time zero in the coherence delay stage. The value of the phase at the spectrum max is then used as the phase factor for the correction of the spectrum as well as the correction of the signal data. The spectrum of the autocorrelation is then fit to a gaussian and normalized in order to deconvolute the pulse from the signal spectrum for each T_w.

Using the bin for time zero, the echo signal before this time bin is removed and only the positive time raw echo signal is used. Baseline correction is carried out, followed by applying a Hanning window to smooth the ω_1 axis to zero. The smoothed signal, which is given in **Figure 1.2,** is then padded to the nearest power of two and Fourier transformed to give the transformed 2DIR signal. The FT signal is then corrected by the phase factor determined from the autocorrelation and divided through by the autocorrelation spectrum fit also determined earlier to give the deconvoluted signal. This processed spectrum is then saved for each scan. When each scan is processed, they are averaged together. A rolling average is then carried out in the ω_3 axis direction to smooth the data. The averaged spectrum is then normalized to the peak of the 0-1.

Spectroscopic Theory for Third Order Polarization Experiments

The spectroscopic layout is used to carry out two key experiments to investigate the cation and SF_6 studies. Pump-probe (PP) and two-dimensional infrared (2DIR) spectroscopy are both third order polarization spectroscopic techniques. The layout is done in the pump-probe geometry, making it is easy to switch between the two experiments by simply blocking the pump pulse through the coherence stage. Pump-probe (PP) spectroscopy is a third order experiment using two beams but with three field interactions. PP is used to determine the lifetime of excited populations in electronic or vibrational systems. In vibrationally resonant PP, IR pulses are tuned to the frequency of the vibrational mode of interest. The pump pulse creates an excited vibrational population using the two field interactions. The probe pulse then interacts with the sample at a later time delay to report on the remaining population in the excited vibrational state. Two possible interactions can then occur if the sample is still in its excited state in a one color pump-probe measurement. If the probe pulse interacts with the sample and has increased transmission, two processes can be occurring. Ground state bleach (GSB) and stimulated emission (SE) can both account for an increase in transmitted probe power ($-\Delta A$). GSB refers to depletion of photons in the ground state to the excited state, leading to greater transmission. Alternatively, the probe pulse can cause a photon to be emitted via stimulated emission, driving the molecule back to the ground state from the excited state (SE). Both of these processes give a signal with the same sign as they both lead to increased probe transmission.

These interactions only involve the ground state (ν = 0) and first excited state (ν = 1). However, given the small anharmonicity of nearly all vibrational systems, a three level system, which includes the second excited state (ν = 2) is required for one color, ultrafast vibrational studies. Due to anharmonicity, the energy gap between $\nu = 0 \rightarrow \nu = 1$ and $\nu = 1 \rightarrow \nu = 2$ are not exactly the same, with the latter being slightly smaller in most cases. In a perfectly harmonic system the 0-1 and 1-2 signals would cancel each other out since these contributions have opposite sign (emission vs absorption). With the addition of the second excited state, the probe pulse can be absorbed due to the $\nu = 1 \rightarrow \nu = 2$ energy gap which also falls in the ultrafast bandwidth. This IR signal contribution is referred to as excited state absorption (ESA) and has the opposite signal of the GSB-SE signal. Due to the anharmonicity, this signal is also red-shifted (lower energy photons). By using the probe pulse, the fluctuations and decay of the system can be mapped out to determine the lifetime of the excited state (T_1).

While PP experiments are third order, it only employs one time delay. To investigate other dynamical properties of vibrational systems by third-order experiments, two time delays are required. 2DIR is a three-beam, two delay time, third-order polarization experiment. 2DIR allows for processes like spectral diffusion, chemical exchange, and other spectral dynamics to be studied. Spectral diffusion is the effect of solvent fluctuations on the vibrational transition frequency being studied, be it a solute molecule of a probe group on the solvent itself. Spectral diffusion describes dynamics that occur between the two limits of line broadening, homogeneous and inhomogeneous. The homogeneous limit is when the fluctuations are extremely rapid and the lineshape is

motionally narrowed. Typically, the pure dephasing time T_2^*, is extracted from these lineshapes with the width being $1/\pi T_2^*$. The inhomogeneous limit occurs with much slower fluctuations, and is considered a static distribution of frequencies, with the width representing this distribution. Typically, this arises from different structural environments.

Most systems lie between these two limits and so we can study the spectral diffusion of the system based on the lineshape. Each transition frequency being studied evolves over time in the experiment. The evolution of these frequencies is described by the frequency- frequency correlation function (FFCF) which incorporates the Kubo lineshape formalism and is modelled as a sum of exponentials with the functional form:

$$C(t) = \langle \delta\omega(t)\delta\omega(0) \rangle = \sum_{i=1}^{n} \Delta_i^2 \, e^{-\frac{|t|}{\tau_i}} \tag{1.1}$$

where Δ_i is the instantaneous distribution of vibrational transition frequencies and τ_i is the exponential decay correlation time of the *i*th contributing component.

To generate a 2DIR signal in a resonant sample, the three pulse beams have to interact in the sample in a specific order and direction. The first pump pulse excites the molecule into the first excited state, creating a superposition between the ground (ν = 0) and the first excited state (ν = 1). These vibrators all start in phase, dictated by the radiation field. As the system evolves in time, the vibrators begin to diphase and return to their randomized equilibrium. The second pump pulse is time delayed experimentally and applied to the sample at varying times, τ, known as the coherence time. The interaction with the sample in the superposition now crates a population in either the ground or

excited state. If a population is not created by this step, for instance if the superposition is made into a 0-2 superposition, then no population is created and is not a time history relevant to generating a 2DIR signal. Once the population is created, the third pulse, the probe, interacts, again delayed experimentally in time, T, called the population time. The third beam interaction disrupts the population and creates a coherence between the ground and excited states. The third beam also creates an emitted signal during its interaction, which has probed how the system as evolved over the coherence time for that specific population delay. The emitted signal is generally small in strength, so a local oscillator (LO) is used to heterodyne with the signal field to allow for detection. In the pump-probe geometry, the probe pulse acts as its own LO.

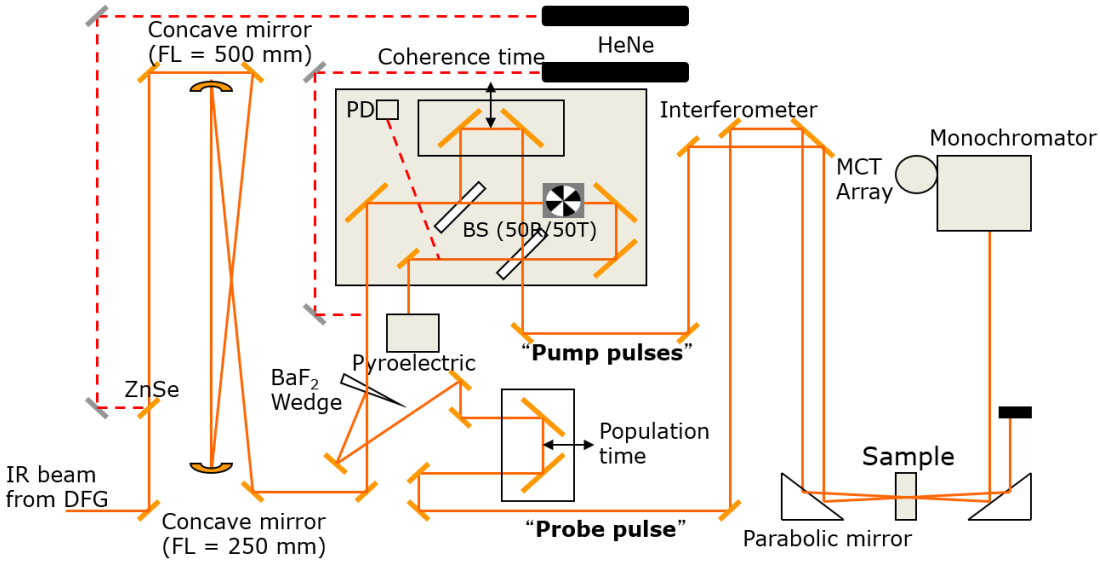

Figure 1.1 – 2D spectrometer layout. The two arms are detailed as "pump" and "probe" pulses. The different parts follow as detailed in the text.

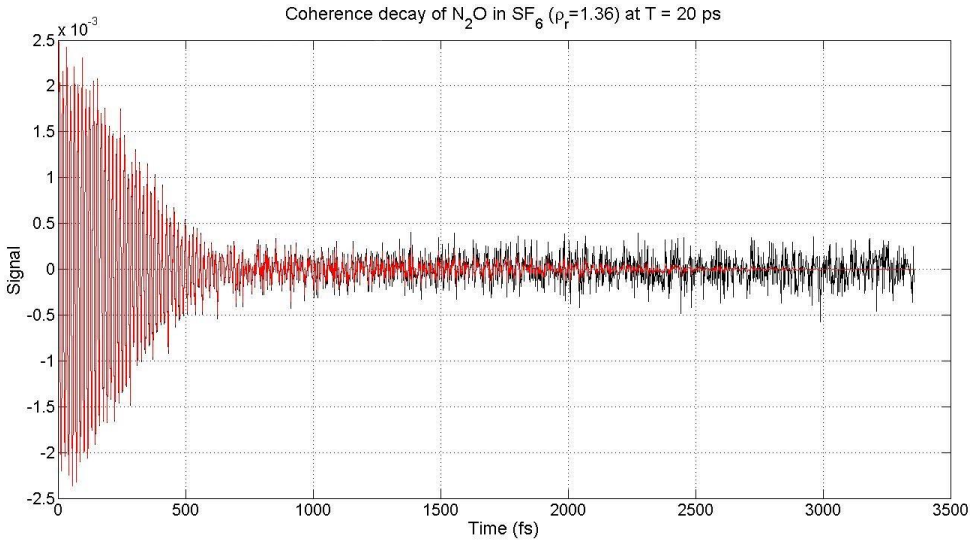

Figure 1.2 – Representative coherence decay with all signal transformations for the N_2O in SF_6 sample.

Chapter 2 - Structure Making and Breaking Effects of Cations in Aqueous Solution: Nitrous Oxide Pump–Probe Measurements[2]

2.1 Introduction

Nearly all water found in nature contains dissolved ions, and the influence of anions and cations on water's structure and dynamics can have significance for understanding their role in biological processes such as protein and nucleic acid stability, cell membrane transport, and cell signaling.[3] The often cited phenomenological Hofmeister series describes the relative ability of a given salt to precipitate proteins from aqueous solution.[4-5] It has been used subsequently to rank the relative effectiveness of ions to influence a wide variety of phenomena in aqueous solution.[6-7] The Hofmeister series trends, which generally follow the surface charge density of the solvated ions, have been used to assign aqueous solvated ions into two categories: kosmotropes, usually small ions with high charge density that stabilize membranes and proteins in solution, and chaotropes, large ions with small charge density that have the obverse effect. Phenomena that follow the usual Hofmeister series trends are traditionally rationalized in terms of the effects of these two classes of ions in water offering either weaker or stronger hydrogen bonds than water for solvation of other solutes (including protein surfaces).[6] A nearly synonymous and more general language has been subsequently used and accepted for aqueous salt solutions where kosmotropic and chaotropic ions are correspondingly described as "structure makers" or "structure breakers". [8-11] These terms are meant to describe the effect of the solvated ions of a given type to either increase or decrease the degree of ordering in the water solvent resulting in either a "stiffer" or "looser" hydrogen

bonding network in the solvent, respectively. Despite the long history of these categories there is still considerable controversy regarding the value of these concepts to describe the effect of ions generally in water and, in particular, the extent to which the effects of ions structurally and dynamically extend beyond the first solvation shell of waters surrounding these ions.[12] Some selected physical measures that highlight the effect of ions on bulk water macroscopic properties for the cations and anion are given in **Table 2.1**. Partial molal volumes ($\bar{V}^0$),[13] the effect on the volume of a large amount of water when one mole of an ion is added relative to water, the B_η coefficient from the Jones−Dole dynamic viscosity equation,[9, 14] a measure of a solution's viscosity relative to pure water due to the presence of an ion, and determinations of the entropy change in the structure of the water beyond the hydration shell ($\Delta S_{hydration}$)[9, 15-17] are given in this table. These properties have also been used to classify ions as structure breakers or structure makers, as well as measure the relative strength of ion−solvent interactions and the effects of ions on water's structure. As seen in **Table 2.1**, aqueous solutions containing cations with larger surface charge density have higher water densities (more negative $\bar{V}^0$), greater B_η viscosity coefficients, and more ordered solutions (more negative entropic changes) for a given anion. In particular, structure making ions have been classified by $B_\eta > 0$, while structure breaking ions have $B_\eta < 0$, corresponding to more or less viscous solutions relative to pure water, respectively.[9] ΔG_{HB}, an experimentally based composite measure of the effect of a solute on the hydrogen bonding structure of water derived from the change in ionic standard chemical potential from H_2O to D_2O,[15, 18] (last column of **Table 2.1**), classifies structure makers and breakers by $\Delta G_{HB} \geq +0.1$ and $\Delta G_{HB} \leq -0.1$,

respectively. Ions in the range $-0.1 \leq \Delta G_{HB} \leq +0.1$ are considered to be borderline in this classification scheme. Thus, by these measures Mg^{2+} and Ca^{2+} are structure makers (kosmotropes), Cs^{+} and K^{+}, structure breakers (chaotropes), and Na^{+} is near the border of this classification leaning slightly kosmotropic. A trend of strong to weak hydration for these cations is given by Mg^{2+}, Ca^{2+}, Na^{+}, K^{+}, Cs^{+} as seen from the data in **Table 2.1**. Correspondingly, Cl^{-} is a weakly hydrating anion[19] and categorized as a very modest structure breaker (**Table 2.1**).[9] The length scale of the hydrogen bonding network structure making or breaking ability of ions is a topic of considerable interest and debate.[9, 20-23] The macroscopic water structure effects of ions in aqueous solutions noted above (**Table 2.1**) pertain to solutions at infinite dilution and, hence, have been taken as evidence that solvated ions alter the global structure of water, and not just the structure and dynamics of an ion's closest solvation shell.[9] Some NMR,[24-26] X-ray diffraction,[25, 27-28] neutron diffraction,[29-31] time-domain OKE,[32-33] spontaneous Raman,[34-35] and dielectric relaxation[19, 36] studies of electrolyte solutions suggest longer range structural changes, i.e., structural changes beyond the first solvation shell, caused by dissolved ions. Thus, such observations are often taken as supportive of the notion of ions as hydrogen bonding network structure breakers or structure makers along with the macroscopic properties discussed above (**Table 2.1**). The long-range effects of ions on the hydrogen bonding network of water has also been studied by MD simulations where equivocal conclusions have been reached regarding the extent of structural perturbations by ions beyond their first solvation shell in aqueous solutions.[37-44] However, during the past decade studies of the ultrafast pump−probe and rotational orientation measurements, primarily resonant

with the O−H (O−D) stretching region in aqueous salt solutions, have largely concluded that ions have a very limited effect on the hydrogen bonded structure of liquid water outside the first solvation shell.[20],[45-47] Thus, in contradistinction to the long held view of ions as structure breakers or makers, these short-time, mid-IR observations have been used to argue that the macroscopic properties of salt solutions should be reinterpreted in terms of the influence of ions, anions in particular, on the first solvation shell only. Terahertz absorption studies have also been interpreted in terms of generally only more local effects, e.g., first solvation shell effects.[19-20, 23] Here we describe mid-IR ultrafast vibrational pump−probe and rotational anisotropy studies of a weakly polar molecular probe, N2O, dissolved in a series of 2 M aqueous chloride salt solutions to probe the effects of cations on the hydrogen bonding network of waters outside the first solvation shell of ions.

Brief Summary of Prior Ultrafast Studies of Effects of Ions on Water Structure

OH/OD Absorption Spectrum Changes Due to Salts. Ultrafast mid-IR pump−probe studies of the O−D/O−H stretch of HDO in H_2O/D_2O have been interpreted as a direct measure of the hydrogen bonding changes in aqueous electrolyte solutions. The peak of linear absorption spectrum of the OH (OD) stretch of HOD in D2O (H2O) is generally blue-shifted in salt solutions and attributed to the weakening of the excited OH (OD) bond resulting from the weaker hydrogen bond to the anion, O−D···X−/O−H···X−, than to another water, O−D···O/O−H···O.[20, 45, 48] For the halogens, this blue-shift follows the structure breaking trend: $I^- > Br^- > Cl^-$. Interestingly, the OH peak appears slightly redshifted in an aqueous solution of the structure making F^- salt relative to water.[49]

Correspondingly, the water bending mode is red-shifted relative to water also following the structure breaking trend, $I^- > Br^- > Cl^-$, and analogously attributed to the weaker hydrogen bonding ability of this sequence of anions.[50] Anions are generally accepted as having a larger effect than cations on properties related to Hofmeister trends owing to the greater polarizability of anions and water−ion distance effects.[5, 17] Anion−hydrogen bond interactions are enthalpically larger than cation−oxygen lone pair electron interactions for the same size ions due to the closer approach of the water hydrogen atoms.[51] Hence, cations were less of a focus in the ultrafast IR studies of salts, however cations are also known to shift the HOD frequency as much as if not more than anions.[52-53] These shifts exhibit less obvious trends with structure breaking/making cation character.[49] However, in 2M chloride salt solutions, Mg^{2+} accounts for a slight red-shifting effect and Cs^+ a blue-shifting for the OH stretch of H_2O (See **Figure 2.2**). These shifts may be rationalized in terms of stronger or weaker hydrogen bond interaction between first and second hydration shell interactions due to the polarization strength of the cation.[49] In addition to the blue-shift of the OH stretch fundamental in salt solutions with halogen anions, the OH absorption line width narrows according to the same structure breaking trend ($Cl^- < Br^- < I^-$) and both effects are attributed to the decreased strength of the $A^-\cdots$HOD hydrogen bond.[47]

OH/OD Vibrational Lifetime (T_1) Effects of Salts. The OD/OH stretch of HOD in H_2O/D_2O exhibits a longer vibrational lifetime than that of pure water in all relatively concentrated salt solutions (1−8 M).[20, 47-48, 52, 54] This VER process is typically characterized by a biexponential decay. The longer lived component is anion and

concentration dependent and is attributed to waters in the first solvation shell of the anions.[47-48, 52] The faster component is salt concentration independent and identical to that of pure water, and thus assigned to the relaxation of all other waters in solution, i.e., bulk and cation solvation waters. The decrease in vibrational energy relaxation rate is attributed to the decreased anharmonic coupling between the IR pump excited OD/OH local mode of waters in the first solvation shell of anions and its energy accepting hydrogen bonds, as well as the decreased frequency of the hydrogen bonds of these anion bound waters.[48, 52] The observed T_1 increase for a series of anions follows the Hofmeister series and hydration strength trend, e.g., $Cl^- < Br^- < I^-$ for a given cation (e.g., Na^+). This trend is ascribed to the decreasing hydrogen bonding strength between first solvation shell waters and the anion, which results in weaker interactions between the excited O−H (O−D) vibrator and the $A^-\cdots$HOD hydrogen bond. Anion mass effects, which red-shift the $A^-\cdots$HOD hydrogen bond frequency, and anion hydration number effects are also cited as contributing to the observed VER trend.[52] In contrast to the effects of anions, cations are observed to have only a small effect, ∼10% for the most strongly hydrating ions (Mg^{2+}, Li^+) at the highest concentrations (∼6 M), on the vibrational O−D/O−H stretch lifetimes of HDO in H_2O/ D_2O.[20, 52] This dependence is attributed to the effects of the cation perturbed solvation waters offering more strongly coupled anharmonic hydrogen bonds to the waters bound in the anion solvation shell.[52] This enhanced vibrational coupling is said to explain the observed corresponding decrease in lifetimes. For a given anion, such as Cl−, the observed OH/OD local mode lifetimes increase in the order $Mg^{2+} < Li^+ < Na^+$.[52] The increasing relative strength of the cationic hydrogen bond

as a function of cation ion charge density for $Na^+ < Li^+ < Mg^{2+}$ and the consequent increase in anharmonic interaction between excited stretch and energy accepting hydrogen bonds are taken to explain this trend. Thus, although all these stretch lifetimes in salt solutions are longer than found for neat water, the shorter T_1's are seen for the more strongly hydrated cations. Cationic bonded waters are reported to have the same OH/OD stretching lifetime as bulk waters.[20, 48, 52] Analogously, the vibrational relaxation of the bend vibration of water in aqueous salt solutions is slowed for anion bound waters while the bend T_1 of bulk or cation solvated waters is the same as in neat water and thus has a negligible effect on the bend VER rate.[50]

Orientational Relaxation Effects. The orientational relaxation of spectrally selected populations of excited OD stretches in HDO offers further measures of the perturbing effects of ions on the hydrogen bonding network of water solutions.[19-20, 45-46, 54-57] The vibrational pump−probe anisotropy decays (R(t)) of the blue-shifted, anion bound waters were found to be slowed due to hydrogen bonding to the anions and interpreted in terms of the rigidity of the first solvation shell around these anions.[45] In contrast, the excited HOD solvated to bulk waters (H2O···HOD) showed little salt dependence on R(t).[45-46] It was concluded from these studies that the presence of ions has no effect on the hydrogen bonding network of water outside of the first solvation shell of anions including cation hydrogen bonded waters, and thus ions do not lead to an enhancement or a breakdown of the hydrogen bond network in liquid water.[45-46] Initially cations were explicitly described as not affecting the reorientation of the hydroxyl groups of water molecules in fs-IR studies of HOD in D_2O/ H_2O for solutions up to 3M in salt concentration. Salt solutions

such as 3M $MgClO_4$ exhibit R(t) decays identical to that of water.[20, 46, 56] However, in subsequent studies of orientation relaxation in salt solutions, a model was developed for the biexponential decay of R(t) for this OD stretch, and it was noted how the constrained axis along the water oxygen to cation direction results in ultrafast IR being a poor measure of orientational relaxation for cation solvated waters when the OD stretch is the probe.[19, 23] In contrast, terahertz dielectric relaxation studies, which directly probe the orientational response of the water dipole, not the OH selected transition moment which defines the optically selected axis for fs-IR studies, find that significant fractions of slowed waters relative to bulk waters are cation dependent.[23] For a given anion, water dynamics are slower in solutions of more strongly hydrating cations. Thus, the choice of the spectroscopic probe offers selective insight into the structure and dynamics of different populations of a seemingly simple sample such as an aqueous salt solution. The experimental results reported here are consistent with this conclusion. In subsequent fs-IR rotational anisotropy studies employing HOD as a probe, R(t) has been found to be sensitive to cationic effects when salt concentrations approach 3M.[23, 56] At these high salt concentrations, cooperative effects due to ion pairing or clustering are cited to explain the slowing of re-orientational motions attributed to waters well beyond the first hydration shell for salt solutions of strongly hydrating anions and cations, such as $MgSO_4$ observed in these more recent HOD studies.[23, 58]

N_2O as a Solvation Probe. The vibrational energy and rotational re-orientational relaxation of the asymmetric stretch (ν_3) fundamental of nitrous oxide at ~2230 cm^{-1} are reported here as a probe of the ion perturbed aqueous solvent environment. The use of

N_2O as a reporter of its local solvation environment offers several advantages relative to other possible probes of aqueous salt solution dynamics. Due to its relatively small dipole moment (0.16 D)[59] and size relative to that of water, N_2O should not be located in the first solvation shell of cations or anions in aqueous solutions. Thus, in contrast to HOD or SCN^-, ultrafast vibrational measurements of N_2O report on water structure and dynamics beyond an ion's first solvation shell, including "free water" regions (to the extent that such regions exist in ~2M salt solutions), and probe more global changes in water−water dynamics due to the presence of ions. In contrast, HOD in H_2O/D_2O aqueous salt solution time-resolved IR experiments directly probe ion−water dynamics. The strong oxygen lone pair−cation interaction that renders OH pump−probe studies insensitive to orientational relaxation due to cation effects is not an issue for vibrational anisotropy measurements using nitrous oxide as a probe due to its weak dipole relative to water.[19, 23, 56] Furthermore, N_2O is a neutral triatomic and is thus a more minimally perturbing probe of aqueous salt solution structure and dynamics than larger molecular species or multiatomic ions, such as N_3^- or SCN^-, where ion pair interaction effects may be significant, particularly at high solute concentrations.[57] Finally, from an experimental viewpoint, the N_2O ν_3 asymmetric stretch 0→1 absorption has a large extinction coefficient in aqueous solution (~$1.5 \times 103 M^{-1}$ cm^{-1}) and a 18 cm^{-1} red-shifted excited state frequency in water resulting in strong pump−probe signals at the relatively low N_2O concentrations (~50−100mM) employed for these studies where N_2O−N_2O interactions should not be contributing to this solvation environment.[60] The N_2O ν_3 absorption at 2230 cm^{-1} overlaps two weak absorption features of the H_2O FTIR spectrum. As seen in

Figure 2.1, the N_2O stretch is resonant with the broad (~300 cm^{-1} FWHM) water bend ν_2−libration combination band centered at ~2130 cm^{-1}. It also overlaps a broad underlying absorption continuum attributable to higher order overtones and combinations of low frequency intermolecular modes resulting from the strong hydrogen bonding network of the liquid (see **Figure 2.1**). The ubiquitous contribution of this continuum spectral density contribution across the water IR spectrum more clearly evident in a semilog plot of the water IR spectrum (**Figure 2.1**) and is evident in Raman spectra of liquid water as well.[61-62] In prior work, distinct rates of vibrational energy relaxation (VER) were observed for the N2O ν_3 mode solvated in the acyl tail, interfacial water, and bulk water regions of hydrated DOPC (dioleoylphosphatidylcholine) bilayers.[63] The lifetime of the interfacial N_2O population was hydration level dependent, and this effect was attributed to changes in the density of intermolecular states contributing to the water's continuum absorption region resonant with the ν_3 band. The water continuum absorption intensity, i.e., the IR weighted continuum density of states, resulting from the oriented interfacial water molecules near the lipid phosphate scaled with hydration level and was inversely proportional to the N_2O ν_3 lifetime. In contrast, the spectral intensity of the water bend−libration combination band was essentially unchanged as the hydration level of DOPC was changed. Molecular dynamics simulations revealed that the charged lipid headgroups perturbed the local structure of the interlamellar waters, which likely caused the reduction of the density of continuum states resonant with the ν_3 mode of N_2O resulting in the slowed VER.[63] These results demonstrate that the VER mechanism for this N_2O stretch mode can be a sensitive probe of local solvation water structure, albeit

indirectly. The water librational spectrum is already known to be affected by the presence of ions in aqueous solution.[34-35, 64] Neutron diffraction, X-ray scattering, and Raman spectroscopy studies of salt solutions provide evidence that ions perturb the hydrogen bonding network of liquid water, and for some ions these perturbations extend beyond the first solvation shell.[29-31, 65-66] MD simulations have shown how the librational spectrum of water is sensitive to hydrogen bonding strength,[67] and some simulation studies find evidence of ion dependent changes on hydrogen bonding structure as well,[68] most significantly within the first solvation shell.[69] Thus, one might anticipate that an ion altered density of states in this region might affect the rate of vibrational relaxation for the N_2O ν_3 mode, in addition to energy transfer coupling effects due to structural and local charge perturbations. These expectations are tested here.

2.2 Experimental

Sample Preparation

Salt solutions used for ultrafast measurements were made at 2M using deionized water. KCl, NaCl, $CaCl_2$, and $MgCl_2$ were purchased from Acros Organics and CsCl was purchased from Sigma Aldrich. All were used as purchased. The solutions were made using volumetric flasks in 10 mL volumes. To fully dissolve the less soluble salts, the solutions were agitated using a vortex. If there was still particulate, the solution was heated and mixed further before letting it cool back to room temperature. There was no risk of the salts falling out of solution as they were all below the solubility limit at 2M. FTIR spectra concentrations were also 2M, except where noted otherwise.

The FTIR spectra of the solutions without nitrous oxide were obtained using 1-inch diameter, 1mm thick CaF_2 windows in a Thorlabs 1-inch lens holder. A drop of the solution was placed on one window before being sandwiched and the retaining ring tightened. Sample was remade if there were air bubbles present. These FTIR were taken on a Nicolet FTIR spectrometer. The chamber was purged for five minutes before an air background was taken and then five minutes before each sample was taken. This led to trace amounts of CO_2 and water vapor present in the chamber, allowing for better analysis of the FTIR spectra.

Ultrafast measurements were obtained in a custom variable path-length stainless steel sample cell, with 2 mm calcium fluoride windows and a 25μm Teflon spacer. Nitrous oxide was equilibrated with the ionic water solutions for a minimum of 12 hours at 200 psi to ensure saturation in the liquid solution. Under these conditions, an optical density of ~ 0.5 was reached for the antisymmetric stretching (ν_3) mode of N_2O corresponding to an N_2O concentration of 0.1 M. Static FTIR spectra were recorded at 1 cm^{-1} resolution with a Nicolet FTIR spectrometer equipped with a liquid-nitrogen-cooled MCT detector. All FTIR absorbance units were converted to extinction coefficients by incorporating the known density dependence of water and aqueous chloride salt solutions at the experimental concentrations.[70-71] This small correction factor allows comparison of aqueous absorption spectra for equal numbers of water molecules.

Ultrafast Spectrometer

The output of a 1 kHz regenerative amplified Ti:Sapphire laser system (Coherent, Inc.), which produced 7 mJ pulses centered at 800nm with a 35 fs pulse duration, pumps

a TOPAS (Light Conversion) optical parametric amplifier (OPA). Signal and idler beams from the OPA are combined collinearly in a 200 μm $AgGaS_2$ difference frequency generation (DFG) crystal resulting in 90 fs pulses centered at 2200 cm^{-1}, with a bandwidth of ~500 cm^{-1} and 6 μJ of energy. The IR beam is split by a 60-40 beam-splitter, into pump and probe beams. The probe arm includes a computer-controlled delay stage allowing precision control of the pump-probe delay time. The probe beam is dispersed after passing through the sample in a 150 mm monochromator (Acton Inc.) and collected on a 32-channel mercury cadmium telluride (MCT) array detector (Infrared Associates Inc.). The pump-probe signal is the change in optical density of the sample measured by the probe beam in the absence (I_{off}) and presence of the pump (I_{on}) as a function of the inter-pulse delay, T:

$$\Delta OD(T) = -log\left(\frac{I_{on}(T)}{I_{off}(T)}\right) \tag{2.1}$$

e pump and probe beam polarizations are controlled by a half waveplate in each beam. The relative polarization is set by rotating the waveplate in the pump arm relative to the fixed probe beam polarization direction. Thus, parallel, perpendicular or the magic angle (54.7 deg) pump-probe relative configurations could be readily achieved. A linear wire-grid polarizer placed after the sample acted as an analyzer and eliminated any polarization mixing induced by the optics.[72]

Pump-probe lifetime decays of the water bend-libration combination band without nitrous oxide in the solution were fit using a global fitting algorithm to a multi decay channel kinetic model determined in our previous neat water study[61]. Three different

experiments for each salt were run with different monochromator positions, 2218 cm^{-1}, 2311 cm^{-1}, and 2133 cm^{-1}, in order to record the dynamics at different frequencies resonant with the 300 cm^{-1} broad combination band absorption. The laser pulse has enough bandwidth that its center wavelength does not need to be moved to perform these dispersed measurements as done for our previous experimental measurements on neat water.

2.3 Results and Discussion

Linear Absorption Spectra of N2O v3 Band in Salt Solutions

FTIR spectra of the N_2O ν_3 fundamental in 2M aqueous solutions of the salts studied here with the H2O absorption removed compared with N_2O in neat H_2O are displayed in **Figure 2.2**. The corresponding N_2O ν_3 peak positions and bandwidths (fwhh) are summarized in **Table 2.2**. The cation dependent ν_3 frequency is slightly blue-shifted ($\sim$1−2 cm^{-1}), and the band is broadened by as much as 15% in these salt solutions relative to the ν_3 peak maximum and width in neat H_2O. Thus, it appears, at least phenomenologically, that the presence of the ions perturbs the N_2O solvent environment slightly outside the first solvation shell of ions, and furthermore this solvation effect is cation dependent. In contrast, the D_2O OD stretch absorption band shape and position in H_2O are reported as primarily anion dependent.[56] In HOD, the observed blue-shift of the OD stretch is attributed to weaker hydrogen bonding to the anions as compared to water. In aqueous MSCN (M = Li, K, Na) salt solutions, the observed SCN^- stretch absorption blue-shifts for the strongly hydrating cations (Li^+ , Na^+) and red-shifts for the most weakly hydrated cation (Cs^+) as a function of ion concentration.[57] However, for this

anionic probe, these spectral shifts are attributed to ion pair and cluster formation of the SCN^- reporter molecule. Such direct ion pair considerations do not apply for the neutral N_2O IR probe employed in this study. The N_2O ν_3 transition frequency is known to be dependent on the polarity of its environment owing to the relative importance of the two predominant resonance structures that can be used to characterize the ground electronic sate distribution of valence electrons. For example, the N_2O ν_3 gas phase transition frequency, 2222 cm^{-1}, red-shifts in octanol to 2215 cm^{-1} and blue-shifts to 2230 cm^{-1} in neat H_2O. Thus, it is not surprising that, in the more polar environment of 2M salt solutions, where the local field strengths are larger than in pure water due to the additional Coulombic interactions, the transition frequency shifts further to the blue than in the pure aqueous environment. Interestingly, the observed cation dependence of the magnitude of the blue-shift is $Cs^+ > Na^+ > Mg^{2+} > Ca^{2+}$ and thus does not follow a simple charge density or typical "Hofmeister" trend. The blue-shifted Ca^{2+} solution N_2O ν_3 peak is closest to the pure water solution observed frequency. The doubled anion concentration may act to lower the local net field strengths in the N_2O solution and thus limit the observed ν_3 blue-shift. The ν_3 blue-shift is largest in the solution of the most weakly hydrated cation, Cs^+, suggesting that waters in the second shell and beyond offer a more polar solvent than neat water. Such effects will be the subject of subsequent computational study. Again, we highlight that these frequency shifts, albeit small, are evident in "reporter" molecules not in the first solvation shell of aqueous solvated cations or anions. The broadening of the N_2O ν_3 transition band follows the trend $Cs^+ > Mg^{2+} > Na^+ > Ca^{2+}$ where the FWHM ν_3 spectral breadth in 2M $CaCl_2$ is nearly equal to that in

neat H_2O (**Table 2.2**). As seen for the peak blue-shift described above, the salt perturbing effect on the ν_3 FWHM is largest for the most weakly hydrating cation for this group of 2M chloride salts. It was found in a previous three-pulse photon echo study[60] that the line width of this N_2O ν_3 transition in H_2O is primarily due to contributions of the inertial water motions, rotational diffusion, and hydrogen bond network fluctuations. A determination of the molecular mechanisms of this line width broadening effect in salt solutions is beyond the scope of the current pump−probe report. The relative trend in rotational diffusion described below is consistent with the ν_3 transition being broader in the Cs^+ solution than in the Mg^{2+} solution. However, since we find both a slight increase (Cs^+) and decrease (Mg^{2+}) in the N_2O rotational anisotropy decay rate relative to R(t) in water, and all N_2O ν_3 bands are broader in these 2M salt solutions, another solvation mechanism must account for the observed, albeit relatively small, overall increase in the free induction decay rate (i.e., bandwidth increase) found for the N_2O ν3 transition in these chloride salt solutions. The dephasing due to the rapid inertial solvent motions and/or the hydrogen bond rearrangement thus must contribute to this effect. A combination of the lengthening of this hydrogen bonding network structural fluctuation time scale and/or increase in the initial distribution of N_2O ν_3 transition frequencies in the water environment perturbed by the ions could account for this faster effective dephasing rate. The frequency−frequency correlation functions determined in prior 2DIR studies of aqueous NaBr solutions probed by the O−D stretch revealed that the hydrogen bond rearrangement time is slowed in salt solutions.[54, 73] Furthermore, increased spectral diffusion time scales, i.e., a slowing of the hydrogen bonding network fluctuation time

scales, were deduced from frequency resolved pump−probe studies.[20] Subsequent 2DIR or 3PPE studies may be able to confirm that slowed energy fluctuation time scales are also the origin of this broadening effect in these aqueous chloride salt solutions probed by the N_2O ν_3 transition. Such analysis is required to directly correlate these probe molecule spectral changes with structure breaking/ making characteristics of these cations.

Cation Effects on the Vibrational Energy Relaxation of the N_2O ν_3 Band. The decaying components of the magic angle pump−probe responses resonant with the ν_3 0−1 transition of N_2O in H_2O and 2 M $MgCl_2$, $CaCl_2$, KCl, and CsCl aqueous solutions are shown in **Figure 2.3**. These responses are well fitted to a single exponential decay component plus a long-lived signal contribution (**Figure 2.3**) which is modeled as a constant over the time scale probed here (∼30 ps). The required constant term results from the sub-picosecond heating of the aqueous solution due to absorption of the broad pump pulse by the water bend−libration combination and continuum absorption region as reported earlier.[61] Modeling the water heating term with the previously determined rapid rise time (0.8 ps) did not affect the longer time exponential decay constant values reported here. The corresponding best-fit determined decays for the N_2O ν_3 fundamental lifetime in these aqueous 2M chloride salt solutions are cation dependent and summarized in **Table 2.3**. The N_2O ν_3 lifetime in bulk water is 9.0 ± 0.3 ps.[63] Vibrational energy relaxation is slowed in the chloride solutions with the most strongly hydrated cations, Mg^{2+} and Ca^{2+}, relative to VER in the pure aqueous solvent corresponding to N_2O ν_3 lifetimes of 11.2 and 10.1 ps, respectively. By contrast, VER is about the same rate or faster than the bulk water for solutions containing the weakly hydrated cations, K^+, Na^+,

and Cs^+. For the most weakly hydrated cation, Cs^+, the N_2O ν_3 excited state lifetime is 7.7 ps. Thus, the VER of this reporter molecule outside of the first solvation shell of these ions increases in solutions of cationic structure breakers and decreases in solutions of cationic structure makers relative to pure water. Thus, the salt perturbed VER responses probed by this weakly polar probe stand in contrast to the lifetime effects seen for OH/OD local mode studies of ionic solutions summarized above. Biexponential pump−probe decays are observed in VER studies of HOD in D_2O or H_2O and attributed to OH/OD oscillators hydrogen bonded in the first solvation shell of anions or in just bulk water regions and the solvation shell of cations.[20, 52] To the extent that only a single T1 component is detected in the N_2O ν3 responses, these signals are consistent with a homogeneous water solvated N_2O population, at least within the precision of these measurements. In contrast to the N_2O results, HOD stretch and bend lifetimes are observed to only increase in H_2O/D_2O solutions of ions.[20, 50, 52] As summarized above, HOD VER are most slowed by the presence of weakly hydrated anions, and cations have a small effect with the shortest lifetimes in solution of the most strongly hydrating cations. Thus, these trends are opposite to the lifetime effects for N_2O solvated in waters outside of the first solvation shell of ions studied here. Within the precision of these ensemble average experiments, the ν_3 VER relaxation of N_2O exhibits a uniform rate of vibrational energy relaxation that has been increased or decreased by the solvation effects of 2M cationic structure breakers or structure makers, respectively. The opposing trends revealed by these two different ultrafast vibrational probes can be attributed to the

different mechanisms responsible for the perturbed VER rates of each of these solvated molecular systems described further below.

Cation Effects on Water Absorption Spectrum and N_2O ν_3 VER. Salt Effects on the 1900−2600 cm^{-1} Region of the H_2O Absorption Region. Dissolved salts are well-known to perturb the vibrational absorption and Raman spectra of water in aqueous solutions.[35, 64, 74-76] Owing to the large intermolecular contribution to the vibrational DOS in the water absorption spectrum in the 1900 to 2600 cm^{-1} region due to the bend libration combination and continuum contributions, it is not surprising that salt perturbations are relatively large in this spectral region. FTIR spectra of room temperature 2 M $MgCl_2$, $CaCl_2$, NaCl, KCl, and CsCl solutions and neat water from 1900 to 2600 cm^{-1} are shown in **Figure 2.4**. As described above, the broad (∼300 cm^{-1}), asymmetric H_2O bend−libration ($\nu_B + \nu_L$) combination band is centered near the middle of this spectral region and overlaps a continuum absorption contribution due to the strong hydrogen bonding network of water (**Figure 2.1**).[62, 77-79] The center frequency of the narrower N_2O ν_3 antisymmetric stretch, at ∼2230 cm^{-1}, is indicated by the vertical line in **Figure 2.4** and thus overlaps both the salt dependent bend−libration combination and continuum water absorption features. As seen in **Figure 2.4**, the water absorption spectrum is perturbed at this concentration by the solvation of these salts. (These 2M chloride salt solution spectra are overlapped and plotted on the same molar extinction scale in **Figure 2.8**.) To quantify and uncover any systematic phenomenological trends in the salt dependence of these water spectra, this absorption region was fitted to as simple a line shape model as possible. The resulting best-fits are shown in **Figure 2.4** and required a

minimum of three components, two Gaussians and a sloping linear baseline, to achieve excellent fits to this absorption region in both neat water and all 2M chloride salt solutions. Gaussians centered on the red and blue sides of the bend−libration combination band are needed to fit this asymmetric and slightly structured feature, and the linear term captures the continuum contribution to the spectral density in this region. **Figure 2.9** illustrates the inadequacy of just a single Gaussian plus a sloping baseline model for fitting this region in the neat water absorption spectrum. The best-fit determined parameters (Gaussian center frequencies, ω_R and ω_B, corresponding widths, FWHM, and areas, AR, AB, A_{tot} = AR + AB), as well as the relative contribution of all three components to the absorption intensity at 2230 cm^{-1}, the peak of the N_2O ν_3 band, are summarized in **Table 2.3**. The two Gaussian components are most clearly resolved in the 2 M $MgCl_2$ spectrum (**Figure 2.4**). As a further test of the robustness of this model, excellent fits to spectra of $MgCl_2$ solutions in the 1 to 5 M range are also obtained by using this three-component model (**Figures 2.10 and 2.11**; the resulting best-fit parameters are given in **Table 2.4**). Although there have been some previous attempts to model neat and salt solution water absorption spectra as a sum of Gaussians,[62, 76] the spectral fitting procedure given here (**Figures 2.4 and 2.11**) is the most precise attempt that has been focused on the bend−libration region alone, and it allows a phenomenological characterization of the perturbation due to these solvated ions of this hydrogen bonding network dependent portion of water's absorption spectrum.

Salt Perturbed Water Spectrum and N2O ν_3 VER.

In our previous study of the N_2O ν_3 lifetimes as a function of hydration in phospholipid interlamellar layers, a correlation of VER rate and continuum intensity in the corresponding water spectra at 2230 cm^{-1} was observed and thus used to rationalize the observed lifetime trends.[63] However, absorption trends that scale with cation hydration strength and hence lifetimes are not as obvious in the 1900−2600 cm^{-1} region fitting results obtained here, but a few correlations can be detected **(Table 2.3**, **Figure 2.4, Table 2.4**, **Figure 2.11)**. In contrast to the hydration level dependent phospholipid studies, analysis of this region of the water spectrum is more complicated due to the effects of chloride anions, albeit a weakly hydrating ion, and divalent cation solutions have twice as many anions as monovalent solutions, in addition to the effects of the various cations. Thus, network hydrogen bonding waters solvating cations, anions, and other waters will all be contributing to the spectral density in this region of the water spectra of salt solutions. For example, the integrated area of the bend−libration band is nearly the same for water and all the solutions studied. The continuum intensity, the total absorption intensity, and the bend−libration intensity at 2230 cm^{-1} also show no systematic trends with cation hydration strength (**Figure 2.5 and Table 2.3**). This FTIR spectral modeling, however, does show redistribution of the bend−libration intensity between the red and blue Gaussian components. For all the 2 M salt solutions, the area of the blue Gaussian (AB) is larger than that of water and mostly follows the hydration strength trend from Mg^{2+} (55% increase) to Cs^{+} (5% increase) (**Table 2.3, Figure 2.12**). We also note that while the bend−libration integrated area is constant within 10% for the 1 to 5 M $MgCl_2$ spectra, the AR/AB area ratios decrease by more than a factor of 2

(**Table 2.4, Figure 2.10**) while the corresponding continuum contribution remains nearly unchanged as the $MgCl_2$ concentration increases. Interestingly, the center of the red Gaussian (ω_R) is red-shifted by an amount that is Cl^- concentration dependent only; NaCl ≈ KCl ≈ CsCl ≈ 2091 cm^{-1} and $MgCl_2$ ≈ $CaCl_2$ ≈ 2081 cm^{-1}. In contrast, the peak of the bluer Gaussian bend−libration component (ω_B) is cation dependent and centered either to the red or the blue of that of water. ω_B of the structure making cations (Mg^{2+}, Ca^{2+}) are considerably blue-shifted relative to those of the more structure breaking cations (K^+, Cs^+). Thus, the redder Gaussian seems more associated with Cl^- solvation environment, and the waters solvating cations more closely influence the bluer Gaussian bend−libration feature. From a simple Fermi Golden Rule framework, the DOS of energy accepting modes is one of the central factors controlling the rate of energy relaxation.[80-84] As described above, in our previous pump−probe study of N_2O dissolved in hydrated phospholipid bilayers, the rate of ν_3 vibrational energy relaxation for N_2O's in the interlamellar water regions between head groups exhibited a dependence on the magnitude of the continuum absorption strength at the resonant vibrational frequency.[63] However, such a correlation is not observed for the lifetime trends in these salt solutions. To the extent that the energy relaxation of the solute N_2O ν_3 2130 cm^{-1} of energy occurs by resonant energy transfer to the solvent, given the sparse intramolecular N_2O density of states (DOS), one qualitative trend potentially relevant to the observed N_2O relaxation dynamics in aqueous salt solutions is evident from this DOS analysis. As shown in **Figure 2.5 and Table 2.3**, only the relative change in the ν_3-resonant (2230 cm^{-1}) IR weighted DOS associated with the red Gaussian contribution to the bend−libration band

scales with the experimental VER according to cation hydration strength. Thus, this empirical trend at least suggests that, with increasing cation hydration strength, the bend−libration DOS of the salt solution are redistributed resulting in a smaller effective DOS for the solvated N_2O and hence longer lifetimes. However, the VER rate for neat H_2O is faster for "structure makers" (Mg^{2+}, Ca^{2+}, Na^+) and slower for "structure breakers" (K^+ , Cs^+), the contribution of this red Gaussian DOS is greater at 2230 cm^{-1} than for all the salt solutions, and thus coupling strengths governing the solute−solvent energy transfer also are affected by the presence of the salt. Subsequent simulations, as well as potentially 2DIR measurements, will be needed to determine not only the nature of this absorption region in water but the details of the energy coupling mechanisms between the N_2O solute and its aqueous environment.

Cation Effects on the Rotational Reorientational Decay of the N_2O ν_3 Band. The observed time dependence of the rotational anisotropy of the N_2O ν_3 transition dipole in pure H_2O, 2M $MgCl_2$, and 2M CsCl is shown in **Figure 2.6**. These chloride salts are the most strongly and weakly hydrating cations studied here. The time scale of reorientational relaxation decays (∼1 ps) for this probe is an order of magnitude faster than the corresponding vibrational lifetimes (∼10 ps). The contribution of the long-lived water heating term described above to the separately observed parallel and perpendicularly polarized pump−probe responses has been removed prior to the calculation of the N_2O ν_3 time dependent rotational anisotropies displayed in **Figure 2.6**.[61] A minimum of two exponentials is required to fit all the resulting N_2O ν_3 anisotropy decays as most evident from the semilog plots of R(t) (inset **Figure 2.6**). The smaller amplitude, faster

component has a time constant of 0.15 ± 0.06 ps in all the observed anisotropy decays, including the orientational relaxation of N_2O in pure water, and is thus independent of the presence of ions in these 2M aqueous salt solutions within the precision of these observations. This rapid initial decay may be attributed to inertial or rapid librational water motions. A short-time (≤100 fs) component was found in MD simulations of anisotropy decays of neat water and aqueous salt solutions.[38, 85-86] In contrast to these aqueous solution results, the corresponding rotational anisotropy decay of the N_2O ν_3 transition in octanol, for example, shows only a single exponential decay dependence.[60] The longer time anisotropy relaxation component, however, shows a small but discernible dependence on the solution cations, as summarized in **Table 2.3.** This N_2O ν_3 reorientational decay component is slower (τ_{or} = 1.25 ps ± 0.10) in 2M $MgCl_2$ and faster (τ_{or} = 0.85 ps ± 0.10) in 2 M CsCl relative to neat water (τ_{or} = 1.0 ps ± 0.10) in respectively a strongly hydrated, structure making cation solution and a weakly hydrated, structure breaking cation solution. The chloride anion is as well a weakly hydrating anion. At this experimental concentration and precision, the effect of cations on the orientational decay can only be described by a single exponential decay component consistent with N_2O in only one solvation environment in these salt solutions, that either decreases (Mg^{2+}) or increases (Cs^{+}) the rate of rotational reorientation. Although not explicitly included here, the rotational anisotropies of 2M $CaCl_2$, NaCl, and KCl had fits that resulted in decays that were not significantly different from water (±0.10) although they did show the same trend with hydration strength. Substantial concentrations of contact ion pairs with the weakly hydrating chloride anion are not expected in 2M salt

solutions.[58] As summarized above, previous studies of R(t) in salt solutions based on the HOD stretch in D_2O/H_2O initially concluded that orientational relaxation of waters was unaffected by cations and that waters beyond the first solvation shell of anions exhibited only bulk-like anisotropy dynamics.[20, 45-46] Reorientational dynamics of waters in the first solvation shell of anions, including Cl^-, were slowed relative to water and attributed to the more restricted motion along the OH/OD··· X− axis and transition dipole direction.[55] Simulations have shown that an extended molecular jump reorientation model, at least for weakly hydrated anions, can account for these slower time scales.36 With better spectral resolution of dynamics from anion-bonded waters and all other waters, cations at concentration greater than 3M were found to slow the reorientational motion of vibrationally excited OD stretches of HOD's bonded to other waters in solutions containing strongly hydrating cations (Na^+ , Mg^{2+}).[56] In a subsequent study ion cooperativity effects for aqueous salt solutions of strongly hydrating cations and anions, such as $MgSO_4$, were found to have slowed water reorientational dynamics attributed to waters beyond the first solvation shell.[23] However, the chloride anion is a weakly hydrating species, and thus such cooperativity or ion pairing effects should not be significant here. Finally, in aqueous salt solutions of MSCN (M = Li, Na, K, Cs) the rotational dynamics of both SCN^- anions and water molecules are shown to be dependent on cations.[57] In qualitative agreement with the results reported here, 2M solutions of SCN^- salts show a small cation dependent anisotropy decay rate for HOD in H_2O solutions of MSCN that are slowest for the most strongly hydrated cation, Li^+ , with time constants that follow the trend $Li^+ > Na^+ > K^+ \approx Cs^+$. Rotational reorientation relaxation

is the same as HOD in H2O for 5M KSCN and CsSCN, although, not commented upon by the authors, HOD relaxation in 2M CsSCN appears slightly faster in agreement with the results reported here.[57] It is unclear if these are first solvation shell effects or not in these MSCN studies. Despite identical orientational rates for the OH/OD stretch in neat water and for non-anion-bonded waters of strongly hydrated cations such as 3M $Mg(ClO_4)_2$, evidence for slowly reorienting waters associated with cations, including $Mg^{2+,}$ was detected via terahertz dielectric relaxation measurements.[19-20, 23] As indicated above, fs-IR HOD OH/OD stretching studies have limited ability to monitor reorientational dynamics for solvated cations. Such restrictions do not apply for DR relaxation due to the different directions of the OH/OD transition dipole and the water molecular dipole moment.[19, 23] Thus, in contrast to the prior results where the probes of orientational relaxation are primarily waters in the first solvation shell of anions or multiatomic anions, the neutral, slightly polar N_2O probe shows both an increase and a decrease in the rotational anisotropy decay relative to that of neat water for the structure making and structure breaking 2M Mg^{2+} and Cs^+ chloride solutions, respectively. This experimental observation is consistent with the macroscopic expectation of ion perturbation effects on water's hydrogen bonding network predicted by values of the relative viscosity of these solutions compared to that of neat water.[9, 46] The viscosity of a 2M $MgCl_2$ solution is about 75% larger than that of pure water, and that of CsCl, 10% less based on B_η values alone (**Table 2.1**). While the detailed molecular mechanism of the reorientational relaxation of N_2O in aqueous solution has yet to be determined, these results are at least consistent with the description of a perturbed water hydrogen bonding

network outside of the first solvation shell of ions that is either “looser” or “stronger” in accordance with the structure breaking or making designation of cations.[10]

2.4 Conclusion

Most conclusions on the perturbing effect of ions on the hydrogen bonding structure of water based on fs-IR measurements are derived from the time-resolved responses of the OH/ OD stretch of HOD in D_2O/H_2O. While this vibrational local mode has the advantage of reporting on the effects of hydrogen bond interactions with ions, primarily anions, directly, it has limited capability to report on other solvation regions of aqueous salt solutions. Here we use the asymmetric stretch (ν_3) of N_2O, a small, neutral, non-hydrogen bonding, slightly polar molecule to report on ultrafast responses in water regions outside of the first solvation shell of ions, specifically for a series of cations in aqueous chloride salt solutions. Decay rates of N_2O ν_3 VER increase in 2M weakly hydrated, so-called “structure breaker” cations (Cs^+, K^+) and decrease in strongly hydrated, “structure maker” cations (Mg^{2+}, Ca^{2+}) relative to neat water. ν_3 lifetimes follow the Hofmeister series trend $Mg^{2+} > Ca^{2+} > Na^+ > K^+ > Cs^+$. This is in contrast to the OH/OD stretch results which only find VER rates slowed in salt solutions and the effects of cations to be small with only the most strongly hydrating cations increasing this VER rate relative to the much stronger slowing effects of anions, particularly more weakly hydrating ions. Furthermore, VER rates decrease with increasing hydration strength when HOD is the vibrational probe in salt solutions as compared to the opposite hydration trend observed for the ν_3 lifetimes as described above.[20, 52] Spectral analysis of the resonant bend−libration/continuum region of the perturbed water absorption spectrum

indicates that, perhaps not surprisingly, both energy transfer coupling and DOS effects contribute to this N_2O ν_3 VER trend with hydration strength in this region outside the first solvation shell of ions. However, in analogy to N_2O ν_3 pump−probe results in the confined interlamellar regions of bilayers of phospholipid with zwitterionic headgroups where VER is slowed in the more structured (ordered) aqueous regions, slower VER is also seen here for the more structure making cations in water solutions.[63] N_2O dissolved in aqueous solutions shows VER dynamics trends that are different from those seen in previous experiments performed with the bend and stretch absorptions of HOD as probes of local aqueous structure owing to the different relaxation mechanisms of the two probe molecules in their distinct solvation environments. Similarly, rotational reorientation of N_2O probed by ν_3 anisotropy measurements (R(t)) are slightly faster and slower in Cs^+ and Mg^{2+} 2M chloride salt solutions respectively relative to neat H_2O. These trends scale with the macroscopic viscosity and are again consistent with the structure breaking and structure making characterization of these cations. These results also appear to be in contradistinction to HOD R(t) studies.[19-20, 23, 46, 56] For most salt solutions studied, the HOD molecules outside of the first solvation shell of anions show the same reorientation dynamics as observed for bulk liquid water via R(t) measurements. However, at concentrations >3M, the rotational dynamics of OD groups bonded to other water molecules are observed to slow down in solutions with strongly hydrating cations in addition to the slowing effect of anions and attributed to the onset of coopertivity.[56] The cation dependent effects evident in the N2O responses are more consistent with the dielectric relaxation results that show that cations can have an influence on water

structure and dynamics and stand in contradistinction to the fs-IR results reported by earlier OH/ OD studies that the only effects of salts on water structure and dynamics are in the first solvation shell of anions. As indicated above, the lack of sensitivity of OH/OD water stretch to direct cationic interaction effects has been subsequently explained in terms of the different orientational geometries of waters in the first solvation shell water of cations and anions which inherently limits the value of rotational anisotropy measurement of cation perturbed water transition dipoles. This constraint does not apply to fs-IR studies of the very weakly polar N_2O probe. Evidence for the "structure breaking" or "structure making" effects beyond the first solvation shell is rarely reported in the HOD based fs-IR studies. In contrast, fs-IR measurements of rotational anisotropy and lifetimes of the ν_3 N_2O probe find dynamical effects consistent with the categorization of large charge density cations as structure makers and small charge density cations as structure makers outside of the first solvation shell of ions. At 2M chloride salt concentrations, where the ion/water ratio is $\sim$1/13 for monovalent cations and higher for divalent cations, it may not be accurate to say that N_2O is reporting on the perturbation of bulk water by ions due to the close proximity of anion and cation first solvation shells. However, these N_2O results report on water perturbation effects affecting a vibrational probe in at least the second shell region. Vibrational energy and orientational relaxation results differ via HOD or N_2O due to the nature of the reporter molecule used and the consequently different solvent environments probed by each. Subsequent simulation and salt concentration dependent N_2O ν_3 pump−probe measurements are planned to further confirm this plausible N_2O solvation environment

and the nature of the apparent intermolecular N_2O ν_3 vibrational relaxation mechanism. Solvation effects of salts on the linear absorption of the ν_3 N_2O transition are also small but robust as described above and, in contrast to the VER and R(t) results, do not show a clear trend with cation hydration strength or structure breaking/structure making characterization. Subsequent 2DIR or IR photon echo studies and MD simulations may reveal how ion perturbed rotational diffusion and spectral diffusion mechanisms combine to consistently blue-shift and broaden the ν_3 band of N_2O relative to neat water. However, the ν_3 vibrational peak blue-shift is indicative of a solvation environment that is more polar for all these salt solutions than that due to water alone. Furthermore, the more rapid free induction decay (broader ν_3 line widths) is consistent with a slower hydrogen bonding network structural fluctuation time as observed in NaBr salt solutions.[54, 73] Finally, most vibrational spectroscopic studies of the effect of salts on water's hydrogen bonding structure and dynamics have been focused on the OH (OD) stretching, owing to the strong oscillator strength of this band and its direct sensitivity to hydrogen bonding character. As evident here, however, salts can have a more dramatic relative change on the bend− libration and continuum regions of the water spectrum. In addition to the important role that the continuum and the librational density of states plays in energy dissipation in aqueous solutions, the combination band region has a high sensitivity to the nature of the intermolecular hydrogen bonding network, and can help to complete the unfolding picture of the nature of the Hofmeister series effects and the challenge of characterizing the dynamics and structure of the hydrogen bonding network in water. The weaker oscillator strength and the precise computational description of these extended

intermolecular nuclear motions in this mid-IR spectral region (1900−2600 cm^{-1}) offer both an experimental and computational challenge to using these H_2O vibrational spectral features as a direct probe of the effects of ions on the water hydrogen bonding structure and dynamics, but the potential for this purpose is evident here. These results highlight the value of using different types of reporter probe molecules to address questions of solvation structure and dynamics particularly in a hydrogen bonding system.

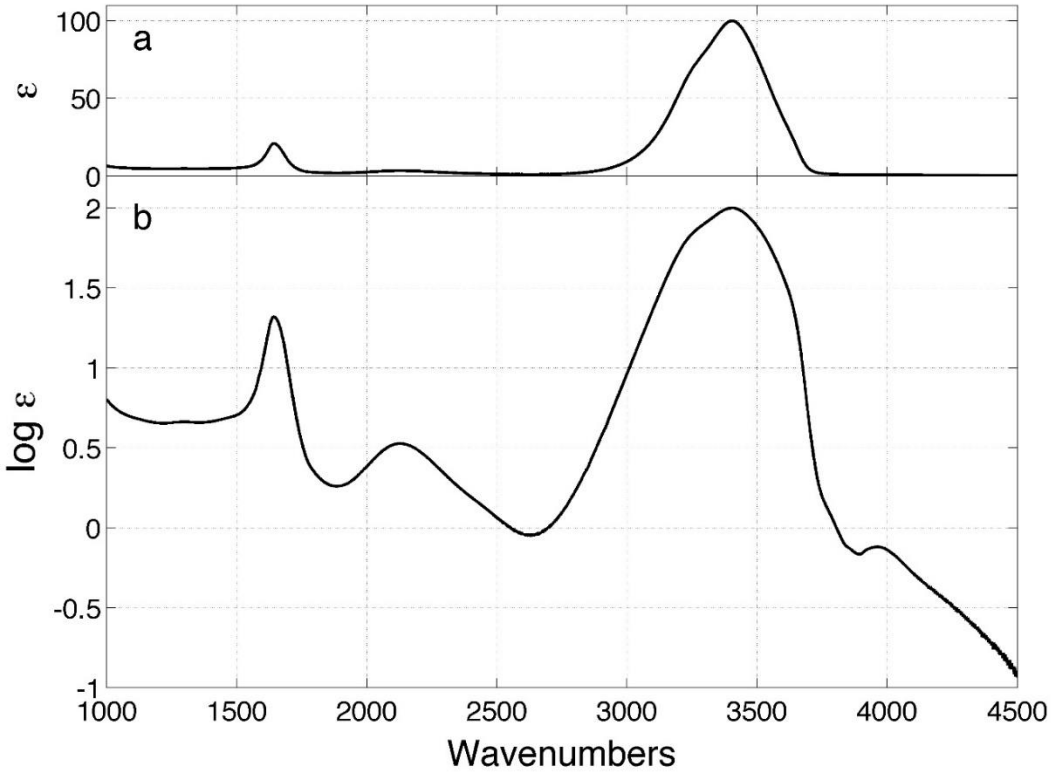

Figure 2.1 - a. Absorption spectrum of neat water, showing the extinction coefficient as a function of wavenumber. b. semilog plot of water absorption spectrum. Inset shows 1900 – 2600 cm^{-1} region of aqueous N_2O solution. The narrow absorption band at 2230 cm^{-1} is the ν_3 asymmetric stretch fundamental transition of N_2O.

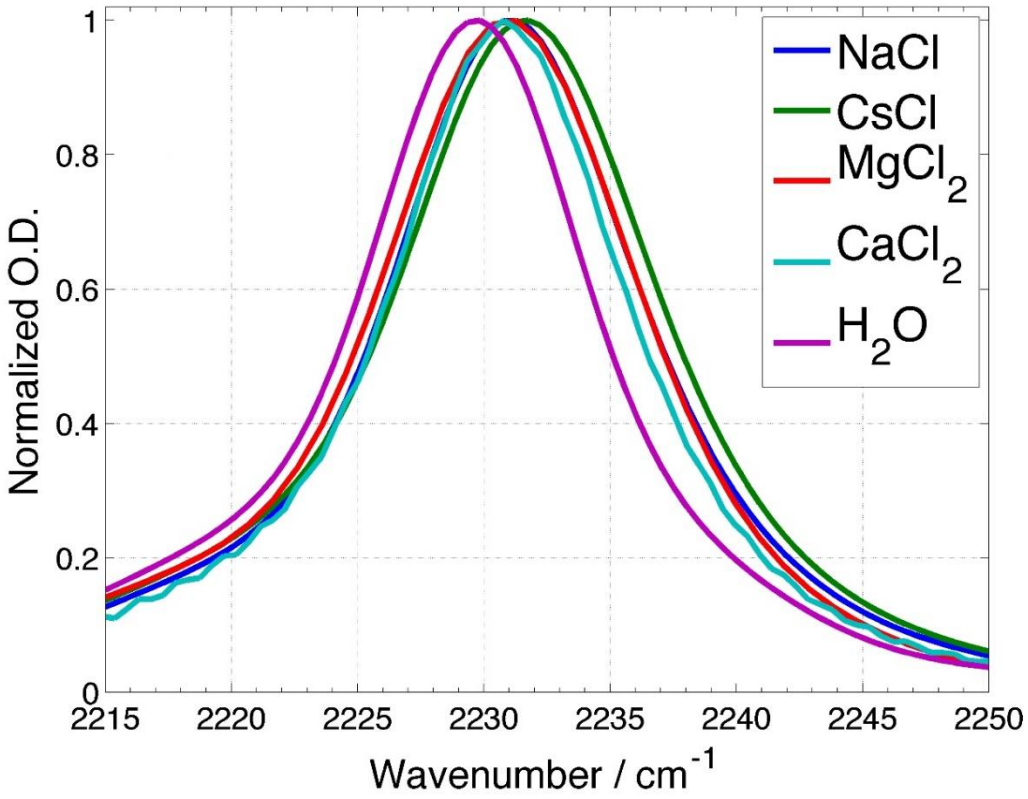

Figure 2.2 - Absorption spectra of the ν_3 asymmetric stretch fundamental transition of N_2O in 2M NaCl, CsCl, $MgCl_2$, $CaCl_2$ and neat H_2O. The water absorption due to the bend-libration combination and continuum background have been removed. Small ν_3 peak shifts and bandwidth changes (Table 2.2) are observed in the salt solutions relative to neat water.

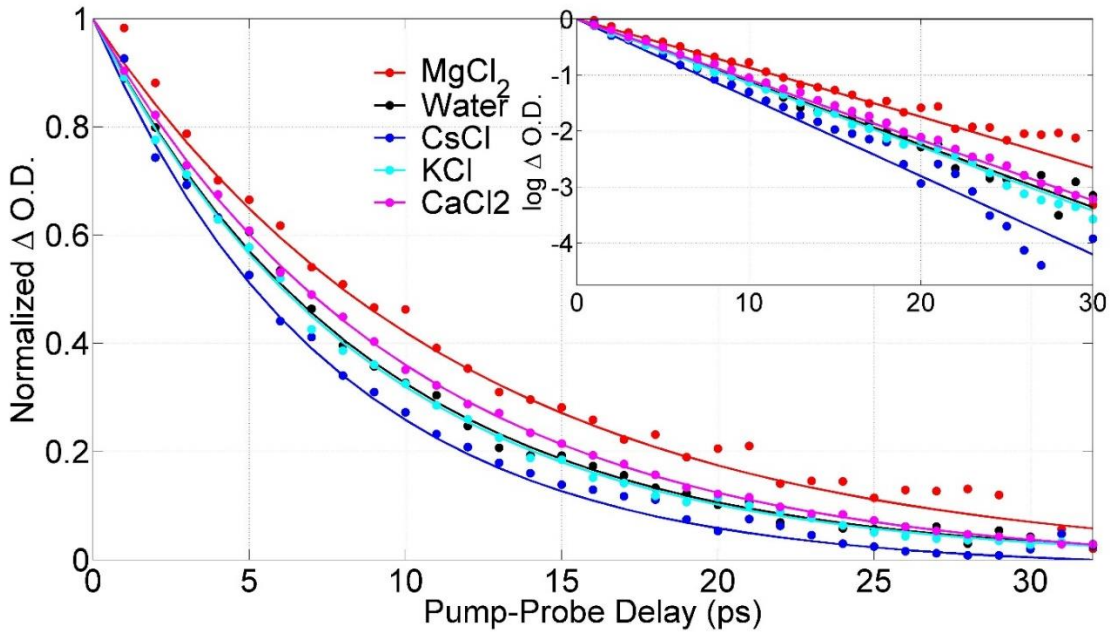

Figure 2.3 - The decaying portion of the pump-probe response of the N_2O ν_3 fundamental transition in 2M NaCl, CsCl, $MgCl_2$, $CaCl_2$ and neat H_2O excited by 90 fs pulses centered at ~2230 cm^{-1}. A term due to the subpicosecond heating of water directly excited by the pump pulse does not decay on this time scale and has been subtracted.

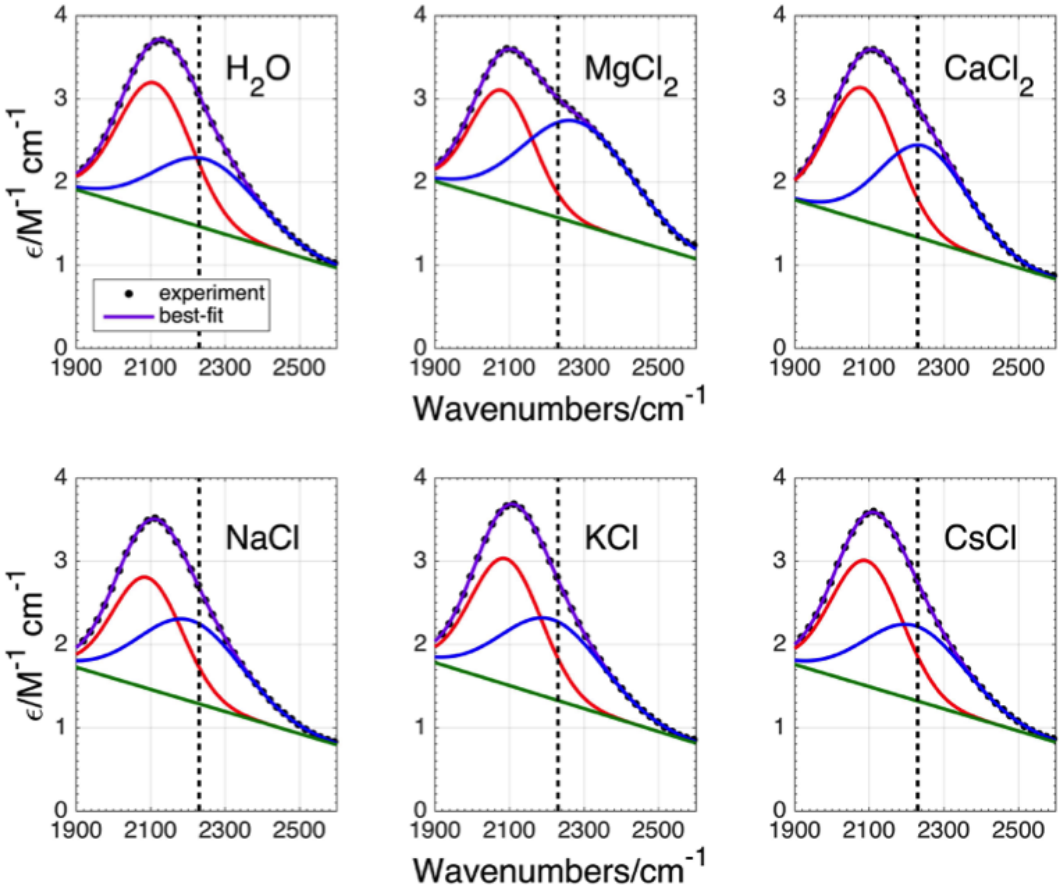

Figure 2.4 - The observed FTIR spectra (black dots) of the ($\nu_2 + \nu_L$) combination band region and resulting best fits (sum of two-Gaussians and a linear baseline term given in purple) of H_2O and the indicated 2M salt solutions. The sum of the two Gaussians (indicated in red and blue) corresponds to the ($\nu_2 + \nu_L$) bend-libration combination band and the sloping linear baseline contribution (green), represents the continuum absorption in this region for each solution. The dashed vertical line corresponds to the peak of the N_2O ν_3 fundamental transition (~2230 cm^{-1}).

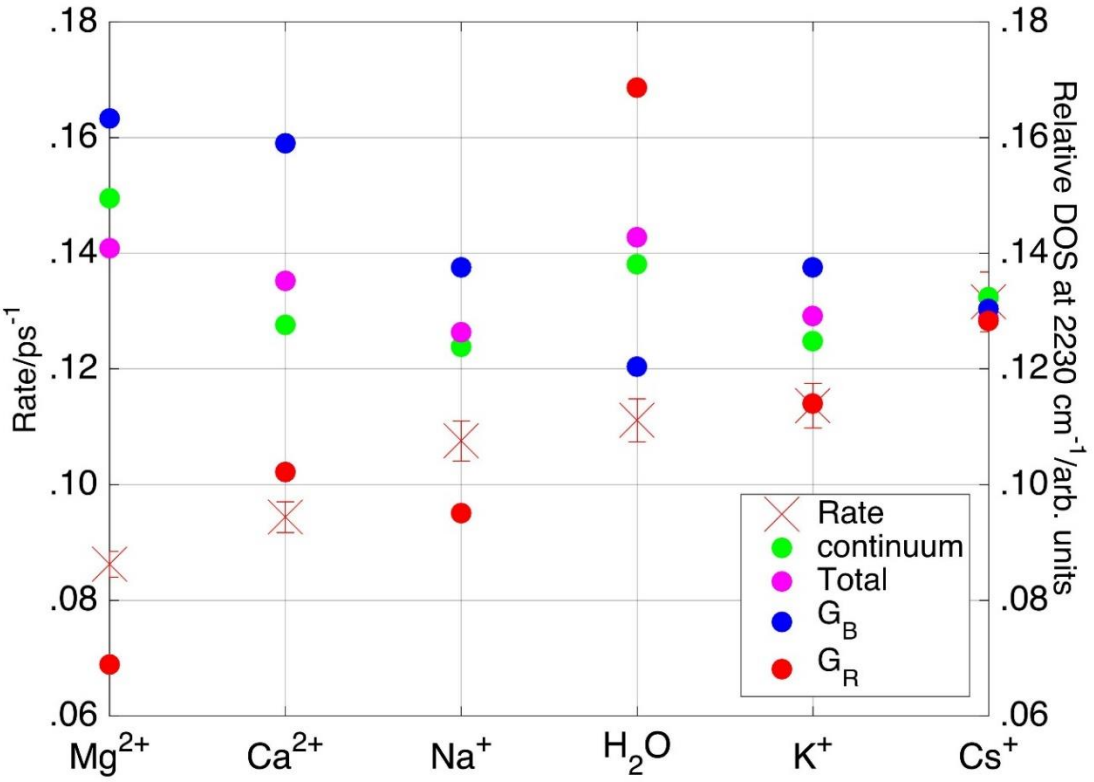

Figure 2.5 - Observed N_2O ν_3 v = 1 VER rates (inverse lifetime) in neat water and 2M aqueous salts (X): $MgCl_2$, $CaCl_2$, NaCl, KCl and CsCl (Table 2.3). The intensity of the best-fit determined continuum (green), total (purple), blue Gaussian (blue) and red Gaussian (red) absorption intensity at 2230 cm^{-1} is plotted as a function of salt cation for the 2M solutions. The ions are arranged in terms of decreasing hydration strength (Table 2.1). Taking the transition intensity to be salt independent, these relative contributions scale with the DOS at 2230 cm^{-1}, the N_2O ν_3 transition frequency. The result for neat water is also shown.

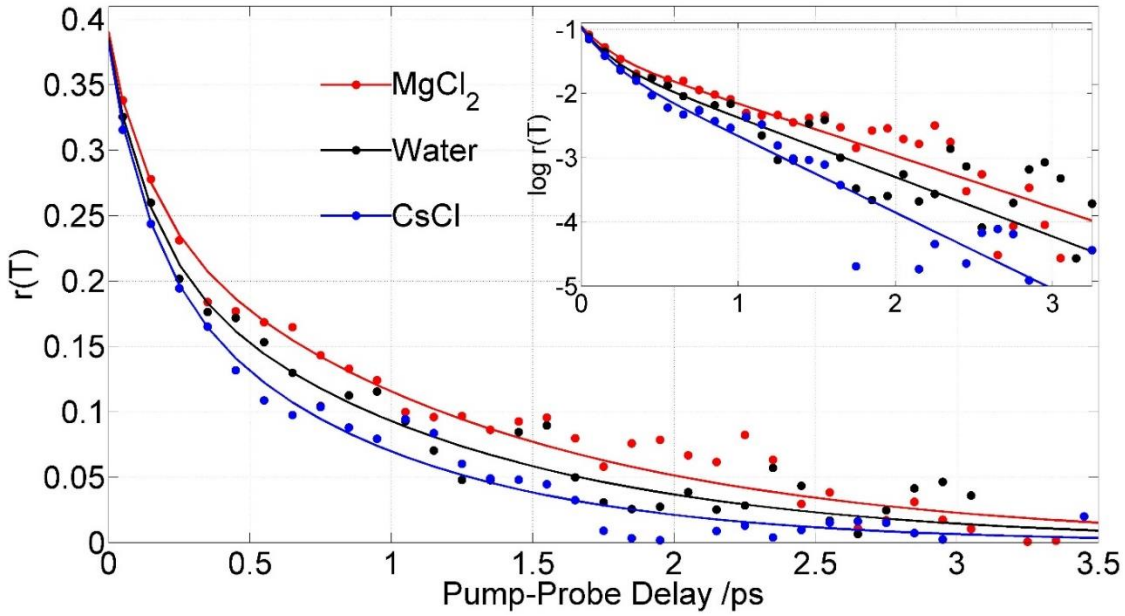

Figure 2.6 - Rotational anisotropy measurements of the ν_3 transition of N_2O in 2M $MgCl_2$, 2M CsCl and neat H_2O.

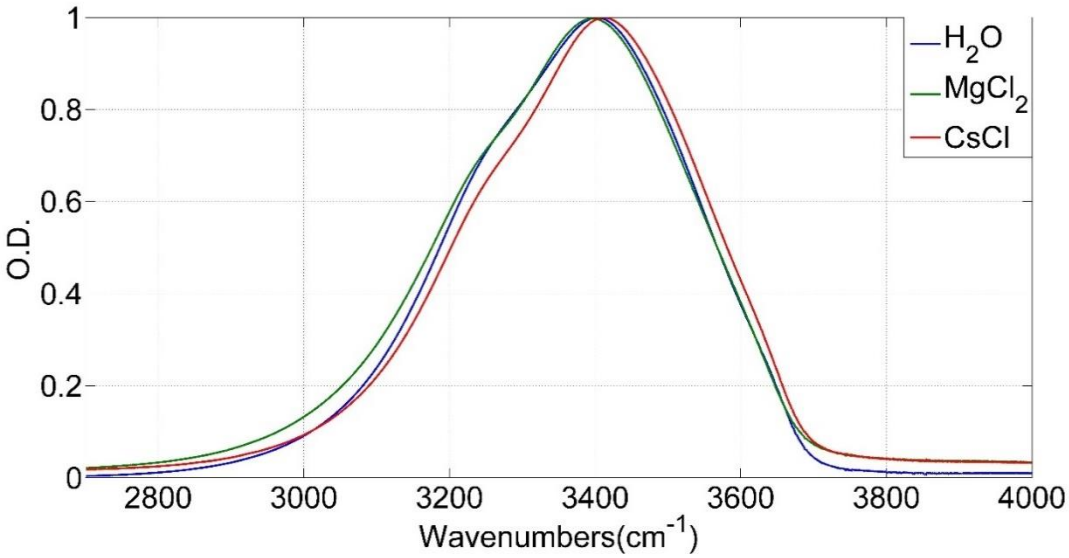

Figure 2.7 - Normalized absorption spectrum of OH stretch region of water and 2M solutions of $MgCl_2$ and CsCl.

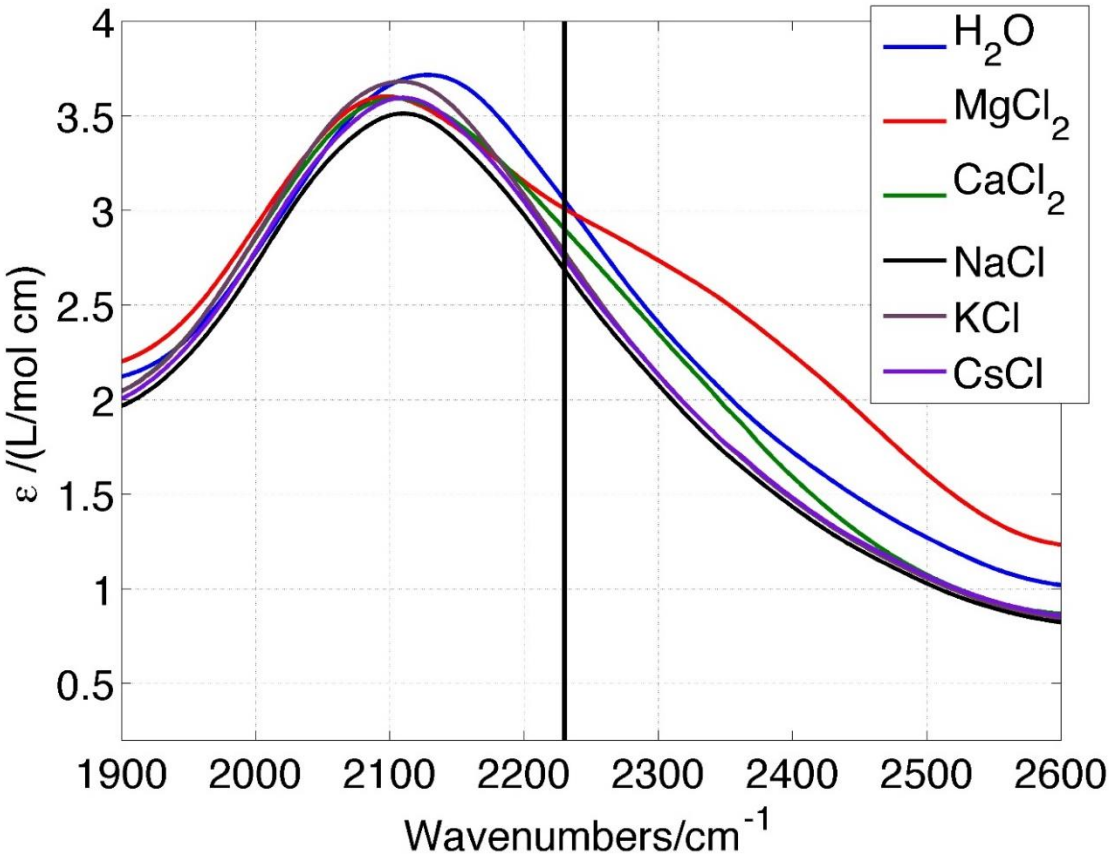

Figure 2.8 - FTIR spectrum of the bend-libration region of the indicated 2M salts compared to that of neat H_2O. The cation dependent spectrum consists of the water bend-libration transition and an underlying continuum absorption. The solid black vertical line marks the N_2O ν_3 fundamental transition peak frequency (~2230 cm^{-1}).

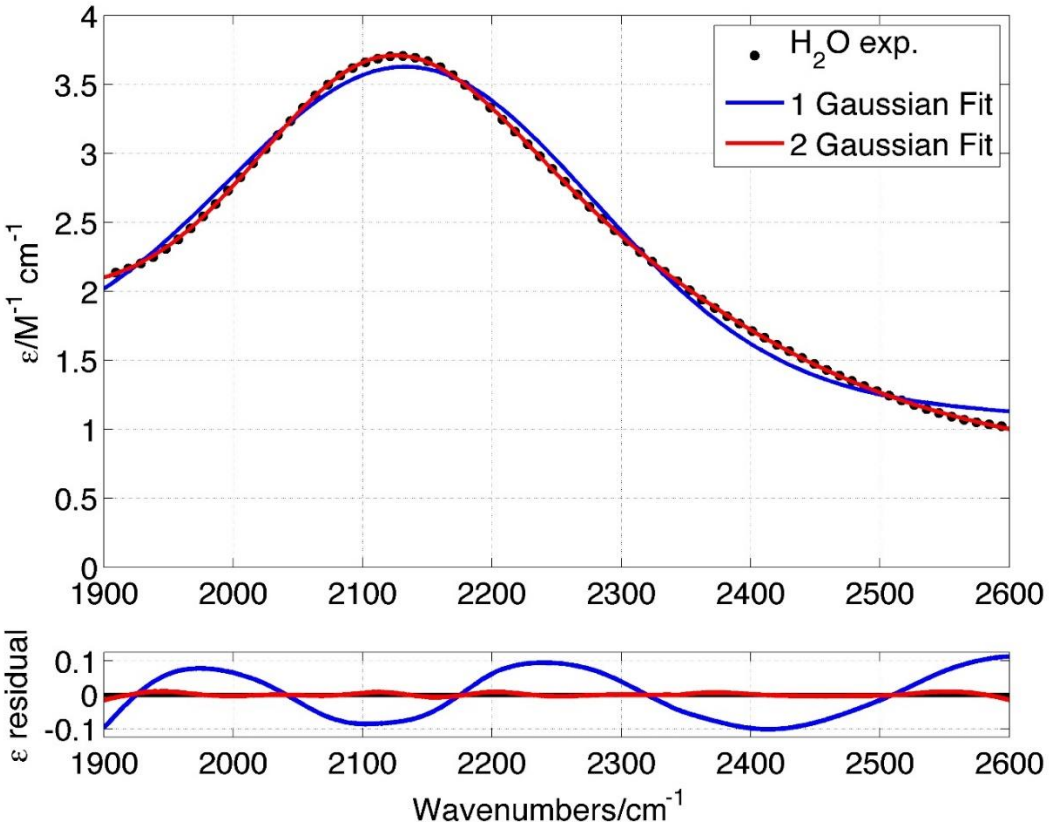

Figure 2.9 - Results of best fitting the bend-libration ($\nu_2 + \nu_L$) band of water to a single Gaussian (blue) or two Gaussian (red) model which also includes a linear baseline term to capture the continuum contribution in this spectra region. Corresponding residuals plotted in the lower panel indicate that a single Gaussian is not sufficient to phenomenologically capture this band shape.

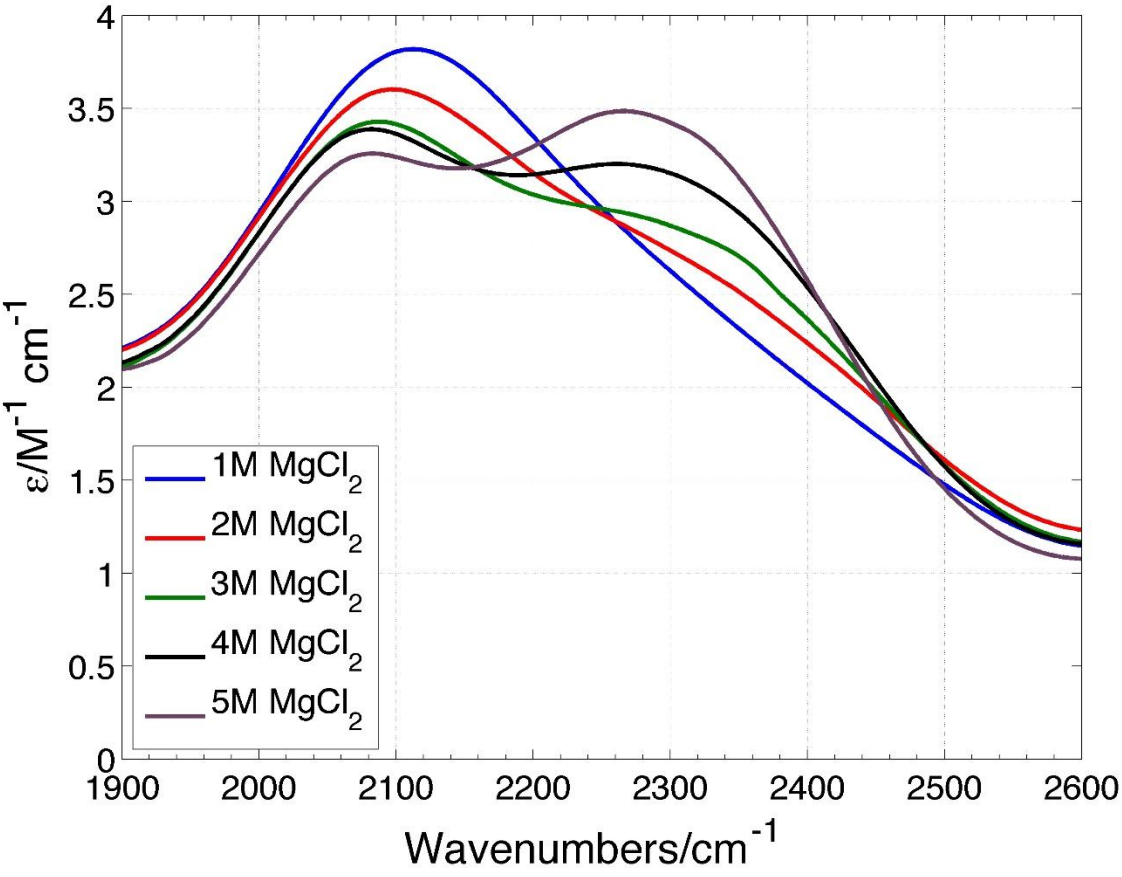

Figure 2.10 - Water absorption spectrum in the bend-libration ($\nu_2 + \nu_L$) region as a function of $MaCl_2$ concentration. The dramatic increase of a second Gaussian contribution on the blue side of this absorption feature is evident with increasing $MgCl_2$ concentration in the 1 – 5 M range.

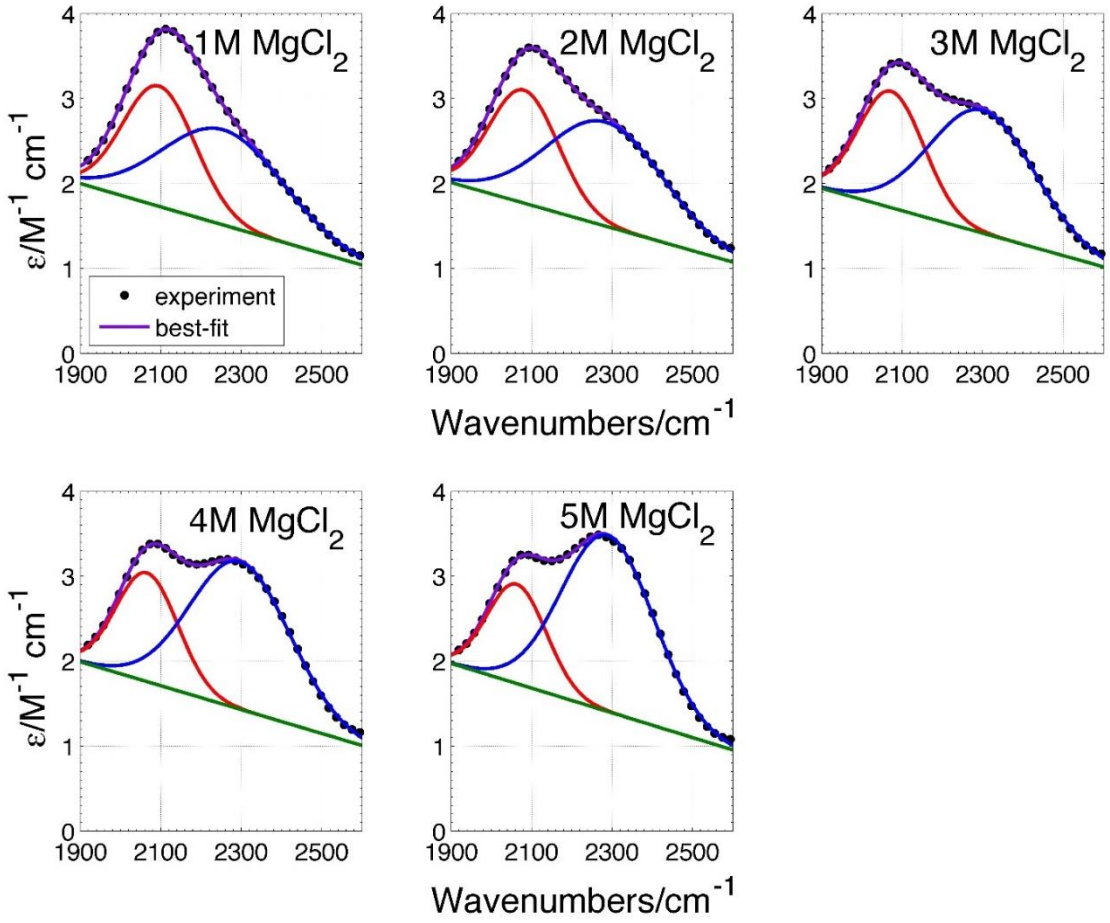

Figure 2.11 - The resulting two Gaussians (red and blue) plus a sloping baseline (green) best-fit (purple) to the water bend-libration ($\nu_2 + \nu_L$) absorption band as compared to the observed spectrum (dots) is shown as a function of $MgCl_2$ concentration.

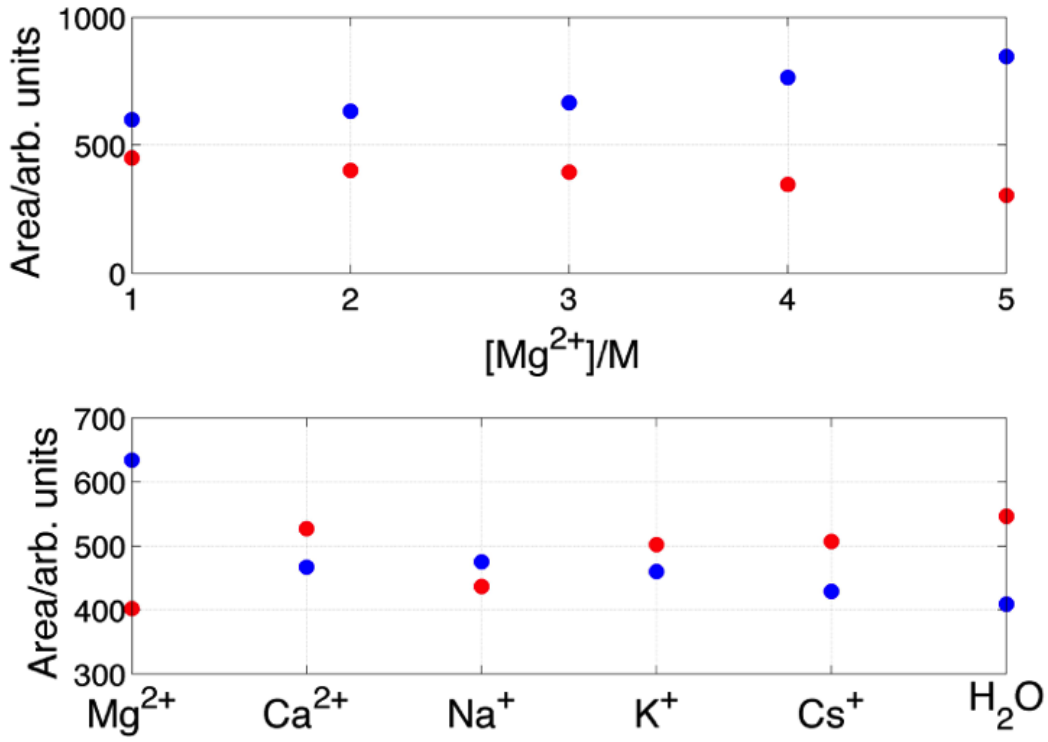

Figure 2.12: The upper panel shows the $MgCl_2$ concentration dependence of the two Gaussian contributions, as given by the area of these best-fit determined components, to the broad bend-libration combination absorption band of water. The total area of this absorption band given by the sum of these two Gaussians is $MgCl_2$ concentration independent within the precision of these measurements (±1%). The relative area of the two Gaussians resulting from the best-fit of the bend-libration combination absorption band of water for the indicated series of 2M cations (chlorides) as given in the lower panel. The total area (intensity) of this band, given by the sum of these two components changes by only ≤ 10% for this series of 2M salts although the distribution of intensities changes by a larger amount as a function of cation. The bluer/redder component increases/decreases relative to water as a function of "structure making" strength except for the change between monovalent Na^+ and divalent Ca^+.

Table 2.1 - Some physical macroscopic properties of aqueous ions.

	Ionic volume[a] (cm^3/mol)	B_J coefficient (M^{-1})[b]	$\Delta S_{hydration}$[c] (kJ mol^{-1})	ΔG_{HB}[d]
Mg^{2+}	–21.17	+0.385	–174	0.9 to 1.1
Ca^{2+}	–17.85	+0.284	–132	0.4 to 0.7
Na^+	–1.21	+0.085	–5	–0.1 to 0.1
K^+	+9.02	–0.009	+34	–0.9 to –0.7
Cs^+	+21.35	–0.047	+59	–0.9 to –0.7
Cl^-	+17.83	–0.005	+6	–0.9 to –0.7

structure makers ↑ ↓ structure breakers

[a]Partial molal volume of ions in H_2O at 298K relative to pure water (H^+ = 0.0).[87] [b]Jones-Dole viscosity B-coefficients of ions at 25 °C.[88-89] [c]This measure of the structural entropy is defined by the standard (298 K) molar entropy of hydration minus the entropy of the primary water hydration shell.[90] [d]An empirically derived factor describing the effect of a solute on the hydrogen-bonding structure of liquid water. In this notation, $\Delta G_{HB} \leq -0.1$ and $\Delta G_{HB} \geq +0.1$ correspond to "structure breakers" and "structure makers", respectively. $-0.1 \leq \Delta G_{HB} \leq 0.1$ are borderline ions by this criterion.[89]

Table 2.2 – Observed N_2O ν_3 peak position and width (FWHH) in several 2M aqueous salt solutions and pure H_2O.

	Peak Frequency[a]/cm^{-1} (ΔH_2O)	*FWHH[a]/cm^{-1} (ΔH_2O)*
H_2O	2229.7	11.0
$MgCl_2$	2231.0 (+1.3)	12.4 (+1.4)
$CaCl_2$	2230.8 (+1.1)	11.2 (+0.2)
NaCl	2231.1 (+1.4)	12.0 (+1.0)
CsCl	2231.7 (+2.0)	12.5 (+1.5)

[88] [a]Estimated precision ± 0.1 cm^{-1}

Table 2.3 – N_2O ν_3 lifetimes in 2M aqueous chloride salt solutions and best-fit parameters for FTIR spectrum of the bend-libration combination band region (1900 cm^{-1} – 2600 cm^{-1}) in water with dissolved salts. The spectral density is approximated as a sum of a sloped, linear baseline contribution and two Gaussians with center frequencies ω_R and ω_B and areas (arb. units A_R and A_B).

Cation	T_1 /ps[a]	ω_R/cm^{-1}	A_R	*FWHM* /cm^{-1}	ω_B/cm^{-1}	A_B	*FWHM* /cm^{-1}	$\nu_2+\nu_L$ A_{Tot}	*Continuum (2230* cm^{-1}*)*	*Total (2230* cm^{-1}*)*	G_R *(2230* cm^{-1}*)*	G_B *(2230* cm^{-1}*)*
Mg^{2+}	11.6	2081	402	201	2283	634	344	1036	1.57	3.00	0.29	1.14
Ca^{2+}	10.1	2082	527	219	2247	467	276	994	1.34	2.88	0.43	1.11
Na^{+}	9.3	2092	437	218	2208	474	323	911	1.30	2.69	0.40	0.96
H_2O	9.0	2111	546	231	2250	409	325	956	1.45	3.04	0.71	0.84
K^{+}	8.8	2091	502	221	2214	460	320	962	1.31	2.75	0.48	0.96
Cs^{+}	7.6	2092	507	224	2223	429	318	936	1.29	2.74	0.54	0.91

[a]Estimated precision ± 0.3 ps.

Table 2.4 - Corresponding best-fit determined fitting parameters (2 Gaussian + baseline model)

$[MgCl_2]$	ω_R/cm^{-1}	$FWHM_R$	$Area_R$	ω_B/cm^{-1}	$FWHM_B$	$Area_B$	$Area_{Total}$	*Continuum @2230* cm^{-1}
1 M	2095	211	450	2255	356	601	1051	1.54
2 M	2081	201	402	2283	344	634	1036	1.57
3 M	2072	191	395	2300	306	667	1062	1.51
4 M	2066	180	347	2296	292	765	1112	1.53
5 M	2063	104	304	2289	271	846	1149	1.49

Chapter 3: Ultrafast Two-Dimensional Infrared Spectroscopy of a Quasifree Rotor: *J* Scrambling and Perfectly Anticorrelated Cross Peaks[91]

3.1 Introduction

Over the last two decades, ultrafast two-dimensional infrared (2DIR) spectroscopy has emerged as one of the leading techniques for investigation of molecular structure and dynamics in condensed phases.[92-93] 2DIR spectral analysis yields information on molecular fluctuation time scales and mechanisms responsible for IR absorption line shapes, the coupling of resonant intra- or intermolecular modes or the dynamics of chemical exchange between interconverting molecular configurations or species.[92-108] For a single vibrational resonance the 2DIR spectrum consists of two oppositely signed features: ground state bleach and stimulated emission (GSB-SE) contributions centered along the diagonal, and an excited vibrational state absorption (ESA) contribution shifted along the probe frequency axis by the vibrational anharmonicity. Molecular fluctuation time scales due to bath interactions in these condensed phase systems are revealed by

The waiting time (T_w) dependence of the 2DIR line shapes and correspond to the transition frequency-frequency correlation function (FFCF) of a resonantly excited vibrational mode.[109]

We report here the first observations and analysis of 2DIR spectra of a quasi-free quantum rotor in a moderately dense gaseous medium. 2DIR spectra of the resonantly excited ν_3 asymmetric stretching rovibrational band of N_2O in SF_6 at two densities (ρ^* =

ρ/ρ_c = 0.16 and 0.30; ρ_c = 0.74 g/mL = 5.79M) have been obtained. Aside from providing a rovibrationally specific framework for understanding the observed complex 2DIR spectral line shapes, these spectra demonstrate a new capability for measuring ultrafast rovibrational relaxation dynamics in the absence of discrete rotational resolution. Furthermore, characterization of the quasi-free rotor 2DIR spectrum is required for studies of solvation in higher density solutions where critical point fluctuation dynamics may be evident ($\rho^* \sim 1$) and for learning about the onset of liquidlike character ($\rho^* > 1$) as a function of density.

3.2 Experimental

Sample Preparation

Solutions used for the SF_6 studies were prepared in a custom variable path-length stainless steel sample cell diagrammed in Fig x. The sample cell uses 2 mm calcium fluoride windows and a 100μm Teflon spacer in a U-shape to allow for gas to flow into the optical chamber. To accommodate the higher pressure and temperatures Viton O-rings (McMaster Carr) were used. The pressure was measured using a PX-602/3 pressure transducer (Omega Engineering) and protected using a pressure scrubber. Heating was achieved using a rope heater (Omega Engineering) using a heating control box with a feedback loop passed through a rheostat. The rope heater was wrapped around the body of the sample cell and the attached tubing to achieve the state points mentioned. A temperature probe was screwed into the body of the sample cell to effectively measure the temperature closest to the optical area.

Nitrous oxide (Airgas) used was of 99.98% purity. Sulfur Hexafluoride (Praxair) was obtained at 99.98% purity. Testing was done to get the optimal fill ratios. First, the sample cell and high pressure gas setup was vacuumed to less than 200 mtorr. For the below supercritical samples, the N_2O was filled to ~45 psi in the sample cell. The sample cell was closed off and the rest of the system was vacuumed again to below 200 mtorr. SF_6 was then filled into the pressure generator at tank pressure, ~300 psi. The sample cell and pressure generator were then equilibrated, dropping the overall pressure to ~200 psi. The pressure generator allowed for compression of the gas up to 60 mL. The pressure was increased to the desired state point. If the pressure was not at the correct level, the sample cell was closed off, the pressure generator was vacuumed and filled with more SF_6. This was repeated until the desired pressure was achieved. For those state points above room temperature, the pressure generator was also wrapped in a heating rope along with the sample cell. Everything was heated and let equilibrate for 1 hour before compression in order to get proper mixing and to avoid cold pockets where the SF_6 could potentially condense into liquid.

These spectra were acquired in a pump-probe configuration, and thus rephasing and nonrephasing signals are overlapped at the detector.[110] Perpendicularly polarized 85 fs pulses (FWHM = 250 cm^{-1}) centered at ~2230 cm^{-1} were used to acquire these spectra. The rapid scan, phase corrected coherence delay between the first two pump pulses (τ_1) was Fourier transformed to give the ω_1 axis and the dispersed signal on a 32 element array (~3 cm^{-1}/pixel) corresponds to the ω_3 axis.

3.3 Results and Discussion

The FTIR (Fourier transform infrared) spectrum of the N_2O ν_3 mode at T = 313 K in 26 atm of SF6 (ρ^* = 0.30, 2.6% N_2O) is shown in **Figure 3.1**. The corresponding spectrum of N_2O in lower density SF_6 (17 atm, ρ^* = 0.16, 4% N_2O) is slightly narrower. (**Figure 3.2**). The maxima at 2211 and 2236 cm^{-1} correspond to the unresolved P ($\Delta J = -1$) and R ($\Delta J = +1$) rovibrational branches, respectively, originating from the thermalized ensemble of initial rotational levels, J. The pure ($\Delta J = 0$) $0 \rightarrow 1$ ν_3 vibrational transition, i.e., the Q branch, would be centered at ~2224 cm^{-1} but is formally forbidden for a linear molecule in free space.[111-112] The rovibrational structure for this single vibrational resonance (Fig. 3.1) stands in contrast to the single maximum line shape observed for the N_2O ν_3 transition in liquid solutions (**Figure 3.2**).[60]

The corresponding observed 2DIR spectra of the N_2O ν_3 mode in SF6 (ρ^* = 0.30) are shown in Fig. 2 for T_w = 0.2, 5.0, and 30 ps. The T_w dependent 2DIR spectra of the lower density (ρ^* = 0.16) N_2O/SF_6 mixture have a qualitatively similar appearance. The ν_3 ν = 1 lifetimes in these solutions, determined by magic angle pump-probe responses, (ρ^* = 0.30; 35 ps and ~1 ns, and for ρ^* = 0.16; 101 ps and ≥10 ns) are much slower than the dynamics revealed in these 2DIR spectra.

The quasi-free rotor 2DIR spectra (**Figure 3.3**) exhibit a qualitatively different and considerably more complex spectral signature than seen for 2DIR spectra of isolated vibrational resonances in condensed phases.[113-116] The sign change and spacing between the center of red and blue overlapping "X"s at the shorter T_w's identifies the red

(positive) and blue (negative) 2DIR features resulting from GSB-SE and ESA contributions to the N_2O/SF_6 2DIR spectra. The elongated spectral shape along the diagonal ($\omega_1 = \omega_3$) and the parallel component redshifted in the $\omega 3$ direction by the ν_3 1 $\rightarrow$ 2 transition anharmonicity ($\sim$28 cm^{-1}) at T_w = 0.2 ps, are the well-known signatures of an inhomogeneously broadened vibrational band in 2DIR spectra. The corresponding antidiagonal features seen in these quasi-free rotor spectra are unique relative to previous 2DIR results; however, they are reminiscent of the 2DIR spectrum predicted for two anticorrelated inhomogeneously broadened coupled oscillators.[117-118] The "X" pattern is evident in a prior 2D rovibronic, low density coherent 4-wave mixing spectroscopy that assists interpretation and simplification of gas phase spectra.[119]

Dramatic changes are seen in these 2DIR spectra (**Figure 3.3 and 3.4**) as a function of T_w. All the initial (T_w = 0.2 ps) elongated features approach nearly symmetrical shapes at longer T_w's which is the well-known signature of transition frequency memory loss, characteristic of spectral diffusion processes in liquid phase environments. Furthermore, the eight spectral features in the 2DIR spectra (4 bleach and 4 absorption types) at the earliest T_w's evolve to 4 distinct features at $T_w \geq 30$ ps. As shown previously, a change in the aspect ratio of the 2DIR spectral line shapes corresponding to the a $\rightarrow$ b transition as a function of T_w closely captures the decay of the FFCF.[109] Thus, the center line slope (CLS), also plotted in **Figure 3.3**, experimentally determines FFCF for both the diagonal and antidiagonal GSB-SE components of the 2DIR spectra. The CLS decay has different signs for the diagonal and antidiagonal

components, but both show the same dominant exponential decay constant within experimental error: 6.1 ± 0.3 ps (diagonal) and 5.8 ± 0.4 ps (antidiagonal). Similarly, the CLS decay times for the lower density ($\rho^* = 0.16$) sample (**Figure 3.5**) are 9.4 ± 0.3 ps (diagonal) and 9.5 ± 0.6 ps (antidiagonal). However, best fits to all these experimental CLS decays also find a small (~5% of total amplitude) positive constant component for the diagonal and anti-diagonal 2DIR GSB-SE features. This small residual offset or very slow fluctuation component may be attributable to pure vibrational dephasing processes (here due to a static inhomogeneity on the experimental time scale), sample heating effects or consequences of the canceling effects of adjacent, oppositely signed 2DIR contributions.

In order to capture the essential features of the observed quasifree rotor 2DIR spectra and provide a basis for interpreting the observed T_w dependence in terms of the underlying rotationally and vibrationally specific collision dynamics, a phenomenological model was developed. The 2DIR signal generated in the $k_{sig} = k_{probe}$ direction for the pump-probe experimental configuration employed here is given by :

$$S(k_{sig}; \omega_3, T_w, \omega_1) \propto \mathrm{Re}\left(\iint_{-\infty}^{\infty} R_{Tot}^{(3)}(\tau_3, T_w, \tau_1)\, e^{i\omega_1\tau_1} e^{i\omega_3\tau_3} d\tau_1 d\tau_3 \right) \qquad (3.1)$$

where τ_1, T_w, and τ_3 are the delays between the two pump pulses; the second pump and the probe pulses; and the $P^{(3)}$ signal detection time, respectively. Since the incident pulse durations (~85 fs) are much shorter than the dynamics observed here, only the intervals between pulse maxima are used for τ_1, T_w, and τ_3. For a single vibrational resonance only a three level, optically coupled system, consisting of the ground ($v = 0$), and first and

second (ν = 1, 2) excited vibrational states, is needed to model the 2DIR signal. Consequently, six Liouville pathways, within the rotating wave approximation, due to spatially overlapped rephasing ($-k_{pump} + k_{pump +} k_{probe}$) and nonrephasing ($+k_{pump} - k_{pump} + k_{probe}$) contributions result for well-separated pulses.[120] However, for an initial rotational level J in ν = 0, i.e., $|0J>$, an eight rovibrational level system, $|\nu J>$, is required to calculate the 2DIR spectrum of a quantum free rotor. A 2DIR signal pathway originating in $|0J> (\equiv 0)$ has two accessible rovibrational levels in the ν = 1 excited state ($|J+1>= 1R$ and $|1J-1>= 1P$), three in the ν = 2 second excited state ($|2J+2>\equiv 2S, |2J>\equiv 2Q, |2J-2>= 2O$) and three in the ground vibrational state ($|0J+2>\equiv 0S, |0J>\equiv 0,$ and $|0, J-2>\equiv 0O$) due to the ΔJ = ±1 selection rule for each Δν = ±1 dipole interaction in this third-order experiment. (**Figure 3.6**). Consequently, there are six rovibrationally explicit Liouville pathways possible for each of the usually considered six types of Liouville pathways contributing to the 2DIR spectrum of an isolated vibrational oscillator.[92, 117] Thus, the total third-order response function for the description of a 2DIR spectrum of a rovibrational resonance originating in a single rovibrational level for nonoverlapped pump and probe pulses is modeled as a sum of 36 rovibrationally explicit Liouville pathways:

$$R_{Tot}^{(3)}(\tau_3, T_w, \tau_1) = \sum_{n=1}^{36} R_n^{(3)}(\tau_3, T_w, \tau_1) \tag{3.2}$$

Twelve such representative pathways showing the temporal evolution from left to right of the density matrix elements contributing to the signal polarization[121-123] are

shown in **Figure 3.7**, and all 36 of these pathways are summarized in **Figure 3.8**. Expressions for the third-order responses contributing to vibrational 2DIR spectra have been described in detail previously,[117] thus only those features most salient to their extension to this rovibrational system are summarized here. Each of the 36 contributing rovibrational response functions are a product of four path-specific transition moments, exponential oscillatory phase factors at the resonant transition frequencies during each of the interpulse evolution periods (τ_1, T_w, τ_3), and a path-specific nonlinear dephasing function.[124-125] The required dephasing functions can be written as products of exponentiated line shape functions, $g_{ab}(t)$, which are defined in terms of the a → b FFCF, $C_{a,b}(\tau_2 - \tau_1)$, within the second order cumulant expansion approximation:[126]

$$g_{ab}(t) = \int_0^t d\tau_2 \int_0^{\tau_2} d\tau_1 C_{a,b}(\tau_2 - \tau_1) \tag{3.3}$$

The FFCF is determined by the underlying fluctuation dynamics of the system and is one of the key quantities determined by 2DIR spectral analysis.[92, 109] The required rovibrationally explicit FFCFs are given by:

$$C_{n\alpha,n'\beta}(t) = \langle \delta\omega_{n0}^{\alpha}(t)\delta\omega_{n'0}^{\beta}(0)\rangle = \zeta_{n\alpha,n'\beta}\Delta_{n0}^{\alpha}\Delta_{n'0}^{\beta}e^{-\frac{t}{\tau_c}} \tag{3.4}$$

where n, n' refer to vibrational levels 0, 1, or 2, and α, β are the corresponding rotational branches. For $n, n' = 1, \alpha, \beta = P$ or $R(\Delta J = -1, +1)$; for $n, n' = 0$ or $2, \alpha, \beta = O, Q,$ or $S(\Delta J = -2, 0,$ or, $+2)$. In this stochastic Gaussian line broadening model,[127] the time dependent fluctuations of the rovibrational transition frequencies, here due to gas collisions, $\delta\omega_{n0}^{\alpha}$, are defined relative to some corresponding ensemble averaged value

ω_{n0}^{α}, i.e., $\omega_{n0}^{\alpha}(t) = \omega_{n0}^{\alpha^0} + \delta\omega_{n0}^{\alpha}(t)$. Δ_{n0}^{α} etc. [Eq. (3.4)], are the initial instantaneous widths of the corresponding 0 → n rovibrational (α) branches, and τ_C is the transition energy fluctuation time scale. $\zeta_{n\alpha,n'\beta}$ is the correlation coefficient[117, 128-129] describing the relative phasing of the fluctuations or distributions between $n\alpha, n'\beta$ rovibrational branches. The total FFCF decay may result from multiple fluctuation mechanisms [Eq. 3.4]. Although 14 rovibrationally explicit FFCFs, $C_{n\alpha,n'\beta}(t)$ are formally required to calculate the 2DIR spectrum of a free rotor, these may all be given in terms of three, unique 0 → 1 rovibrational FFCFs: $C_{1R,1R}(t), C_{1P,1P}(t),$ and $C_{1R,1P}(t)$, assuming negligible fluctuation in vibrational anharmonicity[117]; see Supplemental Material.

In order to capture the effects of spectral diffusion within the unresolved N_2O ν_3 rovibrational branches (**Figure 3.1**) $\omega_{10}^{R^0}$ and $\omega_{10}^{P^0}$ are taken as the transition energy at each of the two ν_3 fundamental absorption branch maxima, and Δ_{10}^{P} and Δ_{10}^{R} are the corresponding inhomogeneous breadths of the P and R branches (**Figure 3.1**). The branch maxima correspond to the P(15) and R(15) transition frequencies at 313 K and thus J = 15 is taken to be the initial rotational level in the ground vibrational state in this 2DIR rovibrational analysis. This treatment is analogous to modeling the line broadening of a single vibrational oscillator due to solvent fluctuations of the vibrational energy gaps about an ensemble averaged vibrational transition frequency and the loss of frequency memory for a single vibrational oscillator (spectral diffusion). This rovibrational model, equivalently, allows for J memory loss or J spectral diffusion[126-127] due to bath interactions (collisions).

The ratio of 1 → 2 and 0 → 1 vibrational transition moments, given within the Condon approximation, used in this calculation is $\sqrt{1.6}$ as evident in the observed pump-probe responses and the rotational contribution to the rovibrational transition dipole is given by $\sqrt{\max(J, J')}$ where J and J' are the rotational quantum numbers of the rovibrational levels involved in the transition. By definition, $C_{n\alpha,n'\beta} = +1$ for autocorrelation functions $(\alpha = \beta)$, $C_{1R,1R}(t)$ and $C_{1P,1P}(t)$. However, for the cross-correlation functions (α ≠ β), $\zeta_{1R,1P} = -1$ since for any J value, $\delta\omega_{10}^{R}(t)\delta\omega_{10}^{P}(0) < 0$ and, consequently, $C_{1R,1P}(t)$ is perfectly anticorrelated. Detailed expressions for each of the 36 response functions $[R_n^{(3)}(\tau_3, T_w, \tau_1)]$ are given in the next section

Calculated 2DIR spectra for the ν_3 mode of N_2O in SF_6 ($\rho^* = 0.30$) resulting from the model outlined above are shown in **Figure 3.3** as a function of T_w and closely capture the structure of the experimental 2DIR spectra and their T_w dependence. The corresponding calculated linear absorption spectrum is shown in **Figure 3.1**. Similar agreement between observed and calculated 2DIR results are found for the less dense ρ^* = 0.16 solution (**Figure 3.3**). Parameters for these calculated 1D and 2D spectra are summarized in **Table 3.1** and **Table 3.5** The values of Δ_{10}^{P} and Δ_{10}^{R} were selected to capture the linear spectral shape in the central portion of the rovibrational absorption band (**Figure 3.1** and **Figure 3.2**). Given the Gaussian distribution of the instantaneous frequencies inherent to this line broadening model, poor fits in the wings of the experimental asymmetric rovibrational spectrum are expected. However, although not rigorously exact for capturing the shape of the instantaneous transition frequency

distribution or any J-specific collision dynamics, the essential features of the observed linear and nonlinear spectra are well described by this analysis and can be understood in terms of spectral diffusion and the rovibrationally specific 2DIR pathways (**Figure 3.7**). In particular, the antidiagonal 2DIR spectral features evident for both the GSB-SE and ESA contributions at early times, and the observed J scrambling as a function of T_w are captured by this treatment. Subsequent more rigorous treatments of these 2DIR observations will have to take a full quantum level specific treatment of coherence loss and J-state changing dynamics into account.

The 36 rovibrational Liouville pathways give rise to twelve unique signal peaks in the 2DIR spectrum in this model. The twelve red (GSB-SE) and blue (ESA) labeled circles on the 2DIR spectral map in **Figure 3.9** indicate these signal locations and the number identifies a specific signal pathway from **Figure 3.7** contributing to the 2DIR spectrum at that (ω_1, ω_3) position. These signals are centered at the fundamental R (ω_{10}^{R}) and P (ω_{10}^{P}) branch transitions along the ω_1 axis and at 8 signal frequencies along the ω_3 detection axis (**Figure 3.9**). However, due to the small dependence of rotational constants on vibrational level ($B_0 \approx B_1 \approx B_2$) and lack of discrete rotational resolution at these densities, only 4 signal frequencies are distinguishable along ω_3: $\omega_{10}^{R} \approx \omega_{10}^{R'}, \omega_{10}^{P} \approx \omega_{10}^{P'}, \omega_{21}^{R} \approx \omega_{21}^{R'}$, and $\omega_{21}^{P} \approx \omega_{21}^{P'}$ (**Figure 3.9**). Hence, in contrast to the 2DIR spectra of isolated vibrational resonances in condensed phase environments characterized by a single T_w dependent GSB-SE and ESA spectral component, the 2DIR spectrum of a free rotor exhibits at least 4 GSB-SE and 4 ESA features. The elongated shapes observed at

shorter T_w's for these 8 2DIR spectral regions are due to the initial predominant inhomogeneous character due to the ensemble of J-specific allowed rovibrational transitions. Arguably, the most obvious signature in a 2DIR spectrum of free rotor character are the anti-diagonally elongated spectral features, which result in X-like cross peaks at early times (**Figure 3.3** and **Figure 3.9**). These features result from the inherent perfectly anticorrelated cross-correlation contributions, $\zeta_{1R,1P} = -1$, i.e., where $C_{1R,1P}(t) = \langle \delta\omega_{10}^{R}(t)\delta\omega_{10}^{P}(0)\rangle = \Delta_{10}^{R}\Delta_{10}^{P}e^{-t/\tau_c}$. Such perfectly anticorrelated FFCFs are unique to this quantum rotor description. The diagonally and antidiagonally elongated line shapes at early T_w's, symmetrize at longer times as observed both in the experiments and calculations. Only 4 spectral features are evident at longer T_w's because the N_2O ν_3 vibrational anharmonicity (28 cm^{-1}) almost exactly matches the frequency difference between P and R branch maxima (25 cm^{-1}). Consequently, the symmetrized diagonal GSB-SE contribution of the P transition (pathway 20) almost exactly cancels the (*P*,*R*) ESA cross–peak (pathway 29), and the cross peak (*R*, *P*) GSB-SE signals (pathways 21, 23) effectively cancel the ESA of the R transitions (pathways 25 and 28). Such intensity cancellation from these same signal polarization pathways results in the two nodes at approximately earliest time 2DIR spectra (**Figure 3.3**).

3.4 Calculation of Ro-Vibrational Response Functions

In order to calculate the total 3rd order response function generating the 2DIR spectrum of a system, the transition frequencies, transition dipoles and dephasing functions are required for each of the contributing pathways.[125] For the (quasi) free rotor

system considered in this work, there are 6 general types of pathways for non-overlapping pulses that contribute to the 2DIR signal, as depicted in **Figure 3.11**. The contributions of these general types of pathways towards to the total 3rd order response function are given by:

$$R_I^{(3)}(\tau_3,T_w,\tau_1)=\frac{1}{\hbar^3}\left[P_a\mu_{da}\mu_{cd}\mu_{bc}\mu_{ab}e^{-i\omega_{da}\tau_1}e^{-i\omega_{ca}T_w}e^{-i\omega_{ba}\tau_3}F_{abcd}^{(1)}(\tau_3,T_w,\tau_1)-c.c.\right]$$

$$R_{II}^{(3)}(\tau_3,T_w,\tau_1)=\frac{1}{\hbar^3}\left[P_a\mu_{da}\mu_{ab}\mu_{bc}\mu_{cd}e^{-i\omega_{da}\tau_1}e^{-i\omega_{db}T_w}e^{-i\omega_{dc}\tau_3}F_{abcd}^{(2)}(\tau_3,T_w,\tau_1)-c.c.\right]$$

$$R_{III}^{(3)}(\tau_3,T_w,\tau_1)=\frac{1}{\hbar^3}\left[P_a\mu_{ad}\mu_{dc}\mu_{ba}\mu_{cb}e^{+i\omega_{da}\tau_1}e^{+i\omega_{ca}T_w}e^{-i\omega_{bc}\tau_3}F_{abcd}^{(3)}(\tau_3,T_w,\tau_1)-c.c.\right] \quad (3.5)$$

$$R_{IV}^{(3)}(\tau_3,T_w,\tau_1)=\frac{1}{\hbar^3}\left[P_a\mu_{ad}\mu_{ba}\mu_{dc}\mu_{cb}e^{+i\omega_{da}\tau_1}e^{+i\omega_{db}T_w}e^{-i\omega_{bc}\tau_3}F_{abcd}^{(4)}(\tau_3,T_w,\tau_1)-c.c.\right]$$

$$R_V^{(3)}(\tau_3,T_w,\tau_1)=-\frac{1}{\hbar^3}\left[P_a\mu_{da}\mu_{ab}\mu_{cd}\mu_{bc}e^{-i\omega_{da}\tau_1}e^{-i\omega_{db}T_w}e^{-i\omega_{cb}\tau_3}\left[F_{abcd}^{(4)}(\tau_3,T_w,\tau_1)\right]^*-c.c.\right]$$

$$R_{VI}^{(3)}(\tau_3,T_w,\tau_1)=-\frac{1}{\hbar^3}\left[P_a\mu_{ad}\mu_{ba}\mu_{cb}\mu_{dc}e^{+i\omega_{da}\tau_1}e^{+i\omega_{db}T_w}e^{-i\omega_{cd}\tau_3}\left[F_{abcd}^{(2)}(\tau_3,T_w,\tau_1)\right]^*-c.c.\right]$$

Where, P_a is the initial population in the eigenstate $|a\rangle$; μ_{ij} is the transition dipole corresponding to the $|i\rangle \rightarrow |j\rangle$ transition $i,j=a,b,c,d$); $\omega_{ji}=\omega_j-\omega_i$ is the oscillation frequency of the coherence (or population if $j=i$) $|j\rangle\langle i|$ that propagates during the time delay τ_a or T_w ($i,j=a,b,c,d$ *and* $\alpha=1$ or 3) and $F_{abcd}^{(m)}(\tau_3,T_w,\tau_1)$ ($m=1,2,3,4$) are the dephasing functions. The peaks in the 2DIR spectra at a waiting time T_w appear at frequencies (ω_1,ω_3), corresponding to the oscillation frequencies of the coherences during time delay τ_1 and τ_3, respectively.

For the free rotor system considered in this work, each of the 6 general types of pathways contributing to the 2DIR signal consists of 6 rovibrationally-specific pathways, as shown in **Figure 3.8**. Detailed expressions for transition frequencies, transition dipoles

and dephasing functions required for evaluation of the total 3rd order response function from the 36 rovibrational pathways (**Figure 3.8**) are provided in the following subsections.

Transition frequencies and transition dipoles

The rotational contributions to the rovibrational transition energies are given by the familiar rigid rotor energies for the ground, first and second excited vibrational states of a linear rotor (Eq. 3.6):

$$\begin{aligned} E_0(J) &= \hbar[B_0 J(J+1)] \\ E_1(J) &= \hbar[\omega_{10} + B_1 J(J+1)] \\ E_2(J) &= \hbar[\omega_{10} + \omega_{21} + B_2 J(J+1)] \end{aligned} \tag{3.6}$$

Where $B_0, B_1, and\ B_2$ are the ground, first and second excited vibrational state rotational constants, respectively, of the linear rotor, ω_{10} and ω_{21} are the fundamental and anharmonically shifted $\nu = 1 \rightarrow \nu = 2$ transition frequencies for the N_2O antisymmetric stretching mode vibration (ν_3). The effects of centrifugal distortion have been neglected in this treatment due to their relatively small magnitude. Eight unique signal frequencies (ω_3) are generated in the 2DIR spectra of this system contributed by all the 36 possible rovibrational pathways (**Figure 3.8**) and are summarized below:

$$\begin{aligned} \omega_{10}^{R} &= [\omega_{10} + B_1(J+1)(J+2) - B_0 J(J+1)] \\ \omega_{10}^{P} &= [\omega_{10} + B_1(J-1)J - B_0 J(J+1)] \\ \omega_{10}^{R'} &= [\omega_{10} + B_1(J-1)j - B_0(J-2)(J-1)] \\ \omega_{10}^{P'} &= [\omega_{10} + B_1(J+1)(J+2) - B_0(J+2)(J+3)] \end{aligned} \tag{3.7}$$

$$\omega_{21}^{R} = [\omega_{21} + B_2(J+2)(J+3) - B_0(J+1)(J+2]$$

$$\omega_{21}^{P} = [\omega_{21} + B_2(J-2)(J-1) - B_1J(J-1)J]$$

$$\omega_{21}^{R'} = [\omega_{21} + B_2J(J+1) - B_0J(J+1)]$$

$$\omega_{21}^{P'} = [\omega_{21} + B_2J(J+1) - B_1(J+1)(J+2)]$$

The transition frequencies at which the coherences (or population at T_w which oscillate at 0 frequency) oscillate at each of the three time intervals are listed in **Table 3.2** for all the 36 pathways originating in a single ground state rovibrational level *J*. We note that in contrast to the description of the 2DIR response function for an isolated vibrational resonance in condensed phase, some density matrix pathways have coherences propagating during T_w corresponding to low frequency rotational energy gaps.

Only four of the unique ω_3 signal frequencies are distinguishable in the 2DIR spectrum given the inherent resolution of this experiment: $\omega_{10}^{R}, \omega_{10}^{P}, \omega_{21}^{R}, \text{and } \omega_{21}^{P}$; i.e. $\omega_{10}^{R} \approx \omega_{10}^{R'}$, $\omega_{10}^{P} \approx \omega_{10}^{P'}$, $\omega_{21}^{R} \approx \omega_{21}^{R'}, \text{and } \omega_{21}^{P} \approx \omega_{21}^{P'}$. For example, $\left(\omega_{10}^{R} - \omega_{10}^{R'}\right) = [2(B_0 + B_1) - 4J(B_0 - B_1) \approx O\left(\frac{3B}{2}\right)$. Since $\frac{3B}{2}$ is much smaller than the linewidths of the 2DIR peaks, only 4 ω_3 transition frequencies are distinguishable in these 2DIR spectra.

The product of 4 different transition dipoles are required to compute the 3rd order response function for each of the 36 2DIR pathways shown in **Figure 3.8**. The $|a,J\rangle \rightarrow |b,J'\rangle$ rovibrational transition dipole is given by $\mu_{ab} \times \sqrt{\max(J,J')}$. Since each transition dipole appears multiplied by its complex conjugate in any pathway, only the dipole

amplitude is considered here. The transition dipoles for each of the 36 diagramed pathways are summarized in **Table 3.3**.

Dephasing functions:

Information on the dynamics of this rovibrational system are encoded in the dephasing functions, $F_{abcd}^{(m)}(\tau_3, T_w, \tau_1)$ $(m = 1,2,3,4)$, required to evaluate the pathway-specific response functions using Eq. 3.8. As discussed above, there are 6 general types of pathways that contribute to the 2DIR signal in the rotating wave approximation when the incident pulses are not temporally overlapping (**Figure 3.11**). However, only four unique types of dephasing functions ($m = 1,2,3,4$) are necessary to describe four-wave mixing spectroscopies such as 2DIR.[125] The general expressions for these unique dephasing functions have been given by Sung and Sibley:[125]

$$F_{abcd}^{(1)}(\tau_3, T_w, \tau_1) = \exp\left[-g_{bb}(\tau_3) - g_{cc}(T_w) - g_{dd}(\tau_1) - h_{bc}^{+}(\tau_3, T_w) - h_{cd}^{+}(T_w, \tau_1) - f_{bd}^{+}(\tau_3, \tau_1; T_w)\right]$$

$$F_{abcd}^{(2)}(\tau_3, T_w, \tau_1) = \exp\left[-g_{cc}^{*}(\tau_3) - g_{bb}^{*}(T_w) - g_{dd}(\tau_1 + T_w + \tau_3) - h_{bc}^{+^*}(, \tau_3) + h_{cd}^{-}(\tau_1 + T_w + \tau_3, \tau_3) + f_{bd}^{-^*}(T_w, \tau_1 + T_w + \tau_3; \tau_3)\right] \quad (3.8)$$

$$F_{abcd}^{(3)}(\tau_3, T_w, \tau_1) = \exp\left[-g_{bb}(\tau_3) - g_{cc}^{*}(T_w + \tau_3) - g_{dd}^{*}(\tau_1) - h_{cd}^{+^*}(T_w + \tau_3, \tau_1) - h_{bc}^{-^*}(T_w + \tau_3, \tau_3) + f_{bd}^{+^*}(\tau_3, \tau_1; T_w)\right]$$

$$F_{abcd}^{(4)}(\tau_3, T_w, \tau_1) = \exp\left[-g_{cc}^{*}(\tau_3) - g_{dd}^{*}(\tau_1 + T_w) - g_{bb}(T_w + \tau_3) + h_{bc}^{-^*}(\tau_3, T_w + \tau_3) - h_{cd}^{+^*}(\tau_1 + T_w, \tau_3) + f_{bd}^{-^*}(\tau_1 + T_w; T_w + \tau_3; \tau_3)\right]$$

where,

$$h_{\alpha\beta}^{\pm}(T_w, \tau_1) = \pm[g_{\alpha\beta}(T_w \pm \tau_1) - g_{\alpha\beta}(T_w) - g_{\alpha\beta}(\pm\tau_1)]$$

$f_{\alpha\beta}^{\pm}(T_w, \tau_1; \tau_3) = \pm[g_{\alpha\beta}(\tau_3 + T_w \pm \tau_1) - g_{\alpha\beta}(\tau_3 + T_w) - g_{\alpha\beta}(\tau_3 \pm \tau_1) + g_{\alpha\beta}(\tau_3)]$

In order to evaluate the expressions for these dephasing functions, one requires the lineshape functions, $g_{\alpha\beta}$, which in turn are obtained from the FFCFs, $C_{\alpha,\beta}$, as shown below:

$$g_{\alpha\beta}(t) = \int_0^t d\tau_2 \int_0^{\tau_2} d\tau_1 C_{\alpha,\beta}(\tau_2 - \tau_1) \tag{3.9}$$

FFCFs provide ensemble averaged correlations of the specified transition energy gap fluctuations. The FFCFs relevant for the 2DIR of a quantum rotor report on the energy gap fluctuations between all the optically coupled rovibrational levels. Thus, the FFCFs are written as $C_{n\alpha,n'\beta}(t) = \langle \delta\omega_{n0}^{\alpha}(t)\delta\omega_{n'0}^{\beta}(0)\rangle$, where $\delta\omega_{n0}^{\alpha}(t) = \omega_{n0}^{\alpha}(t) - \langle\omega_{n0}^{\alpha}\rangle$, as described earlier. n and n' are the vibrational quantum numbers of the dipole coupled vibrational levels 0,1, or 2, and α/β denote the type of rotational transitions under consideration. In order to calculate the dephasing functions for the rovibrational system described in this work, 14 different FFCFs are required, in principle. However, these FFCFs can be given in term of only 3 FFCFs: $C_{1R,1R}, C_{1P,1P}$ and $C_{1R,1P}$, when harmonic scaling is assumed.[117] That is, when the vibrational anharmonicity remains unchanged as a result of these energy gap fluctuations, the other 11 FFCFs can be expressed in terms of these 3 FFCFs as shown below:

$$C_{1R,2S}(t) = 2C_{1R,1R}(t)$$

$$C_{1P,20}(t) = 2C_{1P,1P}(t)$$

$$C_{2S,2S}(t) = 4C_{1R,1R}(t)$$

$$
\begin{aligned}
C_{2O,2O}(t) &= 4C_{1P,1P}(t) \\
C_{1R,2Q}(t) &= C_{1R,1R}(t) + C_{1R,1P}(t) \\
C_{1P.2Q}(t) &= C_{1P,1P}(t) + C_{1R,1P}(t) \\
C_{2Q,2Q}(t) &= C_{1R,1R}(t) + C_{1P,1P}(t) + 2C_{1R,1P}(t) \\
C_{1R,0S}(t) &\approx C_{1R,1R}(t) - C_{1P,1P}(t) \\
C_{1P,0O}(t) &\approx C_{1P,1P}(t) + C_{1R,1R}(t) \\
C_{0S,0S}(t) &\approx C_{1R,1R}(t) + C_{1P,1P}(t) - 2C_{1R,1P}(t) \\
C_{0O,0O}(t) &\approx C_{1R,1R}(t) + C_{1P,1P}(t) - 2C_{1R,1P}(t)
\end{aligned}
\tag{3.10}
$$

The FFCFs are assumed to have a form of an exponential decay and the correlation times (τ_c) are taken to be the same for each of these fundamental correlation functions. Therefore the rovibrational FFCFs are written as:

$$
\begin{aligned}
C_{1R,1R}(t) &= \zeta_{1R,1R}(\Delta_{10}^{R})^2 \cdot e^{\frac{t}{\tau_C}} \\
C_{1P,1P}(t) &= \zeta_{1P,1P}(\Delta_{10}^{P})^2 \cdot e^{-\frac{t}{\tau_C}}
\end{aligned}
\tag{3.11}
$$

$$
C_{1R,1P}(t) = \zeta_{1R,1P}(\Delta_{10}^{R} \cdot \Delta_{10}^{P}) \cdot e^{-\frac{t}{\tau_C}}
$$

In Eq S8, $\zeta_{1R,1R} = \zeta_{1P,1P} = 1$ by definition for the autocorrelation functions. The cross-correlation function on the other hand is perfectly anti-correlated, i.e. $\zeta_{1R,1R} = -1$, as shown below.

$$
\begin{aligned}
\delta\omega_{10}^{R}(\delta J) &= \omega_{10}^{R}(J + \delta J) - \omega_{10}^{R}(J) \\
&= \omega_{10} + B_1(J + \delta J + 1)(J + \delta J + 2) - B_0(J + \delta J)(J + \delta J + 1) \\
&\quad -\omega_{10} + B_1(J + 1)(J + 2) - B_0 J(J + 1)
\end{aligned}
$$

$$\cup 2B_1(2J+3)\delta J - 2B_0(2J+1)\delta J$$

$$\cup 4B\delta J \qquad [\text{where } B_0 = B_1 = B]$$

$$\delta\omega_{10}^{P}(\delta J) = \omega_{10}^{P}(J+\delta J) - \omega_{10}^{P}(J)$$

$$= \omega_{10} + B_1(J+\delta J)(J+\delta J-1) - B_0(J+\delta J)(J+\delta J+1)$$

$$-\omega_{10} + B_1 J(J-1) - B_0 J(J+1)$$

$$\cup 2B_1(2J-1)\delta J - 2B_0(2J+1)\delta J$$

$$\cup -4B\delta J$$

$$\therefore \delta\omega_{10}^{R}(\delta J)\delta\omega_{10}^{P}(\delta J) \cup -16B^2(\delta J)^2 < 0$$

Since, fluctuations in $J(\delta J)$ are a consequence of energy gap fluctuation in time (t):

$$\therefore \delta\omega_{10}^{R}(t)\delta\omega_{10}^{P}(0) < 0 \tag{3.12}$$

The corresponding lineshape functions can be calculated in terms of $\Delta_{10}^{P}, \Delta_{10}^{R}$ and τ_c from Eq. 3.13 as:

$$g_{1R,1R}(t) = (\Delta_{10}^{R})^2 \cdot \tau_C^2 \cdot \left[e^{-\frac{t}{\tau_c}} + \frac{t}{\tau_C} - 1\right]$$

$$g_{1P,1P}(t) = (\Delta_{10}^{P})^2 \cdot \tau_C^2 \cdot \left[e^{-\frac{t}{\tau_c}} + \frac{t}{\tau_C} - 1\right] \tag{3.13}$$

$$g_{1R,1P}(t) = (\Delta_{10}^{R} \cdot \Delta_{10}^{P})^2 \cdot \tau_C^2 \cdot \left[e^{-\frac{t}{\tau_c}} + \frac{t}{\tau_C} - 1\right]$$

12 unique dephasing functions are needed to describe the 2DIR spectrum resulting from the 36 rovibrationally specific pathways (**Figure 3.8**), as summarized in **Table 3.4**.

Hard Sphere Collision time determination:

The mean free time for a single N_2O molecule is calculated using a hard sphere model at the given state point density of SF_6 and the mean speed based on a Maxwell-Boltzmann speed distribution for an ideal gas. The collision frequency,ν_{coll}, is given by:

$$\nu_{coll} = N_A \rho_{SF_6} \pi (r_{SF_6} + r_{N_2O})^2 \sqrt{\frac{8RT}{\pi \mu_{N_2O}}} \tag{3.14}$$

Where $N_A$is Avogadro's number; $\rho_{SF_6}$is the density of SF_6; $r_{SF_6}$and r_{N_2O} are the radii of the respective molecules; R is the universal gas constant; T is the experimental temperature and μ_{N_2O} is the reduced mass of the N_2O molecules. The mean free time, τ_{coll}, is given by:

$$\tau_{coll} = \frac{1}{\nu_{coll}} \tag{3.15}$$

The required parameters for calculation of hard sphere collision times for N_2O molecules in SF_6 at the two SF_6 densities studied here are summarized in **Table 3.6**.

3.5 Conclusion

Aside from capturing the 2DIR spectral line shapes for a free rotor, this analysis reveals that the loss of J memory or rotational spectral diffusion due to N_2O-SF_6 interactions is dominated by an exponential decay process with time constants of 9.4 and 6.0 ps at $\rho^* = 0.16$ and 0.30, respectively. Mean free times between N_2O and SF_6 collisions (τ_{coll}) based on hard sphere calculations are correspondingly 7.0 and 3.8 ps at the experimental state points.[130-132] Thus, rotational equilibration ($Z_{rot} = \tau_c/\tau_{coll}$) occurs within 1 to 2 collisions in these moderately dense gas mixtures; $Z_{rot} = 1.4$ ($\rho^* = 0.16$) and

1.6 ($\rho^* = 0.30$) and is therefore a highly efficient process at near ambient temperatures. From low pressure emission, state resolved transient absorption or ultrasonic measurements, Z_{rot} has been previously typically found to be in the range of 1 or 2 for polar molecules, and 4–5 for nonpolar molecules (hydrides excepted). [133-134]Thus, the results of this 2DIR analysis provides quantitative direct time measurements of rotational relaxation that are consistent with these prior low density results. However, the ultrafast nonlinear methodology provides such quantitative relaxation measurements for much higher pressure regimes. These high density 2DIR CLS decays and NMR based determinations of angular momentum correlation times should provide an interesting comparison of these direct and indirect measures of rotational relaxation.[135-136] This 2DIR methodology for quasi-free rotors can be applied to studies of the effects of different types of solvent interactions on rotational relaxation rates, studies of the onset of liquidlike character and dynamics in near critical point regions, as well as reactivity and relaxation in high pressure and high temperature environments.

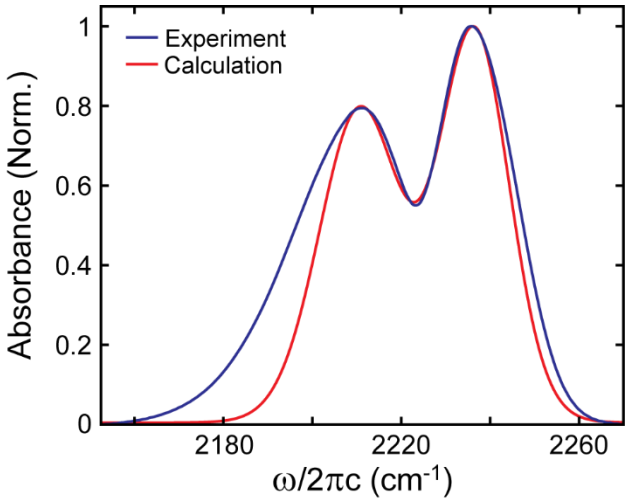

Figure 3.1 - Observed (solid) and modeled (dashed) FTIR spectra of the ν_3 asymmetric stretching fundamental of N2O in $\rho^* = 0.30$ SF_6. P and R branch maxima are at 2211 and 2236 cm^{-1}.

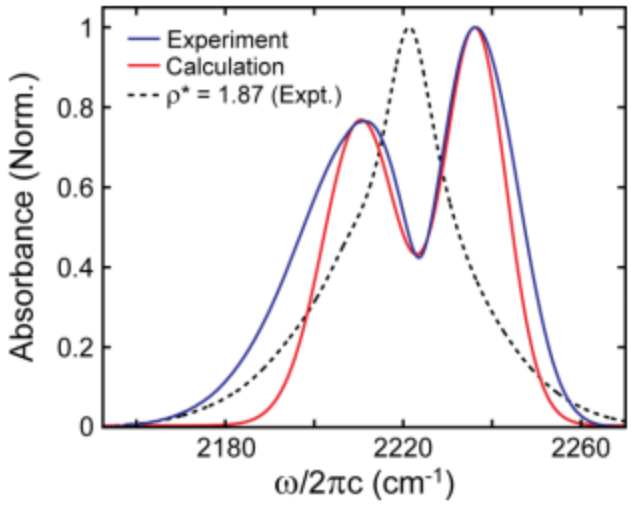

Figure 3.2 - Observed (blue) and calculated (red) FTIR spectrum of the ν_3 antisymmetric stretching fundamental of N_2O in $\rho^* = 0.16$ SF_6 (P = 17 atm, T = 313 K, 4% N_2O). P and R branch maxima are at 2211 and 2236 cm^{-1} , respectively. The calculated absorption spectrum is given by two Kubo lineshape functions centered on the P and R intensity maxima (D_{10}^{R}= 17.7 cm^{-1} , D_{10}^{P} = 21.4 cm^{-1} (FWHM) and τ_C = 9.5 ps). The dashed line is the N_2O ν_3 absorption spectrum in liquid SF_6 and shows how the P and R structure disappears in this condensed state.

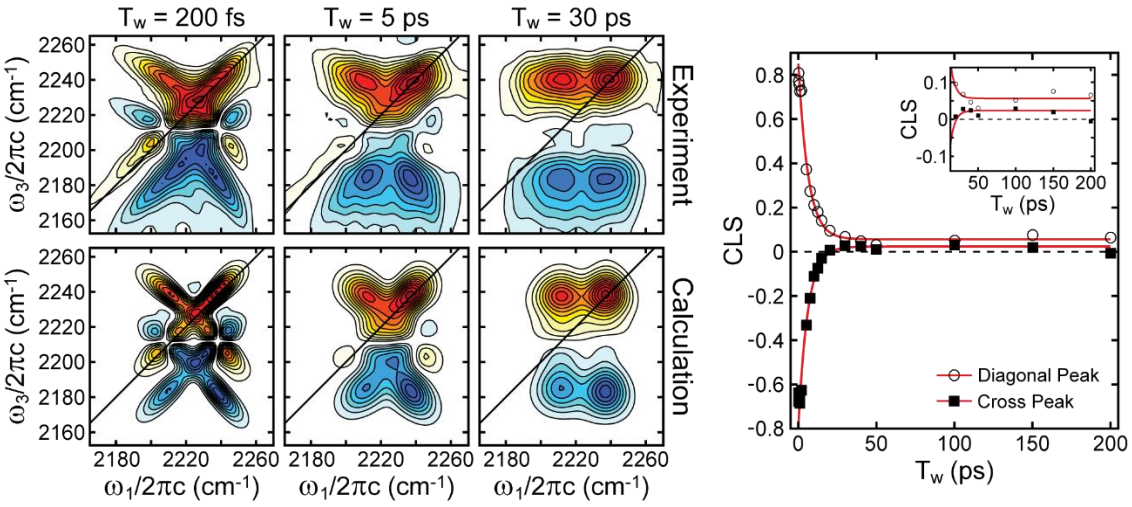

Figure 3.3 - Experimental and calculated 2DIR spectra of the N_2O ν_3 fundamental in $\rho^* = 0.30$ SF_6 for waiting times (T_w) of 0.2, 5, and 30 ps. Frequency-frequency correlation functions determined by CLS decay for the bleach diagonal (open circle) and antidiagonal (filled square) 2DIR features and best fits to an exponential decay and a small constant offset are shown (red). The dominant decay times are 6.1 ± 0.3 ps (diagonal) and 5.8 ± 0.4 ps (antidiagonal).

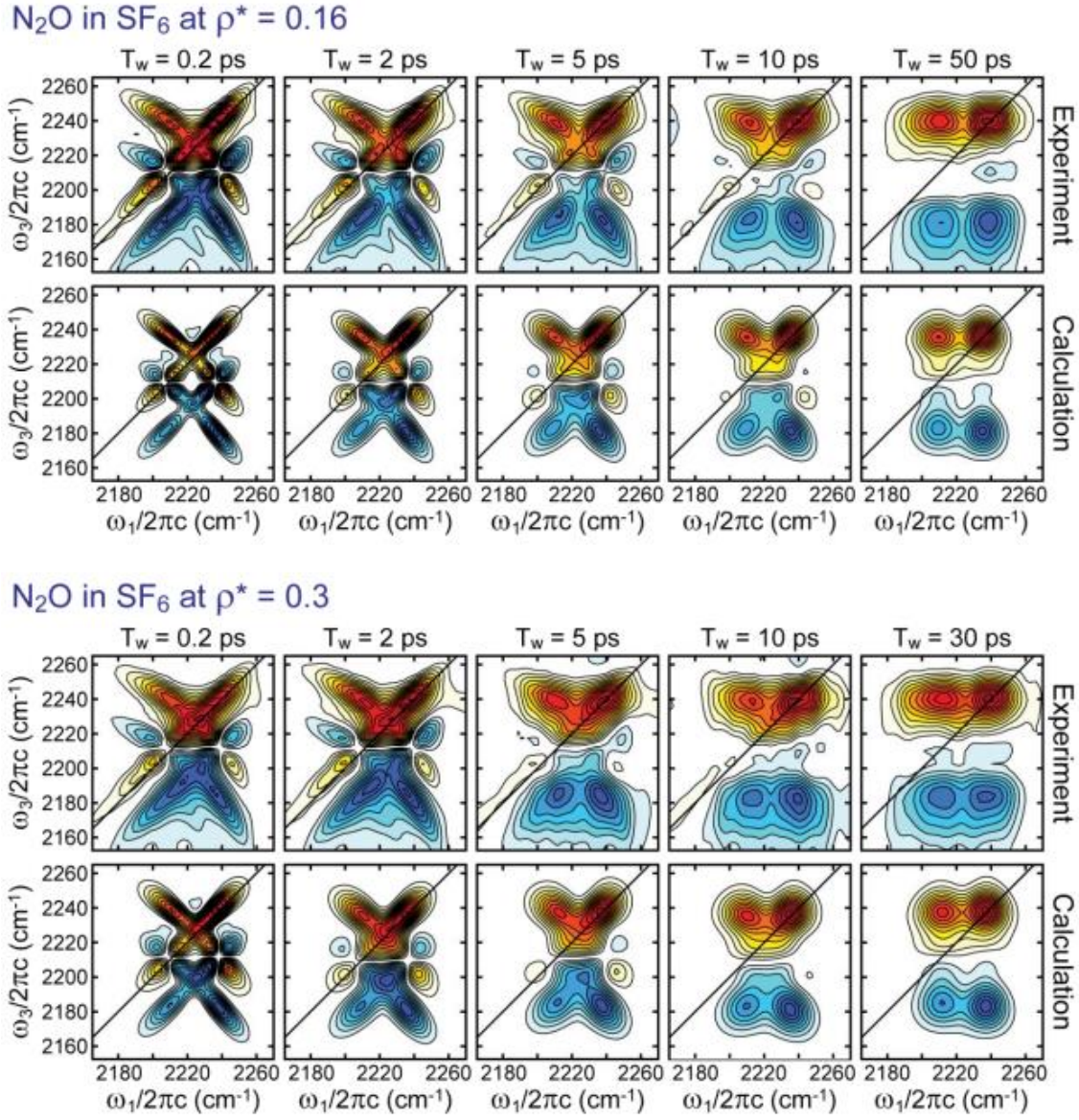

Figure 3.4 - Experimental and calculated 2DIR spectra of the ν_3 antisymmetric stretching fundamental of N_2O in SF_6 $\rho^* = 0.16$ and $\rho^* = 0.3$ as a function of waiting times (T_w).

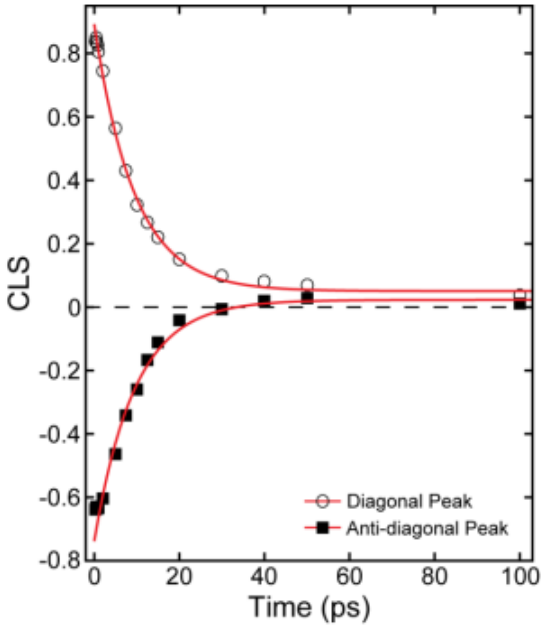

Figure 3.5 - Frequency-frequency correlation functions (FFCF) are determined by CLS decay for the bleach diagonal (o) and anti-diagonal (ν) 2DIR spectral features. The best fits to an exponential decay and a small constant offset are shown in red. The dominant decay times are 9.4 ± 0.3 ps (diagonal) and 9.5 ± 0.6 ps (anti-diagonal).

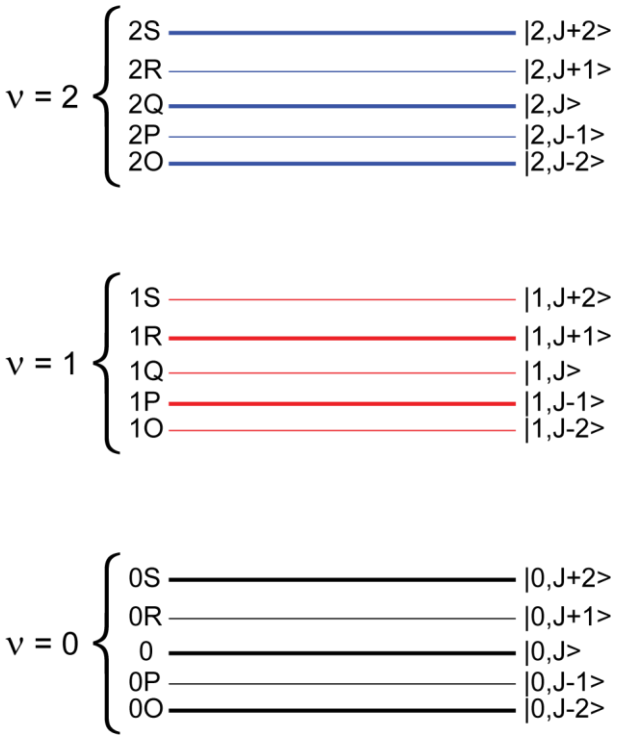

Figure 3.6 - Rovibrational energy levels relevant for the description of the 2DIR spectroscopy of a quantum free rotor. The bold lines indicate the eight dipole-coupled rovibrational levels, resulting from the $\Delta J = \pm 1$ selection rule for each $\Delta\nu = \pm 1$ dipole interaction, that contribute to the signal in this third-order nonlinear experiment originating from the $|0, J>$ level

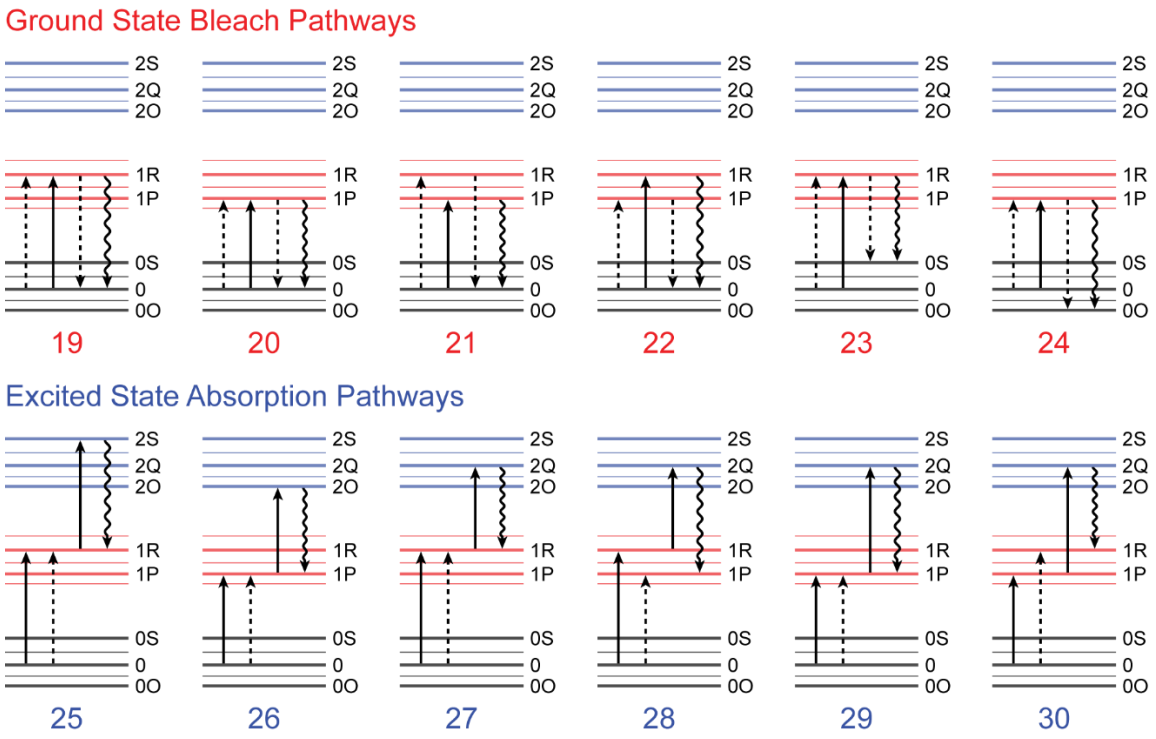

Figure 3.7 - Twelve (six GSB-SE and six ESA) of the thirty-six density matrix pathways contributing to the 2DIR signal originating in the $\nu = |0, J\rangle$ rovibrational level are highlighted.

Pathway I

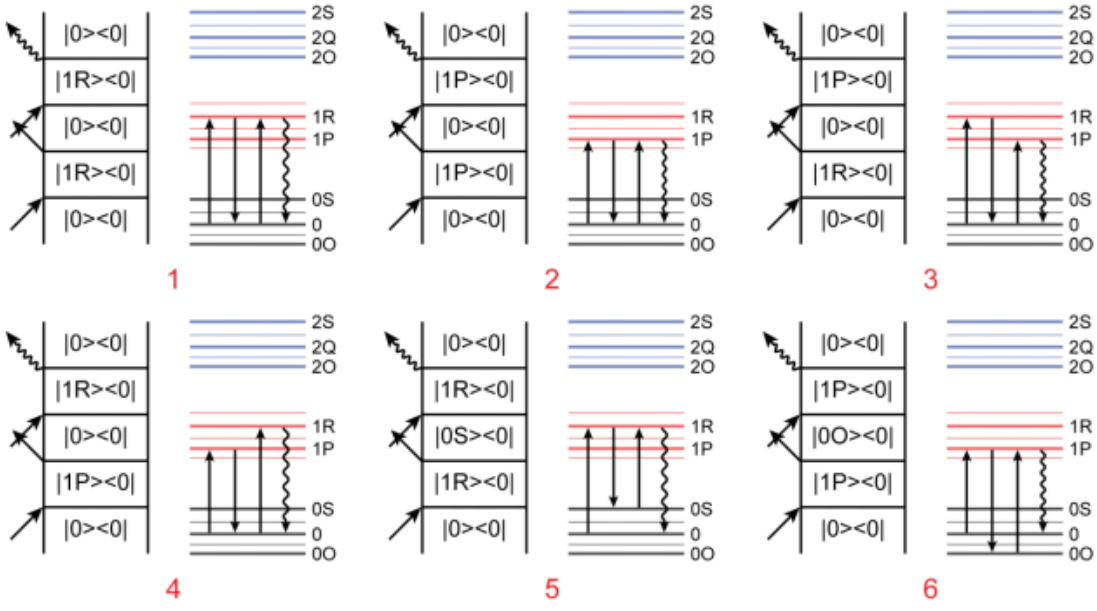

Pathway II

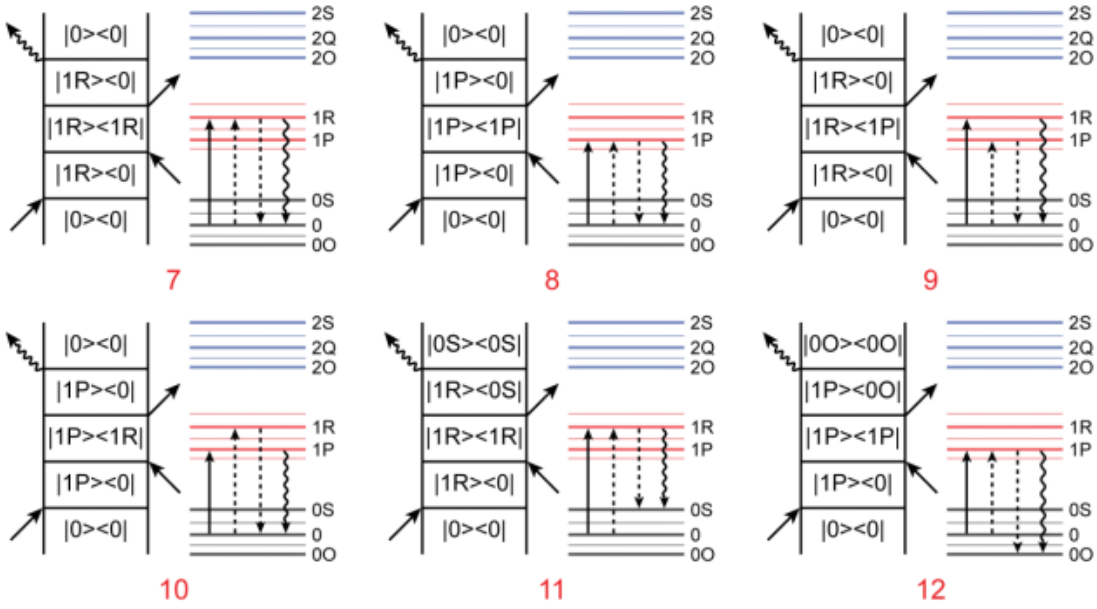

Pathway III

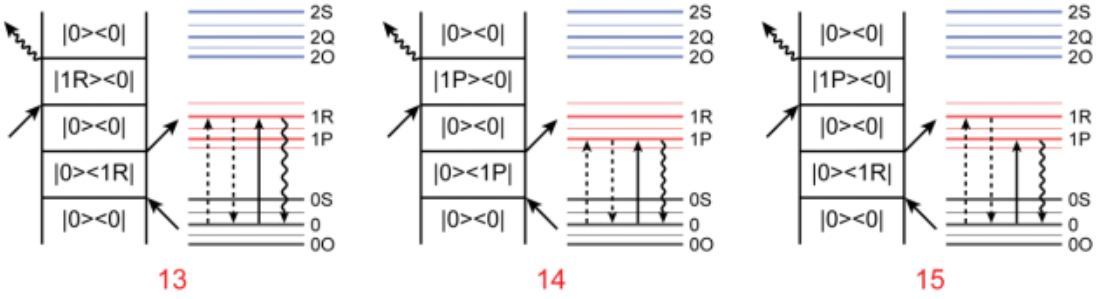

Pathway IV

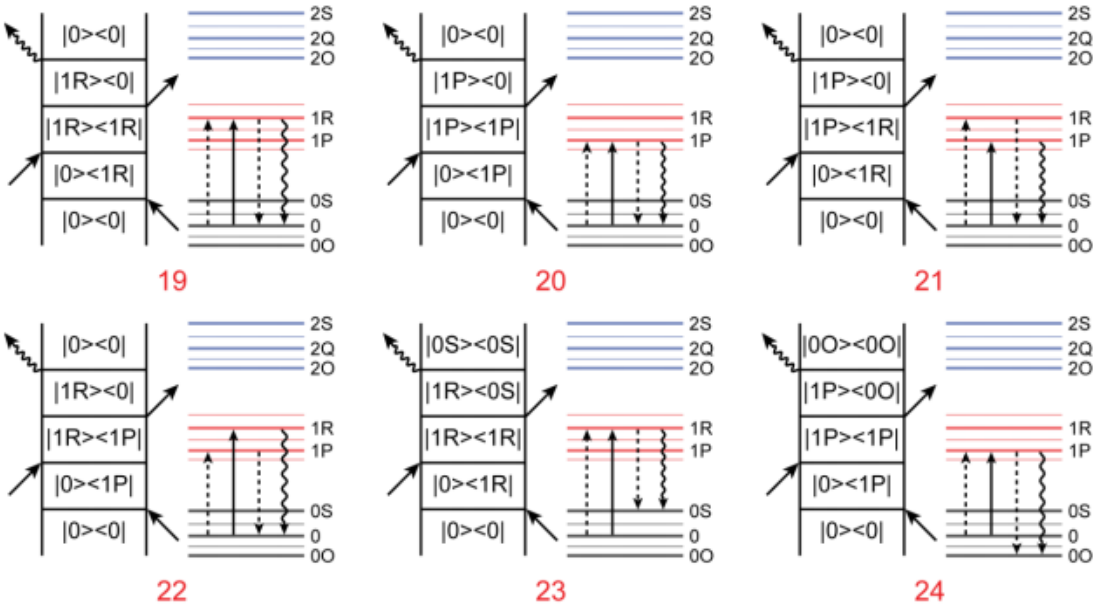

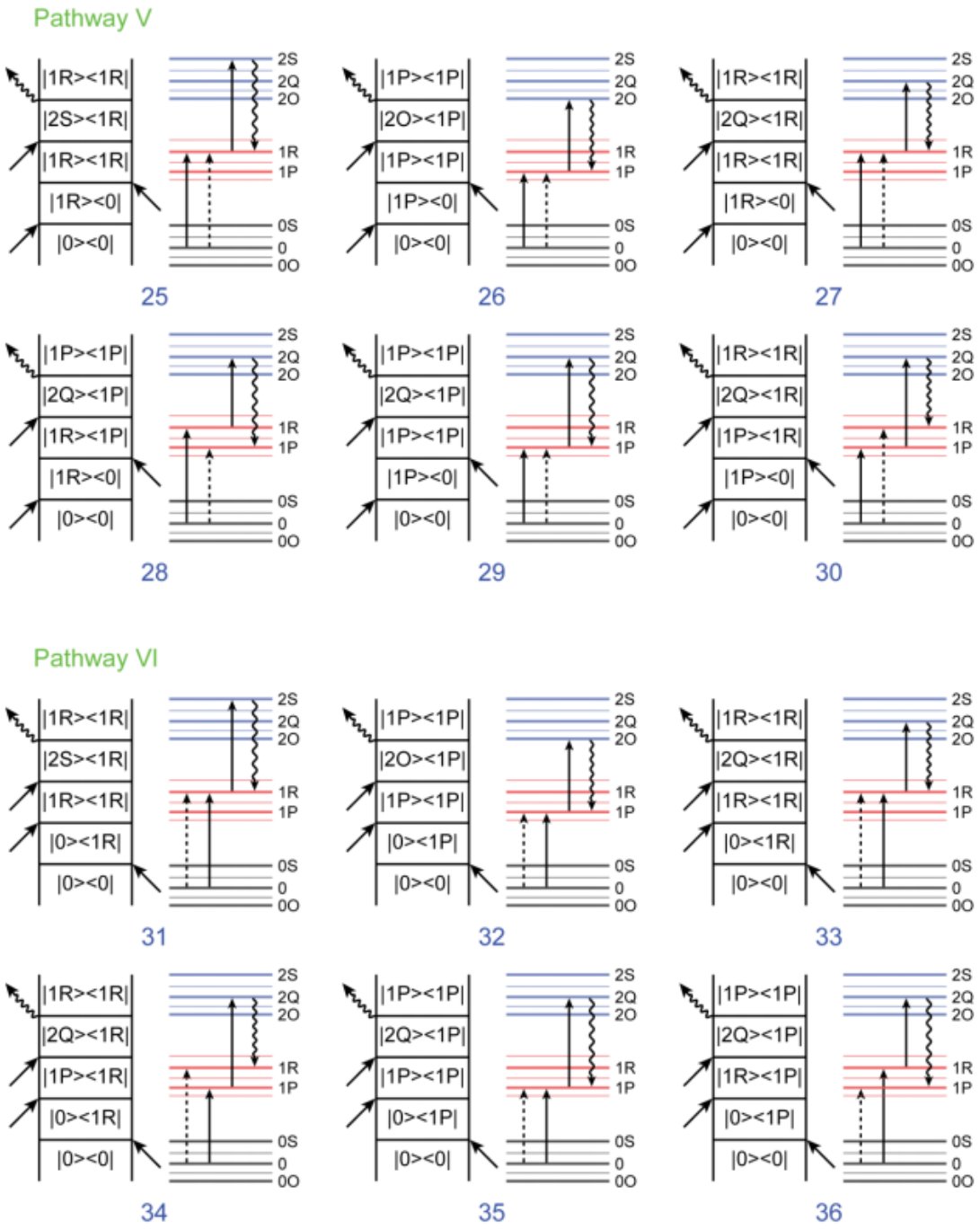

Figure 3.8 - 36 rovibrationally-specific Liouville pathways that contribute to the total third-order response originating from $|0,J\rangle$ rovibrational level and accounts for the 2DIR spectrum of a (quasi) free rotor.

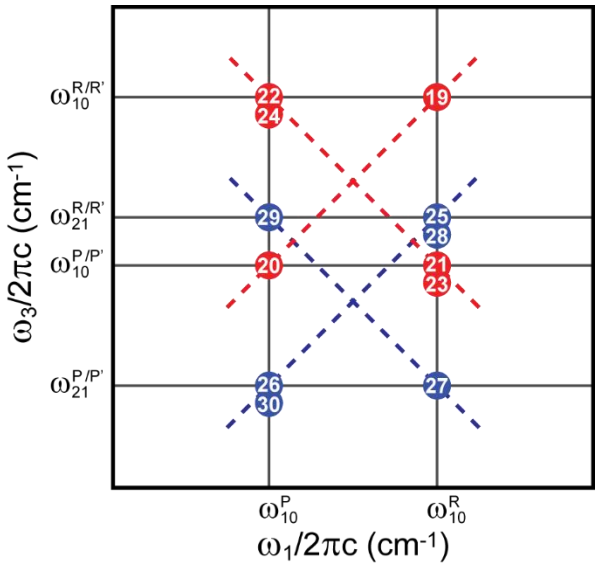

Figure 3.9 - 2DIR map that indicates where signal polarization is generated by the 12 density matrix pathways in figure 3.3 as a function of (ω_1, ω_3).

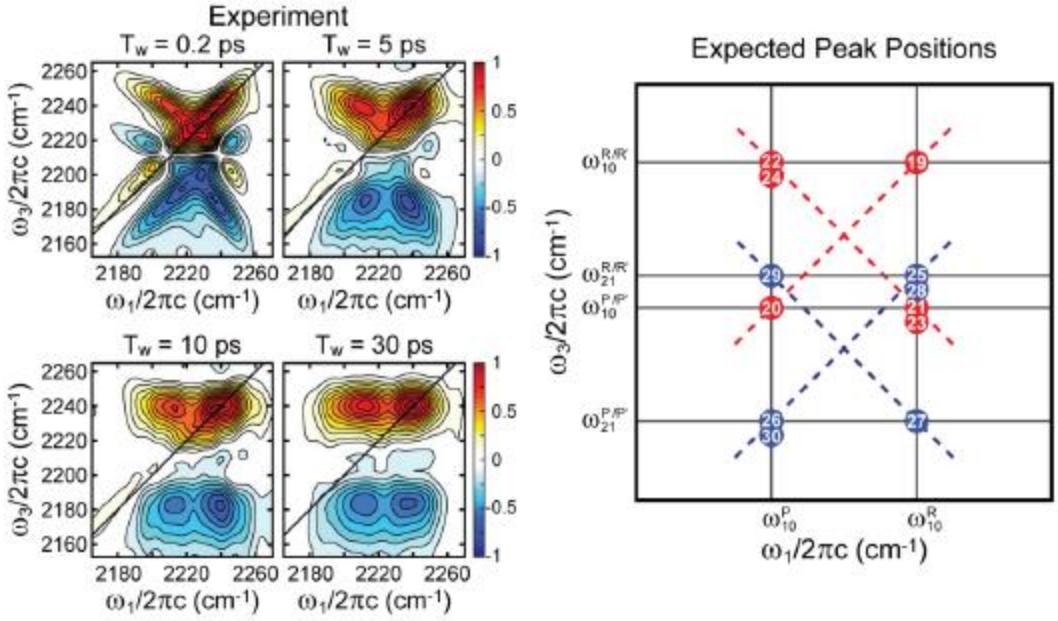

Figure 3.10 - Comparison of experimental and theoretical peak positions in 2DIR spectra of N_2O in SF_6 ($\rho^* = 0.3$). In the experimental spectra at early T_w, 4 distinct GSB-SE features are observed from Liouville pathways 19, 20, (21 and 23) and (22 and 24). Alongside, 4 distinct ESA features are also observed at early T_w from Liouville pathways (25 and 28), (26 and 30), 27 and 29. The GSB-SE features from (21 and 23) and 20 overlaps with ESA features due to (25 and 28) and 29, respectively, resulting an "X" pattern in the experimental spectra. At longer T_w, these two GSB-SE features almost cancel the two overlapping ESA features. As a result, only 4 distinct spectral features are observed at longer T_w, 2 GSB-SE and 2 ESA.

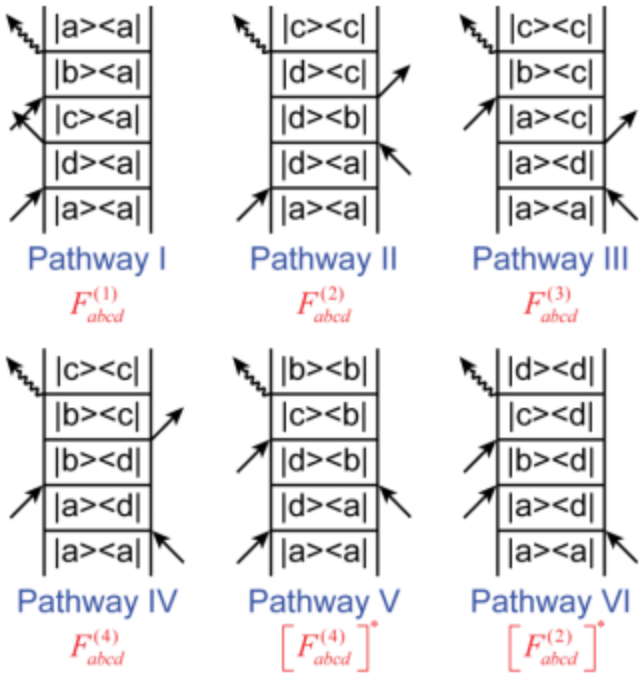

Figure 3.11 - 6 general types of Liouville pathways contributing to the 2DIR signal for a free rotor. Here, $|a\rangle = |0, J\rangle$ and $|b\rangle, |c\rangle$ and $|d\rangle$ are the possible dipole-coupled rovibrational levels allowed by the dipole selection rules of $\Delta v = \pm 1$ and $\Delta J = \pm 1$, and summarized in Fig. 3.6.

Table 3.1: Summary of 2DIR experimental results and calculation parameters for the N_2O ν_3 mode in SF_6 at two densities.

SF_6 Density	$\Delta_{10}^{R}(cm^{-1})$	$\Delta_{10}^{P}(cm^{-1})$	$\tau_c(ps)$	$T_1(ps)^x$	Z_{rot}
$\rho^* = 0.16$	17.7	21.4	6.4	102	1.3
$\rho^* = 0.30$	19.3	22.4	9.4	35	1.6

[x]Fastest component of biexponential lifetime decay

Table 3.2: List of transition frequencies for each of the 36 pathways shown in Figure 3.8.

Pathway No.	ω_1	ω_2	ω_3	Pathway No.	ω_1	ω_2	ω_3
1	ω_{10}^{R}	0	ω_{10}^{R}	19	$-\omega_{10}^{R}$	0	ω_{10}^{R}
2	ω_{10}^{P}	0	ω_{10}^{P}	20	$-\omega_{10}^{P}$	0	ω_{10}^{P}
3	ω_{10}^{R}	0	ω_{10}^{P}	21	$-\omega_{10}^{R}$	$-2B_1(2J+1)$	ω_{10}^{P}
4	ω_{10}^{P}	0	ω_{10}^{R}	22	$-\omega_{10}^{P}$	$2B_1(2J+1)$	ω_{10}^{R}
5	ω_{10}^{R}	$2B_0(2J+3)$	ω_{10}^{R}	23	$-\omega_{10}^{R}$	0	$\omega_{10}^{P'}$
6	ω_{10}^{P}	$-2B_0(2J-1)$	ω_{10}^{P}	24	$-\omega_{10}^{P}$	0	$\omega_{10}^{R'}$
7	ω_{10}^{R}	0	ω_{10}^{R}	25	ω_{10}^{R}	0	ω_{21}^{R}
8	ω_{10}^{P}	0	ω_{10}^{P}	26	ω_{10}^{P}	0	ω_{21}^{P}
9	ω_{10}^{R}	$2B_1(2J+1)$	ω_{10}^{R}	27	ω_{10}^{R}	0	$\omega_{21}^{P'}$
10	ω_{10}^{P}	$-2B_1(2J+1)$	ω_{10}^{P}	28	ω_{10}^{R}	$2B_1(2J+1)$	$\omega_{21}^{R'}$
11	ω_{10}^{R}	0	$\omega_{10}^{P'}$	29	ω_{10}^{P}	0	$\omega_{21}^{R'}$
12	ω_{10}^{P}	0	$\omega_{10}^{R'}$	30	ω_{10}^{P}	$-2B_1(2J+1)$	$\omega_{21}^{P'}$
13	$-\omega_{10}^{R}$	0	ω_{10}^{R}	31	$-\omega_{10}^{R}$	0	ω_{21}^{R}
14	$-\omega_{10}^{P}$	0	ω_{10}^{P}	32	$-\omega_{10}^{P}$	0	ω_{21}^{P}
15	$-\omega_{10}^{R}$	0	ω_{10}^{P}	33	$-\omega_{10}^{R}$	0	$\omega_{21}^{P'}$
16	$-\omega_{10}^{P}$	0	ω_{10}^{R}	34	$-\omega_{10}^{R}$	$-2B_1(2J+1)$	$\omega_{21}^{P'}$
17	$-\omega_{10}^{R}$	$-2B_0(2J+3)$	$\omega_{10}^{P'}$	35	$-\omega_{10}^{P}$	0	$\omega_{21}^{R'}$
18	$-\omega_{10}^{P}$	$2B_0(2J-1)$	$\omega_{10}^{R'}$	36	$-\omega_{10}^{P}$	$2B_1(2J+1)$	$\omega_{21}^{R'}$

Table 3.3: List of transition dipoles for each of the 36 pathways shown in Figure 3.8.

Pathway No.	$\lvert\mu_1\rvert$	$\lvert\mu_2\rvert$	$\lvert\mu_3\rvert$	$\lvert\mu_4\rvert$
1	$\mu_{10}\sqrt{J+1}$	$\mu_{10}\sqrt{J+1}$	$\mu_{10}\sqrt{J+1}$	$\mu_{10}\sqrt{J+1}$
2	$\mu_{10}\sqrt{J}$	$\mu_{10}\sqrt{J}$	$\mu_{10}\sqrt{J}$	$\mu_{10}\sqrt{J}$
3	$\mu_{10}\sqrt{J+1}$	$\mu_{10}\sqrt{J+1}$	$\mu_{10}\sqrt{J}$	$\mu_{10}\sqrt{J}$
4	$\mu_{10}\sqrt{J}$	$\mu_{10}\sqrt{J}$	$\mu_{10}\sqrt{J+1}$	$\mu_{10}\sqrt{J+1}$
5	$\mu_{10}\sqrt{J+1}$	$\mu_{10}\sqrt{J+2}$	$\mu_{10}\sqrt{J+2}$	$\mu_{10}\sqrt{J+1}$
6	$\mu_{10}\sqrt{J}$	$\mu_{10}\sqrt{J-1}$	$\mu_{10}\sqrt{J-1}$	$\mu_{10}\sqrt{J}$
7	$\mu_{10}\sqrt{J+1}$	$\mu_{10}\sqrt{J+1}$	$\mu_{10}\sqrt{J+1}$	$\mu_{10}\sqrt{J+1}$
8	$\mu_{10}\sqrt{J}$	$\mu_{10}\sqrt{J}$	$\mu_{10}\sqrt{J}$	$\mu_{10}\sqrt{J}$
9	$\mu_{10}\sqrt{J+1}$	$\mu_{10}\sqrt{J}$	$\mu_{10}\sqrt{J}$	$\mu_{10}\sqrt{J+1}$
10	$\mu_{10}\sqrt{J}$	$\mu_{10}\sqrt{J+1}$	$\mu_{10}\sqrt{J+1}$	$\mu_{10}\sqrt{J}$
11	$\mu_{10}\sqrt{J+1}$	$\mu_{10}\sqrt{J+1}$	$\mu_{10}\sqrt{J+2}$	$\mu_{10}\sqrt{J+2}$
12	$\mu_{10}\sqrt{J}$	$\mu_{10}\sqrt{J}$	$\mu_{10}\sqrt{J-1}$	$\mu_{10}\sqrt{J-1}$
13	$\mu_{10}\sqrt{J+1}$	$\mu_{10}\sqrt{J+1}$	$\mu_{10}\sqrt{J+1}$	$\mu_{10}\sqrt{J+1}$
14	$\mu_{10}\sqrt{J}$	$\mu_{10}\sqrt{J}$	$\mu_{10}\sqrt{J}$	$\mu_{10}\sqrt{J}$
15	$\mu_{10}\sqrt{J+1}$	$\mu_{10}\sqrt{J+1}$	$\mu_{10}\sqrt{J}$	$\mu_{10}\sqrt{J}$
16	$\mu_{10}\sqrt{J}$	$\mu_{10}\sqrt{J}$	$\mu_{10}\sqrt{J+1}$	$\mu_{10}\sqrt{J+1}$
17	$\mu_{10}\sqrt{J+1}$	$\mu_{10}\sqrt{J+2}$	$\mu_{10}\sqrt{J+1}$	$\mu_{10}\sqrt{J+2}$
18	$\mu_{10}\sqrt{J}$	$\mu_{10}\sqrt{J-1}$	$\mu_{10}\sqrt{J}$	$\mu_{10}\sqrt{J-1}$

Pathway No.	$\lvert\mu_1\rvert$	$\lvert\mu_2\rvert$	$\lvert\mu_3\rvert$	$\lvert\mu_4\rvert$
19	$\mu_{10}\sqrt{J+1}$	$\mu_{10}\sqrt{J+1}$	$\mu_{10}\sqrt{J+1}$	$\mu_{10}\sqrt{J+1}$
20	$\mu_{10}\sqrt{J}$	$\mu_{10}\sqrt{J}$	$\mu_{10}\sqrt{J}$	$\mu_{10}\sqrt{J}$
21	$\mu_{10}\sqrt{J+1}$	$\mu_{10}\sqrt{J}$	$\mu_{10}\sqrt{J+1}$	$\mu_{10}\sqrt{J}$
22	$\mu_{10}\sqrt{J}$	$\mu_{10}\sqrt{J+1}$	$\mu_{10}\sqrt{J}$	$\mu_{10}\sqrt{J+1}$
23	$\mu_{10}\sqrt{J+1}$	$\mu_{10}\sqrt{J+1}$	$\mu_{10}\sqrt{J+2}$	$\mu_{10}\sqrt{J+2}$
24	$\mu_{10}\sqrt{J}$	$\mu_{10}\sqrt{J}$	$\mu_{10}\sqrt{J-1}$	$\mu_{10}\sqrt{J-1}$
25	$\mu_{10}\sqrt{J+1}$	$\mu_{10}\sqrt{J+1}$	$\mu_{21}\sqrt{J+2}$	$\mu_{21}\sqrt{J+2}$
26	$\mu_{10}\sqrt{J}$	$\mu_{10}\sqrt{J}$	$\mu_{21}\sqrt{J-1}$	$\mu_{21}\sqrt{J-1}$
27	$\mu_{10}\sqrt{J+1}$	$\mu_{10}\sqrt{J+1}$	$\mu_{21}\sqrt{J+1}$	$\mu_{21}\sqrt{J+1}$
28	$\mu_{10}\sqrt{J+1}$	$\mu_{10}\sqrt{J}$	$\mu_{21}\sqrt{J+1}$	$\mu_{21}\sqrt{J}$
29	$\mu_{10}\sqrt{J}$	$\mu_{10}\sqrt{J}$	$\mu_{21}\sqrt{J}$	$\mu_{21}\sqrt{J}$
30	$\mu_{10}\sqrt{J}$	$\mu_{10}\sqrt{J+1}$	$\mu_{21}\sqrt{J}$	$\mu_{21}\sqrt{J+1}$
31	$\mu_{10}\sqrt{J+1}$	$\mu_{10}\sqrt{J+1}$	$\mu_{21}\sqrt{J+2}$	$\mu_{21}\sqrt{J+2}$
32	$\mu_{10}\sqrt{J}$	$\mu_{10}\sqrt{J}$	$\mu_{21}\sqrt{J-1}$	$\mu_{21}\sqrt{J-1}$
33	$\mu_{10}\sqrt{J+1}$	$\mu_{10}\sqrt{J+1}$	$\mu_{21}\sqrt{J+1}$	$\mu_{21}\sqrt{J+1}$
34	$\mu_{10}\sqrt{J+1}$	$\mu_{10}\sqrt{J}$	$\mu_{21}\sqrt{J}$	$\mu_{21}\sqrt{J+1}$
35	$\mu_{10}\sqrt{J}$	$\mu_{10}\sqrt{J}$	$\mu_{21}\sqrt{J}$	$\mu_{21}\sqrt{J}$
36	$\mu_{10}\sqrt{J}$	$\mu_{10}\sqrt{J+1}$	$\mu_{21}\sqrt{J+1}$	$\mu_{21}\sqrt{J}$

Table 3.4: List of unique dephasing functions.

Dephasing Functions	Pathway No.
$F^{(1)}_{0,1R,0,1R}(\tau_3,T_w,\tau_1) = F^{(2)}_{0,1R,0,1R}(\tau_3,T_w,\tau_1) = \left[F^{(4)}_{0,1R,2S,1R}(\tau_3,T_w,\tau_1)\right]^*$ $= \exp[-g_{1R,1R}(\tau_1) - g_{1R,1R}(T_w) - g_{1R,1R}(\tau_3) + g_{1R,1R}(\tau_1+T_w)$ $+g_{1R,1R}(T_w+\tau_3) - g_{1R,1R}(\tau_1+T_w+\tau_3)]$	1 = 7 = 25
$F^{(1)}_{0,1P,0,1P}(\tau_3,T_w,\tau_1) = F^{(2)}_{0,1P,0,1P}(\tau_3,T_w,\tau_1) = \left[F^{(4)}_{0,1P,2O,1P}(\tau_3,T_w,\tau_1)\right]^*$ $= \exp[-g_{1P,1P}(\tau_1) - g_{1P,1P}(T_w) - g_{1P,1P}(\tau_3) + g_{1P,1P}(\tau_1+T_w)$ $+g_{1P,1P}(T_w+\tau_3) - g_{1P,1P}(\tau_1+T_w+\tau_3)]$	2 = 8 = 26
$F^{(1)}_{0,1P,0,1R}(\tau_3,T_w,\tau_1) = F^{(2)}_{0,1R,0S,1R}(\tau_3,T_w,\tau_1) = \left[F^{(4)}_{0,1R,2Q,1R}(\tau_3,T_w,\tau_1)\right]^*$ $= \exp[-g_{1R,1R}(\tau_1) - g_{1R,1P}(T_w) - g_{1P,1P}(\tau_3) + g_{1R,1P}(\tau_1+T_w)$ $+g_{1R,1P}(T_w+\tau_3) - g_{1R,1P}(\tau_1+T_w+\tau_3)]$	3 = 11 = 27
$F^{(1)}_{0,1R,0,1P}(\tau_3,T_w,\tau_1) = F^{(2)}_{0,1P,0O,1P}(\tau_3,T_w,\tau_1) = \left[F^{(4)}_{0,1P,2Q,1P}(\tau_3,T_w,\tau_1)\right]^*$ $= \exp[-g_{1P,1P}(\tau_1) - g_{1R,1P}(T_w) - g_{1R,1R}(\tau_3) + g_{1R,1P}(\tau_1+T_w)$ $+g_{1R,1P}(T_w+\tau_3) - g_{1R,1P}(\tau_1+T_w+\tau_3)]$	4 = 12 = 29
$F^{(1)}_{0,1R,0S,1R}(\tau_3,T_w,\tau_1) = F^{(2)}_{0,1P,0,1R}(\tau_3,T_w,\tau_1) = \left[F^{(4)}_{0,1P,2Q,1R}(\tau_3,T_w,\tau_1)\right]^*$ $= \exp[-g_{1R,1P}(\tau_1) - g_{1P,1P}(T_w) - g_{1R,1P}(\tau_3) + g_{1R,1P}(\tau_1+T_w)$ $+g_{1R,1P}(T_w+\tau_3) - g_{1R,1R}(\tau_1+T_w+\tau_3)]$	5 = 9 = 28
$F^{(1)}_{0,1P,0O,1P}(\tau_3,T_w,\tau_1) = F^{(2)}_{0,1R,0,1P}(\tau_3,T_w,\tau_1) = \left[F^{(4)}_{0,1R,2Q,1P}(\tau_3,T_w,\tau_1)\right]^*$ $= \exp[-g_{1R,1P}(\tau_1) - g_{1R,1R}(T_w) - g_{1R,1P}(\tau_3) + g_{1R,1P}(\tau_1+T_w)$ $+g_{1R,1P}(T_w+\tau_3) - g_{1P,1P}(\tau_1+T_w+\tau_3)]$	6 = 10 = 30
$F^{(3)}_{0,1R,0,1R}(\tau_3,T_w,\tau_1) = F^{(4)}_{0,1R,0,1R}(\tau_3,T_w,\tau_1) = \left[F^{(2)}_{0,1R,2S,1R}(\tau_3,T_w,\tau_1)\right]^*$ $= \exp[-g_{1R,1R}(\tau_1) + g_{1R,1R}(T_w) - g_{1R,1R}(\tau_3) - g_{1R,1R}(\tau_1+T_w)$ $-g_{1R,1R}(T_w+\tau_3) + g_{1R,1R}(\tau_1+T_w+\tau_3)]$	13 = 19 = 31
$F^{(3)}_{0,1P,0,1P}(\tau_3,T_w,\tau_1) = F^{(4)}_{0,1P,0,1P}(\tau_3,T_w,\tau_1) = \left[F^{(2)}_{0,1P,2O,1P}(\tau_3,T_w,\tau_1)\right]^*$ $= \exp[-g_{1P,1P}(\tau_1) + g_{1P,1P}(T_w) - g_{1P,1P}(\tau_3) - g_{1P,1P}(\tau_1+T_w)$ $-g_{1P,1P}(T_w+\tau_3) + g_{1P,1P}(\tau_1+T_w+\tau_3)]$	14 = 20 = 32

Dephasing Functions	Pathway No.
$F^{(3)}_{0,1P,0,1R}(\tau_3,T_w,\tau_1) = F^{(4)}_{0,1R,0S,1R}(\tau_3,T_w,\tau_1) = \left[F^{(2)}_{0,1R,2Q,1R}(\tau_3,T_w,\tau_1)\right]^*$ $= \exp[-g_{1R,1R}(\tau_1) + g_{1R,1P}(T_w) - g_{1P,1P}(\tau_3) - g_{1R,1P}(\tau_1+T_w)$ $-g_{1R,1P}(T_w+\tau_3) + g_{1R,1P}(\tau_1+T_w+\tau_3)]$	15 = 23 = 33
$F^{(3)}_{0,1R,0,1P}(\tau_3,T_w,\tau_1) = F^{(4)}_{0,1P,0O,1P}(\tau_3,T_w,\tau_1) = \left[F^{(2)}_{0,1P,2Q,1P}(\tau_3,T_w,\tau_1)\right]^*$ $= \exp[-g_{1P,1P}(\tau_1) + g_{1R,1P}(T_w) - g_{1R,1R}(\tau_3) - g_{1R,1P}(\tau_1+T_w)$ $-g_{1R,1P}(T_w+\tau_3) + g_{1R,1P}(\tau_1+T_w+\tau_3)]$	16 = 24 = 35
$F^{(3)}_{0,1R,0S,1R}(\tau_3,T_w,\tau_1) = F^{(4)}_{0,1P,0,1R}(\tau_3,T_w,\tau_1) = \left[F^{(2)}_{0,1P,2Q,1R}(\tau_3,T_w,\tau_1)\right]^*$ $= \exp[-g_{1R,1P}(\tau_1) + g_{1R,1P}(T_w) - g_{1R,1P}(\tau_3) - g_{1R,1R}(\tau_1+T_w)$ $-g_{1P,1P}(T_w+\tau_3) + g_{1R,1P}(\tau_1+T_w+\tau_3)]$	17 = 21 = 34
$F^{(3)}_{0,1P,0O,1P}(\tau_3,T_w,\tau_1) = F^{(4)}_{0,1R,0,1P}(\tau_3,T_w,\tau_1) = \left[F^{(2)}_{0,1R,2Q,1P}(\tau_3,T_w,\tau_1)\right]^*$ $= \exp[-g_{1R,1P}(\tau_1) + g_{1R,1P}(T_w) - g_{1R,1P}(\tau_3) - g_{1P,1P}(\tau_1+T_w)$ $-g_{1R,1R}(T_w+\tau_3) + g_{1R,1P}(\tau_1+T_w+\tau_3)]$	18 = 22 = 36

Table 3.5: Numerical values of parameters used in calculations in this chapter.

Parameter	Value
J	15
B_0	0.419 cm^{-1}
B_1	0.4156 cm^{-1}
B_2	0.4122 cm^{-1}
ω_{10}	2223. 5 cm^{-1}

Table 3.6: Parameters used in the calculation of the hard sphere collision times for N_2O in SF_6.

Parameter	Value
$\boldsymbol{\rho_{SF_6}}$ ($\boldsymbol{\rho}^* = 0.16$)[130]	821.31 $mol \cdot m^{-3}$
$\boldsymbol{\rho_{SF_6}}$ ($\boldsymbol{\rho}^* = 0.30$)[130]	1506.3 $mol \cdot m^{-3}$
$\boldsymbol{r_{SF_6}}$Error! Bookmark not defined.**128**[131]	2.326 x 10^{-10} m
$\boldsymbol{r_{N_2O}}$[132]	1.94 x 10^{-10} m
$\boldsymbol{N_A}$	6.022 x 10^{23}
$\boldsymbol{R}$	8.3145 $J \cdot mol^{-1} \cdot K^{-1}$
$\boldsymbol{T}$	303.15 K
$\boldsymbol{\mu}$ (reduced mass)	0.03382 $kg \cdot mol^{-1}$

Chapter 4: Two-dimensional infrared spectroscopy from the gas to liquid phase: Density dependent *J*-scrambling, vibrational relaxation, and the onset of liquid character

4.1 Introduction

Vibrational spectroscopic lineshapes in solutions encode a wealth of information about intermolecular interactions, energy relaxation rates, and the structure and dynamics of the surrounding solvent at a given state point. As a molecule's environment changes from that of a dilute gas to one whose density is characteristic of a liquid, rovibrational spectral shapes correspondingly evolve and thus report on these fundamental properties as a function of temperature, pressure and density. At low densities, where the solution is in the gas phase, vibrational spectra are characterized by discrete resolvable *P(J)* (ΔJ = -1) and *R(J)* (ΔJ = +1) rotational transitions and, when symmetry allowed, a *Q*-branch (ΔJ = 0).[137] Due to the spectral resolution, such systems can readily provide information about intermolecular collisions, the shapes of interaction potentials, coherent quantum dynamics and quantum specific energy decay. However, as the surrounding fluid's density increases, collisional broadening obscures the resolved discrete *J* rovibrational absorption features and *v, J* quantum specific information, such as the distinct timescales of rotational and vibrational relaxation, are not readily evident spectroscopically. As the fluid's density increases further and approaches liquid-like densities only vestigial evidence, at best, of the diffuse rotational branches can be detected in the IR spectrum and the nature of the lineshape becomes increasingly dependent on theoretical

modeling.[138] At even higher densities, including state points in the supercritical region, bandshapes begin to narrow resembling their absorption spectral bandshapes in liquid solution. It is unclear if these nearly featureless spectra are due to quasi-free rotors, hindered rotational or librational transitions, or some dynamic combination of these. Experimental characterization of these fluid solutions, correspondingly as gas, liquid or a dynamic inhomogeneous mix, is thus limited.

The use of ultrafast 2DIR spectroscopy[139] to learn about rotational and vibrational relaxation in dense fluids, special solvation effects in the supercritical fluid (SCF) phase, and the evolution of liquid phase character, as a function of fluid density is reported here. Much of what is known about gas phase reaction dynamics has come from state-to-state, time-resolved spectroscopic measurements necessarily in relatively low density systems where discrete rotational spectroscopic features are resolvable.[140] However, dense fluids, particularly at high temperatures and pressures, are solvent environments important to many chemical processes. For example, internal combustion engines operate under high pressures, in the 5-100 atm range, and often in the supercritical regime.[141] Given the lack of spectral resolution largely due to quasi-elastic and inelastic collisional effects in such high density/pressure fluids, echo-like spectroscopic techniques, such as 2DIR, are uniquely suited to uncover dynamical information on how excited molecules in these dense environments return to equilibrium with both J and v specificity.[91] Rates of chemical reactions are often controlled by how quickly excited or highly energetic species lose internal energy and return to rotational and vibrational thermal equilibrium.

As demonstrated here, 2DIR offers a unique capability for learning about both rotational and vibrational relaxation as a function of fluid density and thus can thus be exploited to provide critical tests of our fundamental theoretical understanding of small molecule relaxation in dense chemical reaction environments.[142]

The unique and readily tunable solvation properties of SCFs offer the potential for controlling chemical processes.[143] Additional interest in SCFs has been especially peaked by the use of sc-CO_2 and sc-H_2O as potential inexpensive "green" solvents.[144-146] Enhanced local density effects have been indicated to play a role in the special solvation properties of SCFs and identified in simulations.[147-152] In addition, the slowing of density fluctuations, due to long range spatial correlations near the critical point, is also a dynamical characteristic of the critical point phase region.[153-156] Only a relatively few direct time-domain measurements of molecular responses in SCFs have been reported. These include some vibrationally resonant ultrafast pump-probe experiments.[157-161] Very dramatic effects near the critical point are generally not observed in these lifetime and transient absorption data, and most pump-probe responses follow the density dependence of trends both below and above the critical density (ρ_c). However, a faster lifetime (T_1) was observed for an IR active mode of $W(CO)_6$ in supercritical CO_2, C_2H_6, and CHF_3 at densities just below ρ_c than expected by simple phenomenological trends, and T_1 remained essentially constant for a range of densities around the critical point, ~$0.6\rho_c$ to ~$1.4\rho_c$, when the temperature was near T_c.[157, 159] These near critical effects were reproduced by a theory based on mostly thermodynamic properties of the solvent,

neglecting local enhancement effects, and achieved good agreement with observed density dependence.[158-159] However, 2DIR may provide a more direct experimental measure of anomalous fluctuation dynamics and inhomogeneities near a critical point than lifetime measurements because this spectroscopic approach provides a direct, experimental measure of the transition energy *fluctuation* dynamics. This study is the first 2DIR report of the real time fluctuation dynamics in SCF solutions.

Furthermore, although the supercritical region is traditionally described as exhibiting single phase character, i.e. no liquid, vapor distinction, some thermodynamic properties have maxima where $P > P_c$ and $T > T_c$, and lines that connect these maxima have been used to distinguish gas and liquid like character in the SCF region. For example, a "Widom line" defined by the maxima of the constant pressure specific heat, or some other thermodynamic response functions, as a function of T extending from the critical point has served to divide the supercritical fluid into gas and liquid-like regions.[162-166] Another line dividing a supercritical fluid in two regions, a low-temperature "rigid" liquid and a high-temperature nonrigid gas-like fluid, the Frenkel line, has also been proposed.[167-168] Dynamics revealed by 2DIR may be expected to qualitatively change in supercritical regions where the Widom or Frenkel line boundaries can be identified and experimentally distinguish gas or liquid like supercritical regions.

As introduced above, a final aim of these studies is to learn how density dependent 2DIR measurements can reveal and identify the onset of liquid properties in supercritical and near-liquid density solutions and is made possible by our recent

characterization of free rotor 2DIR spectra in low density solutions.[91] There is an extensive literature on the observation and molecular-level interpretation of the vibrational spectra of small molecules, especially IR absorption spectra of hydrogen halides in high pressure and simple non-polar liquids, that closely relates to this 2DIR analysis.[138, 169-185] A characteristic phenomenological feature of these IR spectra is the observation of a broad and overlapping "triplet" structure for vibrational bands of diatomics in these liquids and high pressure fluids. The two feature or shoulders on the red and blue of the vibrational absorption band are attributed to unresolved *P* (ΔJ = -1) and *R* (ΔJ = +1) gas-phase-like rovibrational branches. The middle feature is close to the vibrational transition frequency observed in condensed phase FTIR spectra and suggests the interpretation of the center resonance as a *Q*-branch (ΔJ = 0). However, for all diatomics, and all parallel polarized vibrational bands, the *Q*-branch is strictly dipole symmetry-forbidden in free space[137, 186] due to conservation of angular momentum constraints.

Despite the simplicity of these fluid solutions, various theoretical and computational approaches have been applied to understand the appearance of these observed complex IR absorption lineshapes, characterized by the density dependent triplet structure and *Q*-branch like absorption intensity in high density environments. Explanations offered for these diatomics in liquid and dense fluid vibrational bandshapes span the range from dipole-induced-dipole effects,[171] *J*-mixing due to anisotropic interaction potential,[172] van der Waals complex formation or long lived anisotropic

spatial correlations in the fluid,[138, 173-174, 183] "modified rotor" or hindered rotor descriptions,[177-178, 185] to *P* and *R* spectral interference effects.[184] Some analyses have speculated that these complex lineshapes are due to both mixed free rotor character and modified rotor character resulting from slowly varying anisotropic solute-solvent potentials and the role of barriers on the lower lying rotational levels.[176, 180-182] The obvious *experimental* feature that limits more detailed interpretation of the high fluid density rovibrational absorption spectra is the lack of resolved rotational features. Hence, these broad, relatively structureless diatomic vibrational features in liquids and dense fluids still remain open to a variety of interpretations. As demonstrated here (*vide infra*) 2DIR studies can provide greater insight into the origins of this complex lineshape behavior.

Over the past two decades ultrafast two-dimensional infrared (2DIR) spectroscopy has been shown to be a powerful time-domain technique for learning about nuclear dynamics in the condensed phase on the femto- to picosecond time scale.[93, 139] Analysis of 2DIR spectra yields information on the nature of vibration lineshapes in terms of transition energy fluctuation dynamics and inhomogeneous broadening effects, the coupling of resonant intra- or intermolecular modes or the dynamics of chemical exchange between interconverting discrete molecular configurations or species.[94, 96, 187-189] This information is obtained by distributing the three-pulse vibrational response over a pump excitation frequency axis (ω_1) and a probe detection frequency axis (ω_3) as a function of T_w, the fixed time delay between the second and third pulse. Condensed phase

coherent 2DIR spectra resonant with a single vibrational absorption exhibit two oppositely signed spectral features at the $0 \rightarrow 1$ and the $1 \rightarrow 2$ vibrational frequencies which respectively result from ground state bleach and stimulated emission (GSB-SE), and excited state absorption (ESA) signal polarization pathways. The GSB-SE polarization response is centered at the pure vibrational resonance along the diagonal ($\omega_1 = \omega_3$), and the corresponding ESA signal is red-shifted along the probe frequency axis ω_3 by the $1 \rightarrow 2$ anharmonicity. Molecular fluctuation timescales due to bath interactions in these condensed phase systems are determined by the waiting time (T_w) dependence of the 2DIR lineshapes and correspond to the transition frequency-frequency correlation function (FFCF) of a resonantly excited vibrational mode.[139]

While all previous ultrafast 2DIR studies spectra have been carried out for vibrators in condensed phase solutions, we have recently described the first corresponding 2DIR analysis of a quasi free quantum rotor.[91] The 2DIR spectra of the resonantly excited ν_3 asymmetric stretching rovibrational band (2220 cm^{-1}) of N_2O in SF_6 gas at two densities ($\rho^* = \rho/\rho_c = 0.16$ and 0.30; $\rho_c = 0.74$ g $mL^{-1} = 5.79$ M) showed a qualitatively different and considerably more complex spectral signature than seen for the 2DIR spectra of isolated vibrational resonances in condensed phases. The N_2O ν_3 mode has strong oscillator strength ($\varepsilon \sim 1.5 \times 10^3$ M^{-1} cm^{-1}) in a relatively transparent region of the mid-IR spectrum and a small dipole moment (0.16D) allowing it to act as an effective small molecule probe in a wide variety of solutions. In addition, the N_2O ν_3 mode is

relatively long lived[190] (*vide infra*) thus enabling 2DIR fluctuation dynamics measurements for relatively long timescales, as seen below. SF_6 is a relatively simple, chemically inert, non-polar fluid with a readily accessible critical point (T_c = 45.6°C, P_c = 36.6 atm). At early waiting times spectral 'X' shapes displaced by the ν_3 anharmonicity along the ω_3 axis identifies 2DIR features attributable to ground state bleach and excited state absorption contributions to the N_2O 2DIR spectrum.[91] The elongated spectral shape along the diagonal ($\omega_1 = \omega_3$) and the parallel component red-shifted in the ω_3 direction by the ν_3 1 $\rightarrow$ 2 transition anharmonicity (~28 cm^{-1}) in the early time ($T_w \sim$ 0.2 ps), are the well-known 2DIR signatures of an inhomogeneously broadened vibrational band. The corresponding anti-diagonal features seen in these quasi-free rotor spectra are not observed in condensed phase and are the key spectral feature that identifies a population of free rotors in a 2DIR spectrum. The initial elongated features all approach symmetrical shapes at longer waiting times which is the well-known signature of transition frequency memory loss, the 2DIR spectral characteristic of spectral diffusion processes in liquid phase environments. The T_w dependence of these 2DIR spectra showed that ν_3 N_2O rotational relaxation occurred in ~1.5 collisions at both moderately dense ρ^* = 0.16 and 0.30 SF_6 environments (9.5 ps and 6.0 ps, respectively). The goal here is to extend these 2DIR measurements of N_2O's ν_3 band in higher densities of SF_6, including state points in the vicinity of the critical point and above, as well as in liquid SF_6 to learn about the density dependent rates of *J*-scrambling (rotational) and vibrational energy loss, relaxation in the critical point region and evidence of the onset of liquid-like character in

this system. These nonlinear spectroscopic studies allow experimental tests of the adequacy of independent binary collision (IBC) relaxation models in dense fluids, determine how solute-solvent intermolecular properties separately influence rotational and vibrational relaxation, and characterize the transition from gas to condensed phase dynamics, at high densities, where attributes of both solvation environments may be simultaneously present.

4.2 Experimental

Sample Preparation

Solutions used for the SF_6 studies were prepared in a custom variable path-length stainless steel sample cell. The sample cell uses 2 mm CaF_2 windows and a 100μm Teflon spacer in a U-shape to allow for gas to flow into the optical chamber. To form high pressure seals, Teflon O-rings (McMaster Carr) were used. The pressure was measured using a PX-603 thin-film pressure transducer (Omega Engineering) and protected using a pressure scrubber, read out by a benchtop pressure meter (DP25B-S, OMEGA Engineering, Inc.) to a precision of ±1 psi. Heating was achieved using a rope heater (Omega Engineering) using a heating control box with a feedback loop passed through a rheostat. The rope heater was wrapped around the body of the sample cell and the attached tubing to achieve the state points mentioned. A temperature probe was screwed into the body of the sample cell to effectively measure the temperature closest to the optical area.

N_2O (99.999%, Linde Gas) and SF_6 (99.8%, Praxair, Inc.) were used for the experiments. Testing was done to get the optimal fill ratios. First, the sample cell and high pressure gas setup was vacuumed to less than 200 mtorr. For the below supercritical samples, the N_2O was filled to ~45 psi in the sample cell. The sample cell was closed off and the rest of the system was vacuumed again to below 200 mtorr. SF_6 was then filled into the pressure generator (HiP 87-6-5) at tank pressure, ~300 psi. The sample cell and pressure generator were then equilibrated, dropping the overall pressure to ~200 psi. The pressure generator allowed for compression of the gas up to 60 mL. The pressure was increased to the desired state point. If the pressure was not at the correct level, the sample cell was closed off, the pressure generator was vacuumed and filled with more SF_6. This was repeated until the desired pressure was achieved. For those state points above room temperature, the pressure generator was also wrapped in a heating rope along with the sample cell. Everything was heated and let equilibrate for 1 hour before compression in order to get proper mixing and to avoid cold pockets where the SF_6 could potentially condense into liquid.

The final N_2O/SF_6 mixtures were allowed to equilibrate for ~24 hours before taking spectroscopic measurements to ensure complete mixing. The temperature control was achieved by wrapping an electric rope heater (Omega Engineering, Inc.) around the cell body and piping. The electric rope heater was controlled by a benchtop temperature controller (CSi32K-C24, OMEGA Engineering, Inc.) with a K-type bolt-on thermocouple wire (WTK-10-60, OMEGA Engineering, Inc.) for temperature feedback. Proportional

integral derivative (PID) control was used to regulate and maintain temperatures to within ±0.1°C.

Ultrafast spectroscopy setup

A diode-pumped Legend Elite Duo (Coherent, Inc.) Ti:sapphire regenerative amplifier produces ultrafast pulses centered at 800 nm at a 1 kHz repetition rate with energies of 7.5 mJ/pulse, a pulse duration of 40 fs, and a bandwidth of 30 nm. The 800 nm output undergoes nonlinear down conversion through a TOPAS-C (Light Conversion) optical parametric amplifier (OPA) incorporating β-BaB_2O_4 (BBO) crystals to generate 1.3 and 1.8 μm signal and idler beams, respectively. Infrared pulses (10 μJ, 80 fs, 250 cm^{-1} FWHM) centered at 4.5 μm (~2222 cm^{-1}) are produced by collinear combination of the OPA output beams in a difference frequency generation (DFG) $AgGaS_2$ crystal.

The 2DIR spectrometer is set up in a compact pump-probe geometry described elsewhere[110], in which the two collinear pump beams are outputs of a modified Mach-Zender/Michelson interferometer, and the probe beam is a reflection off a 0.5º BaF_2 wedge. The IR beams are expanded and tightly focused onto the sample by a parabolic mirror to a focal spot diameter of ~100 μm. The phase-matched direction of the coherent, heterodyne-detected signal (incorporating spatially overlapped rephasing and non-rephasing contributions as well as a local oscillator for phase resolution and signal amplification) is in the probe direction. The heterodyned signal is dispersed in a monochromator (Princeton Instruments, Inc.) by grating, and detected by a double-array

32 element MCT detector (InfraRed Associates, Inc.) with a resolution of 3 cm^{-1}/pixel. 2DIR spectra are collected in perpendicular polarization geometry <*XXYY*>.

Linear FTIR (Fourier transform infrared) spectra were collected on a ThermoNicolet Nexus 670 FTIR spectrometer at 0.125 cm^{-1} resolution using Happ-Genzel apodization. The maximum FTIR absorbance of the N_2O ν_3 band was kept in the range of ~0.3-0.5 OD. The pump-probe signal, obtained on the same 2DIR set-up, is reported as the change in optical density of the sample measured by the probe beam in the absence and presence of the pump beam, as a function of the interpulse delay time. The polarization of the pump beam is set at the magic angle (54.7°) to eliminate polarization effects.

Rate equations for one-color N_2O ν_3 pump-probe response in SF_6 corresponding

The differential rate equations for the N_2O ν_3 pump-probe responses in SF_6 are given by:

$$\frac{dN_{001}}{dt} = -\frac{N_{001}(t)}{T_1} \quad \text{(Eq. 4.1)}$$

$$\frac{dN_{100}}{dt} = \frac{N_{001}(t)}{T_1} - \frac{N_{100}(t)}{T_2} \quad \text{(Eq. 4.2)}$$

$$\frac{dN_{000}}{dt} = \frac{N_{100}(t)}{T_2} \quad \text{(Eq. 4.3)}$$

The time-dependent populations within this model are given by:

$$N_{001}(t) \propto e^{-t/T_1} \quad \text{(Eq. 4.4)}$$

$$N_{100}(t) \propto \frac{T_2}{T_2-T_1} e^{-t/T_2} - \frac{T_2}{T_2-T_1} e^{-t/T_1} \quad \text{(Eq. 4.5)}$$

$$N_{000}(t) \propto 1 - \frac{T_2}{T_2-T_1} e^{-t/T_2} + \frac{T_1}{T_2-T_1} e^{-t/T_1} \quad \text{(Eq. 4.6)}$$

The corresponding normalized pump-probe signal at delay time t is correspondingly given by:

$$\Delta OD(t) = C_1 e^{-k_1 t} - C_2\left(\frac{k_1}{k_1 - k_2} e^{-k_1 t} - \frac{k_1}{k_1 - k_2} e^{-k_2 t}\right) \quad \text{(Eq. 4.7)}$$

where C_1 and C_2 are proportional to the $(00^00) \rightarrow (00^01)$ and $(10^00) \rightarrow (10^01)$ absorption cross sections respectively, and k_1 and k_2 are the inverse lifetimes of the ν_3 and ν_1 N_2O states, respectively. The fit parameters, i.e., the coefficients and lifetimes, are given for all densities in **Table 4.2**.

4.3 Results and Discussion

N_2O ν_3 absorption spectra as a function of SF_6 density

Normalized FTIR absorption spectra of the N_2O ν_3 asymmetric stretch in different SF_6 density solutions are shown in **Figure 4.1**. These spectra highlight the continuous evolution of the ν_3 absorption lineshape from the gas to liquid phase. The $0 \rightarrow 1$ ν_3 excitation is a parallel polarized transition, and thus no Q-branch is formally allowed for the gas phase spectra.[137] Rotational fine structure is not evident in any of these spectra due to the broadening of the individual *P(J)* and R(*J)* discrete transitions. At the two lowest, gas-like SF_6 solvent densities shown here,[91] $\rho^* = 0.16$ (40˚C, 17 atm, $0.98T_c$, $0.46P_c$) and $\rho^* = 0.30$ (40˚C, 26 atm, $0.98T_c$, $0.71P_c$), *P* and *R* rovibrational branches are observed with easily resolvable peak maxima centered at 2211 cm^{-1} and 2236 cm^{-1}, respectively. In this modest density regime, the larger relative absorption in the "forbidden" *Q*-branch region (~2021 cm^{-1}) in the $\rho^* = 0.30$ spectrum (blue) is the most obvious difference.

As the SF_6 density increases further (**Figure 4.1**), the *P* and *R* branches become progressively less distinct and absorption intensity grows in the ν_3 *Q*-branch region. *P* and *R* branch maxima are still identifiable in ρ^* = 0.67 (48˚C, 37.9 atm, 1.02T_c, 1.05P_c) and 0.86 (48˚C, 38.8 atm, 1.01T_c, 1.05P_c) solutions, and but become nearly indistinguishable at ρ^* = 0.99 (50˚C, 40.7 atm, 1.01T_c, 1.10P_c). At higher density, the vestige of *P* and *R* branches are barely evident as weak shoulders and the largest intensity is now in the *Q*-branch region as seen for the ρ^* = 1.36 (48˚C, 41.3 atm, 1.01T_c, 1.12P_c) fluid solution spectrum (**Figure 4.1**). Note the ρ^* = 0.16 and 0.30 spectra are in the gas phase, and the ρ^* = 0.67, 0.86, 0.99 and 1.36 are all in the supercritical phase.

In contrast, the lineshape of the N_2O ν_3 in liquid SF_6 (ρ^*= 1.87, 20˚C, 22 atm, 0.92T_c, 0.60P_c) absorption spectrum is qualitatively different (**Figure 4.1**). All vestiges of *P* and *R* branches are completely absent and a nearly Lorentzian band shape with a single peak frequency (2221 cm^{-1}) is observed for ν_3 in liquid SF_6 at ρ^*= 1.87. The small absorption feature at ~2209 cm^{-1} in this spectrum is due a bending ν_2 (589 cm^{-1}) hot band absorption ($\nu_2 \rightarrow \nu_2 + \nu_3$) as noted previously.[60, 191] Interestingly, this small hot-band feature is only clearly evident for N_2O in liquid phase environments (SF_6, H_2O and octanol). No rovibrational structure appears in any condensed phase N_2O ν_3 absorption spectrum.[2, 60, 191-193] In liquids, the N_2O ν_3 transition frequency is highly sensitive to solvent polarity.[193] The observed peak is at 2221 cm^{-1} in liquid SF_6 and only slightly red-shifted (2220 cm^{-1}) from that in the less dense supercritical SF_6 at ρ^* = 1.36.

2DIR spectra of N_2O ν_3 mode in dense gas and supercritical SF_6

2DIR spectra of the N_2O ν_3 mode in SF_6 at densities corresponding to the absorption spectra in **Figure 4.1** are shown in **Figure 4.2** as a function of some representative waiting times, T_w. These samples correspond to gas phase ($\rho^* = 0.16$) and supercritical state points, including state points near SF_6 ρ_c and approaching liquid density ($\rho^* = 1.36$). The "X" shape, most evident at early times in the $\rho^* = 0.16$ spectrum, fundamentally originates from the strict $\Delta J = \pm 1$ selection rule for each $\Delta\nu = \pm 1$ transition of a free rotor that contributes to the $P^{(3)}$ density matrix pathways contributing to the 2DIR signal response.[91] For an inhomogeneously broadened system, this leads to diagonal and the anti-diagonal "X" – like 2DIR features for an ensemble of quasi-free rotors at early T_w times for both GSB-SE and ESA contributions, as described earlier and evident in **Figure 4.2**. The ESA contribution is red-shifted in the ω_3 direction by the N_2O ν_3 $1 \rightarrow 2$ transition anharmonicity (~28 cm^{-1}). Thus, any "X" like character in the 2DIR spectrum indicates quasi-free rotor character in the sample ensemble. The elongated shapes observed at the shorter T_w's result from the initial predominant inhomogeneous character of the ensemble of *J*-specific allowed rovibrational transitions.[91]

The underlying fluctuation dynamics of the system that determines the observed T_w dependence of these 2DIR spectra is captured by a stochastic Gaussian line broadening model.[194] Following the treatment of the 2DIR spectra for free rotors given previously,[91] lower density absorption spectra were modeled as separate transition

frequency-frequency correlations (FFCF) given by the familiar Kubo lineshape formulism and centered on the *R* and *P* branch peaks:[194]

$$C_{1R,1R}(t) = \left\langle d\omega_{10}^{R}(t) d\omega_{10}^{R}(0) \right\rangle = +\Delta_{10}^{R}\Delta_{10}^{R} e^{-t/\tau_c} \qquad \text{(Eq. 4.8a)}$$

$$C_{1P,1P}(t) = \left\langle d\omega_{10}^{P}(t) d\omega_{10}^{P}(0) \right\rangle = +\Delta_{10}^{P}\Delta_{10}^{P} e^{-t/\tau_c} \qquad \text{(Eq. 4.8b)}$$

where $\omega_{10}^{P}(t) = \omega_{10}^{P^o} + d\omega_{10}^{P}(t)$ and $\omega_{10}^{R}(t) = \omega_{10}^{R^o} + d\omega_{10}^{R}(t)$, and $\omega_{10}^{P^o}$ ($\omega_{10}^{R^o}$) corresponds to the P (R) branch maximum. $\Delta_{10}^{P}, \Delta_{10}^{R}$ are the initial instantaneous widths of the corresponding $0 \rightarrow 1$ *P* and *R* rovibrational branches, and τ_c is the transition energy fluctuation time scale. In addition to these FFCF autocorrelations, a FFCF cross-correlation function is required to capture the structure and dynamics of the free rotor 2DIR spectra and its perfectly anticorrelated features:[91]

$$C_{1P,1R}(t) = C_{1R,1P}(t) = \left\langle d\omega_{10}^{P}(t) d\omega_{10}^{R}(0) \right\rangle = -\Delta_{10}^{P}\Delta_{10}^{R} e^{-t/\tau_c} \qquad \text{(Eq. 4.9)}$$

Changes in the aspect ratio of the elongated 2DIR spectral lineshapes as a function of T_w captures the decay of the FFCF.[195] The center line slope (CLS) method was used to quantify the T_w dependence of the initial elongated 2DIR features and thus the FFCF decay constant, τ_c.[195] The CLS at a given T_w is determined by the slope of the line that connects the maxima of the peaks of a series of cuts through the 2D spectrum parallel to the ω_1 frequency axis. τ_c is a measure of the spectral diffusion dynamics or equivalently

the timescale for *J*-specific initial transition frequency memory loss, *J*-scrambling, due to bath interactions.[91] More specifically, for these gas/fluid phase environments, it corresponds to the time for the excited rotational distribution to return to equilibrium as result of collisions of N_2O with the SF_6 solvent/bath.

The CLS determined FFCF for the diagonal and anti-diagonal GSB-SE components of the 2DIR spectra shown in **Figure 4.2** are also correspondingly plotted in this figure. Excellent exponential best-fits are obtained at each density. The CLS best-fit determined exponential rotational relaxation times, τ_c, as a function of SF_6 reduced density are summarized in **Table 4.1**. As noted in our earlier lower density report, a very small (~5%) slow second FFCF component is found at all densities. This component provides a positive constant offset on the signal T_w timescale and interestingly has positive sign on both the diagonal and anti-diagonal contributions. (2DIR and CLS decays for the ρ^* = 0.86 state point, 48°C, 38.8 atm, 1.00T_c, 1.06P_c, are shown in supplementary information for conciseness.)

Qualitative systematic trends are evident in the N_2O ν_3 2DIR spectra as a function of SF_6 density. At the lowest densities studied[91] (ρ^* = 0.16 and ρ^* = 0.30), eight distinct elongated signals are evident at early T_w times. Four contribute each to GSB-SE and ESA pathways, which carry different signed signals. However only four symmetrized features are evident at long times, where the FFCF is ≈ 0, because the N_2O ν_3 vibrational anharmonicity (28 cm^{-1}) almost exactly matches the frequency difference between *P* and *R* branch maxima (25 cm^{-1}) at the experimental temperatures (~40ºC). Consequently the

symmetrized diagonal GSB-SE contribution of the *P* transition almost exactly cancels the (*P*, *R*) ESA cross-peak, and the cross-peak (*R*, *P*) GSB-SE signals effectively cancel the ESA of the *R* transitions.[91]

In analogy to loss of distinct *P* and *R* branch structure in the FTIR spectra as the SF_6 density increases and described above (**Figure 4.1**), the 2DIR spectra also exhibit less resolved rotational features with increasing SF_6 density. For example, the eight readily distinguished elongated feature at early times and four at long times evident at $\rho^* = 0.16$, are difficult or impossible to distinguish for the higher densities (**Figure 4.2**). Cancellation of the overlapping diagonal *P* GSB-SE and ESA anti-diagonal (*P*, *R*) cross-peak, and the overlapping GSB-SE (*R*, *P*) cross-peak and ESA (*R*, *R*) features are already broadened at our shortest T_w at densities of $\rho^* = 0.67$ and higher so that this 2DIR spectral region shows no signal. However, the unique anti-diagonal 2DIR signature of free rotor character *persists at all these dense gas and supercritical densities* thus allowing precise determination of *J*-scrambling or rotational relaxation times *even in the absence of any rotational resolution* in the corresponding linear spectra. This anti-diagonal 2DIR spectral structure in particular indicates some component of the resonant ensemble has free rotor character **Figure 4.2**). The T_w dependence of the collapse of the 2DIR anti-diagonal and diagonal structure provides this unique capability for studying rotational relaxation in high density fluids.

As the density or collision frequency increases from $\rho^* = 0.16$ to 1.36, a factor of 8.5 the timescale of rotational relaxation, τ_c, decreases from 9.4 ps to 1.35 ps, roughly a

factor of 7. CLS decays of both the diagonal and antidiagonal yield decays within the precision of these measurements. If we use calculated mean free times between N_2O and SF_6 collisions (τ_{coll}) based on hard sphere calculations (see SI), the number of collisions at each density that are required for N_2O to rotationally relax is given by $Z_{rot} = \tau_c/\tau_{coll}$. The 2DIR determined rotational relaxation times, τ_c and Z_{rot}, are plotted as a function of fluid density in **Figure 4.3a**. As seen in the figure (and Table 1), rotational equilibration occurs within 1 to 2 collisions over this order of magnitude range of SF_6 fluid densities. Thus, as noted previously for the lowest density dense gas phase 2DIR analysis,[91] J memory loss due to collisions remains a highly efficient process in the supercritical region. The efficiency of rotational relaxation will be contrast with that of vibrational relaxation at these state points subsequently. The rate of rotational relaxation is nearly constant in this density region in terms of Z_{rot}, the number of SF_6 collisions to achieve rotational equilibrium, and thus the independent binary collision model is adequate for describing the relaxation dynamics at all these supercritical and gas state points. However, the data suggests there may be a small slowing effect at $\rho^* = 0.99$ (Z_{rot} maximum) or a small plateau in this region as the critical density is approached ($\sim\rho^* =$ 0.86 to 0.99). This feature is better seen by plotting the fluctuation rate ($1/\tau_c$) as a function of density (**Figure 4.3b**). The dashed straight line, extending from the origin, consistent with an IBC description, to the $\rho^* = 1.36$ rate, is a visual aid highlighting the fluctuation slowing in the critical point region. This density dependent data is consistent with critical fluctuation slowing effect and a potential plateau region in the critical point

region. This effect is analogous to the $W(CO)_6$ lifetime effects in the same supercritical phase region of other fluids and is consistent with the analysis and conclusions of those SCF studies.[157-159, 196]

2DIR spectra of N_2O ν_3 mode in liquid SF_6.

The 2DIR spectrum of the N_2O ν_3 mode in liquid SF_6 (ρ^* = 1.87 at 20°C, 22 atm, $0.92T_c$, $0.60P_c$) is shown in Fig. 4 for T_w = 0.2 and 1.0 ps. Unlike the 2DIR N_2O in SF_6 spectra in gas and supercritical phase state points, no anti-diagonal features can be detected in the 2DIR of ν_3 in the liquid SF_6 environment even at the earliest T_w (0.2 ps). Thus, in contrast to the lower density fluids, no evidence of N_2O free rotor character can be detected in the liquid SF_6 2DIR spectra at this state point. This is consistent with the linear absorption spectrum where no vestiges of rotational branches can be detected (**Figure 4.1**).

Furthermore, the spectrum is already fully symmetrized by 0.2 ps and no meaningful 2DIR shape changes are detected as a function of T_w (**Figure 4.4**). This 2DIR spectrum characterizes a vibrational feature dominated by a single homogeneous dephasing time lacking any inhomogeneous character or spectral diffusion, at least at the limit of current IR pulse durations. The decay dynamics of the relevant FFCF for this N_2O mode at this solution state point, $\tau_c << 0.2$ ps, is consistent with the observed near Lorentzian character of the observed vibrational absorption lineshape (**Figure 4.1**, and **Figure 4.5**). The rapid fluctuation FFCF dynamics of the N_2O ν_3 mode in liquid SF_6 stands in contrast to photon echo results for N_2O solvated in octanol or water where

significantly slower fluctuation processes are found and instantaneous vibrational frequency memory loss occurs on much longer timescales.[197]

Estimates of non-free rotor N_2O character in FTIR as a function of SF_6 density.

All 2DIR spectra unequivocally show free rotor character at the investigated SF_6 non-liquid state points. These results can be used to provide experimental evidence for understanding the observed density dependent absorption spectra (**Figure 4.1**) and the onset of liquid character in these systems. Extensions of these results to the long-studied triplet structure and anomalous *Q*-branch intensity for solutions of hydrogen halides in simple liquids follow as well. As demonstrated previously,[91] the N_2O ν_3 absorption spectra at the lowest densities studied here are phenomenologically well fit by a stochastic Gaussian line broadening model. Each *P* and *R* branch envelope is represented by Kubo lineshape functions only requiring $\Delta_{10}^{P}, \Delta_{10}^{R}$ and τ_c (Eq. 4.8a, 4.8b). Analysis of the 2DIR determines the fluctuation time scale, τ_c, due to N_2O-SF_6 collisions at each density. Given this experimental value of τ_c, best fits to the observed ρ^* = 0.16 and 0.30 absorption spectra determined $\Delta_{10}^{P}, \Delta_{10}^{R}$. Excellent fits to the FTIR were obtained except in the spectral wings which is to be expected given the non-Gaussian character of the *P* and *R* branch spectral shapes in those spectral regions.[91] If we assume the distribution of initial, instantaneous *J* transition frequencies, which are mostly determined by rotational constants and temperature, $\Delta_{10}^{P}, \Delta_{10}^{R}$, is essentially unchanged as the fluid density increases, then the 2DIR determined τ_c values (**Table 4.1**) allow the calculation of the

corresponding free rotor N_2O ν_3 absorption spectrum at each SF_6 density. The Gaussian widths for the *P* and *R* branch *J* transitions were found to be 21.4 cm^{-1} and 17.7 cm^{-1}, respectively, resulting from the best fits to lowest density $\rho^* = 0.16$ absorption spectrum using the corresponding 2DIR CLS decay result for τ_c (9.4 ps).

The calculated free rotor spectrum, using the fluctuation times, τ_c, obtained from the 2DIR spectral analysis, i.e. CLS decay, at each SF_6 density > 0.16 and the low pressure $\Delta_{10}^{P}, \Delta_{10}^{R}$ widths are shown (red line) in **Figure 4.6**. These free-rotor spectra are compared to the observed FTIR spectra (blue line) at each density in this figure as well. This lineshape comparison reveals that the intensity in the *Q*-branch region cannot be captured by the free rotor absorption character as the density increases. To better estimate how the non-free rotor character in the *Q*-branch region is increasing with density, the calculated spectrum has been subtracted from the experimental one with the relative scaling determined so that the rotor contribution is as large as possible without resulting a negative difference spectrum. The difference spectrum in the *Q*-branch region is the blue shaded area in **Figure 4.6**. Again, we are ignoring the difference spectrum in the absorption wings of the vibrational band where this modeling is not quantitative due to the Gaussian frequency distribution inherent to this lineshape model.[91] Despite this limitation far from the band center, this model succeeds in providing a 2DIR based interpretation of the most salient features of the experimental absorption spectra. The blue shaded portion of the difference spectra represents the forbidden "*Q*-branch" region spanning the range from ~2211-2236 cm^{-1} with a peak at ~2221 cm^{-1}, the liquid density

peak frequency. This absorption component increases with density in the range as the system change from the more gas-like modest density environment to the more liquid-like higher density supercritical environment.

The resulting interpretation of the above analysis, based on the 2DIR results, is that there are simultaneously two types of N_2O molecules in the ensemble that contribute to the absorption spectra in high density SF_6 fluids in this spectral region; one is a free rotor gas phase species and the other is a hindered or liquid like solvated species. Once the solvent condenses, no free rotor population remains, as seen for the SF_6 liquid absorption and 2DIR, and vibrators can be best characterized by a rotational diffusive or librational response. The hindered/solvated rotors component accounts for the "*Q*-branch" type absorption features in this high fluid density as pictured in **Figure 4.7**. Heuristically, the ratio of free rotor to liquid-like population contributing to the ν_3 spectroscopic features, $P_{rot/liq}(r)$, may be given by an Arrhenius type of expression describing the probability that a N_2O rovibrational level passes over a slowly varying, local density dependent SF_6 barrier, $E_{bar}(r)$:

$$P_{rot/liq}(r) \propto \exp\left(- \frac{E_{bar}(r)}{E_{rot}(J)} \right) \qquad (3)$$

For low densities, $E_{bar}(r) \sim 0$, $P_{rot/liq}(r) \sim 1$ and the system is all free rotors showing *P* and *R* branch structure only, as for example in the $\rho^* = 0.16$ sample. For the liquid limit $E_{bar}(r) \sim ¥$, $P_{rot/liq}(r) \sim 0$ and only a more liquid-like, hindered rotor *Q* branch

spectrum is observed, i.e. the ρ^* = 1.87 sample. At a specific density in between these two limits, $E_{bar}(r) \sim kT$ and thus the more rotationally and translationally energetic N_2O molecules are above the barrier and result in the sub-ensemble that accounts for the free rotor spectrum. Such an explanation was proposed for the absorption spectrum of HCl in near and supercritical SF_6.[181] The presence of the *Q* branch-like feature in the absorption spectra of N_2O in SF_6, made possible by this 2DIR analysis **Figure 4.6**), is a key experimental attribute signifying the onset of liquid-like character in the fluid that coexists with free rotors at a given state point. Thus the sample is spectroscopically inhomogeneous not just due to the distribution of barrier heights or solvation environments but, at a given solvation environment or spatial location, the molecular distribution of rotational energy relative to the barrier size will also result in sub-ensembles of free rotor or hindered rotor spectral signatures.

N_2O ν_3 vibrational energy relaxation as a function of SF_6 density.

To contrast the 2DIR rotational dynamics given by the CLS decays with the timescale of the N_2O ν_3 vibrational energy relaxation, magic angle, one-color pump-probe measurements for each of the SF_6 solutions studied here were carried out. The density-dependence and relative collision efficiency of these vibrational energy relaxation (VER) rates can be compared with the *J*-scrambling spectral diffusion dynamics revealed by the 2DIR analysis. Furthermore, the effects of the supercritical and liquid SF_6 environments on N_2O ν_3 VER may be contrasted with that of moderately dense gas phase.

The magic angle, one-color, pump-probe responses of the ν_3 $\nu = 1$ excited state of N_2O in SF_6 for all the state points studied here are shown in supplementary information. To avoid complications due to overlapping GSB-SA and ESA contributions, the *ΔOD(t)* signal integrated over ~30 cm^{-1} of the dispersed pump-probe signal, centered at 2240 cm^{-1} of the ν_3 rovibrational band, are reported here. A bi-exponential decay is observed for all the ν_3 N_2O in SF_6 pump-probe responses regardless of solution phase; gas, supercritical and liquid. In order to most accurately determine vibration relaxation rates and rationalize this biexponential decay character, the following VER mechanism and corresponding kinetic scheme is proposed. Due to the low density of states for this triatomic in the asymmetric stretch region, collisions are required for the dissipation of vibrational energy in these N_2O/SF_6 solutions. The highest frequency fundamental in SF_6 is the 948 cm^{-1} asymmetric stretching mode and it is mismatched with the N_2O ν_3 energy by ~ 1270 cm^{-1}. Thus the most rapid vibrational decay pathway minimally involves two receiving modes.[198] Vibrational levels contributing to the proposed ν_3 VER mechanism and biexponential pump-probe signal are diagramed in **Figure 4.8**. (00^00), (10^00), (00^01), (10^01), and (00^02) correspond to the ground, symmetric stretch, asymmetric stretch, symmetric-asymmetric stretch combination ($\nu_1+\nu_3$), and asymmetric stretch overtone of N_2O, respectively. The red vertical lines correspond to allowed dipole transitions within the pump/probe pulse bandwidth, and $\sigma_{002,001}$, etc. are the absorption cross-sections for the (00^01) $\rightarrow$ (00^02), etc. transitions.

Since the energy level gap (~940 cm^{-1}) between the excited N_2O ν_3 (00^01) at ~2220 cm^{-1} and ν_3 symmetric stretch (10^00) center at ~1285 cm^{-1} effectively matches the SF_6 ν_3 asymmetric stretching mode at 948 cm^{-1} (**Figure 4.8**), the fastest decay component in the pump-probe response and the rate of N_2O ν_3 vibrational loss is attributed to resonant V $\rightarrow$ V collisional energy exchange resulting in the excitation of the SF_6 ν_3 and the N_2O ν_1 modes. Vibrational relaxation redistribution through V $\rightarrow$ V processes is relatively rapid compared to V $\rightarrow$ T/R and is generally the first step in the VER of polyatomic systems.[199-201] The second, slower component observed in the one-color pump-probe responses is attributed to the dipole allowed N_2O (10^00) $\rightarrow$ (10^01) absorption, which falls in the frequency width of our probe pulse and consequently the second $\Delta OD(t)$ decay component reflects the longer lifetime of the symmetric stretch level (10^00).

Rate equations for this one-color N_2O ν_3 pump-probe response in SF_6 corresponding to mechanism discussed above and illustrated by the energy level diagram in **Figure 4.8** are given in the supplementary information. The corresponding normalized pump-probe signal at delay time t is given by:

$$\Delta OD(t) = C_1 e^{-k_1 t} - C_2 \left(\frac{k_1}{k_1 - k_2} e^{-k_1 t} - \frac{k_1}{k_1 - k_2} e^{-k_2 t} \right) \qquad \text{(Eq. 4.10)}$$

where C_1 and C_2 are proportional to the (00^00) $\rightarrow$ (00^01) and (10^00) $\rightarrow$ (10^01) absorption cross sections respectively, and k_1 and k_2 are the inverse lifetimes of the ν_3 and ν_1 N_2O states respectively. Excellent fits to this kinetic model are obtained at all densities

including the SF_6 liquid. See SI for a representative best-fit to the ν_3 resonant pump-probe response in ρ^* = 0.86 SF_6 and the component kinetics for the ν_3 vibrational energy relaxation and the subsequent ν_1 population build up. The coefficients and lifetimes determined by best fits of Eq. 4.10 to the observed pump-probe responses at a given solution density (ρ^*) are summarized in **Table 4.2**.

The relative absorption strengths, $C_1 / C_2 \gg 2$ at each state point, including the liquid, is consistent with the kinetic mechanism illustrated in **Figure 4.8**. The vibrational lifetimes of the ν_3 vibrational energy decay ($\tau_1 = 1/k_1$) and $Z_{vib} = \tau_1/\tau_{coll}$, the ν_3 lifetimes in terms of number of hard sphere collisions at each dense gas and supercritical state point, in analogy to the plot of rotational relaxation times (**Figure 4.3a**), are shown in **Figure 4.9**. Just as found for the rotational relaxation rate, the vibrational relaxation rate increased by nearly an order of magitude as density increased in the ρ^* = 0.16 to 1.36 range and effectively scaled with the number of SF_6 collisions (**Figure 4.9**). That is, regardless of the density in this regime $Z_{vib} \approx 14$ thus again supporting an independent binary collision description for the dynamics at these state points. However, for rotational relaxation (τ_c) $Z_{rot} \approx 1.5 - 2$ as described above for this solute-bath system. Thus, the 2DIR results reveal that SF_6 collisions are a factor of ~10 more efficient at relaxing rotational energy in the ν_3 excited fundamental level. However, while rotational equilibrium is re-established < 10 ps after excitation depending on the density, complete

vibrational cooling, returning the system to vibrational equilibrium, occurs on the ~ ns timescale (Table 2) in this $SF_6 - N_2O$ system.

The slower $\Delta OD(t)$ decay time scale, τ_2 $(1/k_2)$, is ~ 30 - 40 times slower than τ_1. The current 200 ps range of our pump-probe delay limits the precision of the reported τ_2, the lifetime of the N_2O symmetric stretch fundamental (10^00). The vibrational energy level structures of the N_2O – SF_6 collision partners **Figure 4.8**) accounts for the difference of these two decay rates. Unlike the proposed mechanism for N_2O vibrational relaxation from (00^01) to (10^00), there is no single SF_6 vibrational level resonant with the N_2O ν_1 energy so its relaxation to the ground state is governed by a higher process requiring three receiving modes, and hence the ~ 30 - 40 times slower VER rate for this ν_1 component of the $\Delta OD(t)$ decay.[198, 202] At ρ^* = 0.99, the second decay component appears to be slower than the corresponding ν_1 energy relaxation rate at ρ^* ~ 0.86 or 1.36. This may be attributed to critical point dynamical effects, however, given the 200 ps limit of our pump-probe, we leave further comment on these slower dynamics to a subsequent study.

4.4 Conclusion

Data are presented demonstrating that ultrafast 2DIR, when combined with conventional pump-probe spectroscopy, can be an effective tool for measuring the distinct rates of excited state rotational and vibrational relaxation for small molecules in high density gases and supercritical fluids where no discrete rovibrational resolution is evident in the corresponding linear absorption spectrum. In particular, the observation of

anti-diagonal features in the 2DIR spectrum unequivocally identifies free rotor character in the molecular ensemble and is evident in the 2DIR for all the dense gas and supercritical state points examined here, $0.16 \leq \rho^* \leq 1.37$. For the N_2O ν_3 fundamental in SF_6, rotational energy equilibration occurs in 1 – 2 collisions at each state point from the dense gas to the supercritical fluid region, and thus rotational equilibration is a highly efficient process across all these density state points in this fluid system. In contrast, ν_3 vibrational energy loss is an order of magnitude slower than *J*-scrambling at each corresponding density, requiring ~14 SF_6 collisions to achieve VER and complete equilibration of vibrational energy occurs on the ~ ns timescale. Furthermore, these results establish that an IBC description is sufficient to describe the solvation dynamics in the gas and supercritical regime for this system. Unlike the supercritical fluid solutions however, the 2DIR of N_2O in liquid SF_6 ($\rho^* = 1.87$) shows no free rotor character and the ν_3 absorption lineshape is in the rapid fluctuation limit described by a FFCF with a fluctuation timescale << 0.2 ps.

The 2DIR determined time scale for rotational equilibration, Z_{rot} 1-2 N_2O-SF_6 collisions at all fluid densities is consistent with previously reported rates of rotation-to-translation energy transfer near room temperature where typically 1–10 collisions suffice for rotational relaxation.[203-204] Interestingly, Z_{rot} ~ 1.3 – 2 was estimated for (neat) N_2O vapor from ultrasonic measurements in agreement with the more direct ultrafast 2DIR results in dense SF_6 despite ~10^5 difference in fluid density.[205] Traditional techniques for measuring rotational relaxation dynamics[204] include different versions of pump-probe

spectroscopy,[206-208] resonance fluorescence,[209] shock wave analysis[210] and ultrasonic absorption.[205, 210-212] However, these techniques are restricted to low pressure regimes unlike the 2DIR methodology which can report on rotational relaxation dynamics in high temperature and pressure regions of phase space as shown here.

For the wide range of densities studied here ($\rho^* = 0.16 - 1.87$), the N_2O ν_3 rovibrational total bandwidth, including the liquid state point, decreases by just a factor of ~2 (**Figure 4.1**). However, 2DIR reveals fluctuation dynamics that decrease more than 50 fold (~10 ps to < 0.2 ps) across this density range. This largely results from the strongly inhomogeneous character of this rovibrational system and is another illustration of the power of 2DIR spectroscopy to uncover dynamics completely hidden in absorption spectra and this nonlinear approach will be widely applicable to other dense fluid systems.

In addition to establishing free rotor character in these dense fluids, the 2DIR analysis (CLS determined τ_c) provides an experimental estimate for coexisting liquid-like character. This component, contributing to intensity in the gas-phase forbidden *Q*-branch region of the linear absorption spectrum, increases with density. Thus, in these dense gas and supercritical SF_6 solutions, 2DIR experiments are consistent with the description that N_2O has simultaneous free rotor and hindered rotor subpopulations, and this heterogeneity results, in part, from the distribution of rotational energies relative to the density dependent N_2O-SF_6 potential barriers heights. As the density increases, the average effective barrier heights increase and a larger portion of the entire ensemble has

insufficient rotational energy to exceed these barrier energies. Subsequent isobaric temperature studies for a number of pressures and simulations will be carried out to develop more quantitative description of the heuristic barrier model (Eq. 4.9).

This growing intensity in the nominally forbidden gas phase *Q*-branch region is phenomenologically analogous to the triplet structure previously observed in the numerous studies of the absorption spectra of hydrogen halides in nonpolar liquids.[138, 169-185] 2DIR studies of these diatomics in these dense nonpolar fluids can also establish the free rotor character in these diatomic probe systems and their state point dependence. MD simulations and calculations have been carried out to understand the origins of these absorption spectra and what they reveal about solvation in the liquid and high-pressure environments. Re-examining these systems with the quantitative fluctuation dynamics provided by 2DIR measurements would provide a better understanding of this long studied phenomenon and the gas to liquid solvation transition in these systems (and others).

An advantage of 2DIR relative to some other time domain techniques is that CLS decays directly report on bath fluctuation dynamics, at least as they couple to the reporting probe molecule's (ro)vibrational energy. A modest slowing of the fluctuation dynamics appears in SF_6's critical point region. This observation is analogous to the faster vibrational lifetimes found for $W(CO)_6$ in SCF solutions at densities near the critical point region.[157-159] However, in 2DIR, as shown here, such critical *slowing* effects are directly observed in contrast to being inferred from T_1 effects. 2DIR measurements in

our lab are ongoing to map this critical slowing effect with greater precision in the N_2O-SF_6 system.

As these results demonstrate, 2DIR can establish the relative amounts of gas or liquid like character at all phase points in the supercritical region when the corresponding absorption character is devoid of any rotational structure. In contrast to previous studies[162-168] which have generally relied on simulation results to test the concept of Frenkel or Widom lines to demarcate regions in the supercritical region with dominate liquid or gas like structure, 2DIR can be an effective experimental tool for this purpose and test the validity of these concepts in the SCF region in general. In another potential application, 2DIR can be used to study the dynamics of small molecules photoproducts in dense fluids (gas, supercritical and liquid) as these excited fragments return to equilibrium even when rotational features are not resolved. For example, a transient absorption study of the rotational cooling of hot CN resulting from BrCN photodissociation in perfluorohexane was recently reported.[142] The rovibrational band of this diatomic showed no rotational resolution and thus the analysis of the cooling of this degree of freedom relied on best fit modeling results including both free-rotor (*P, R*) and hinder rotor (*Q*-branch) contributions. 2DIR spectroscopy has the capacity to quantitatively provide measurements or rotational relaxation for such systems as shown here.

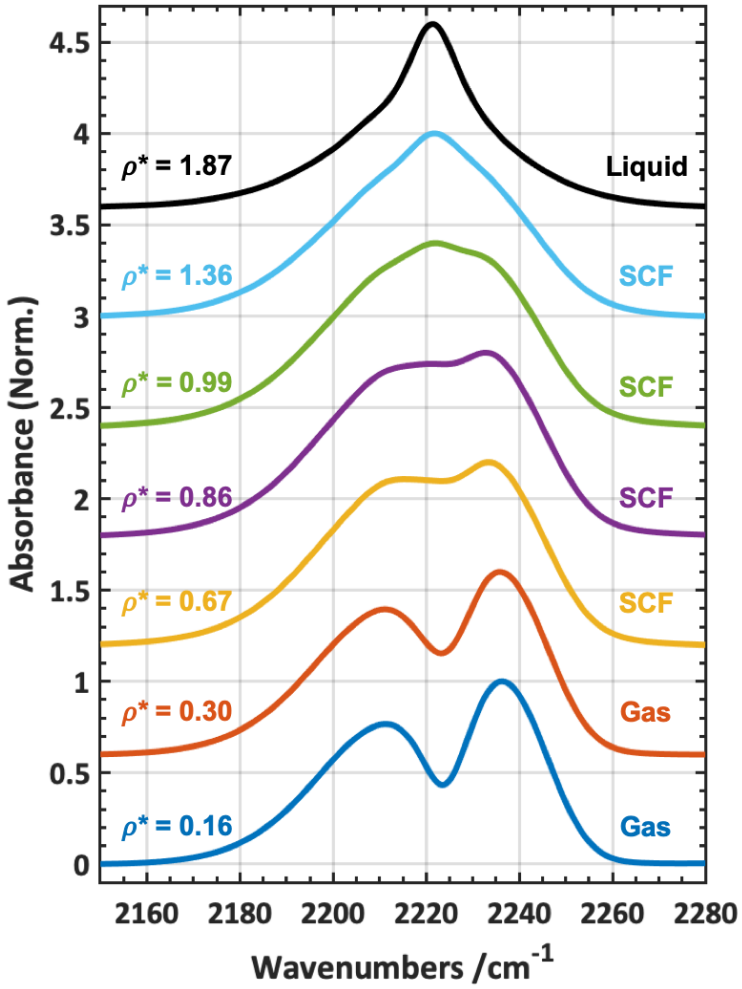

Figure 4.1 - Normalized absorption spectra of the N_2O ν_3 asymmetric stretch mode in SF_6 at densities ranging from gas to liquid through the supercritical fluid (SCF) regime ($\rho^* = \rho/\rho_c$). Pressures and temperatures corresponding to these state points are given in the text.

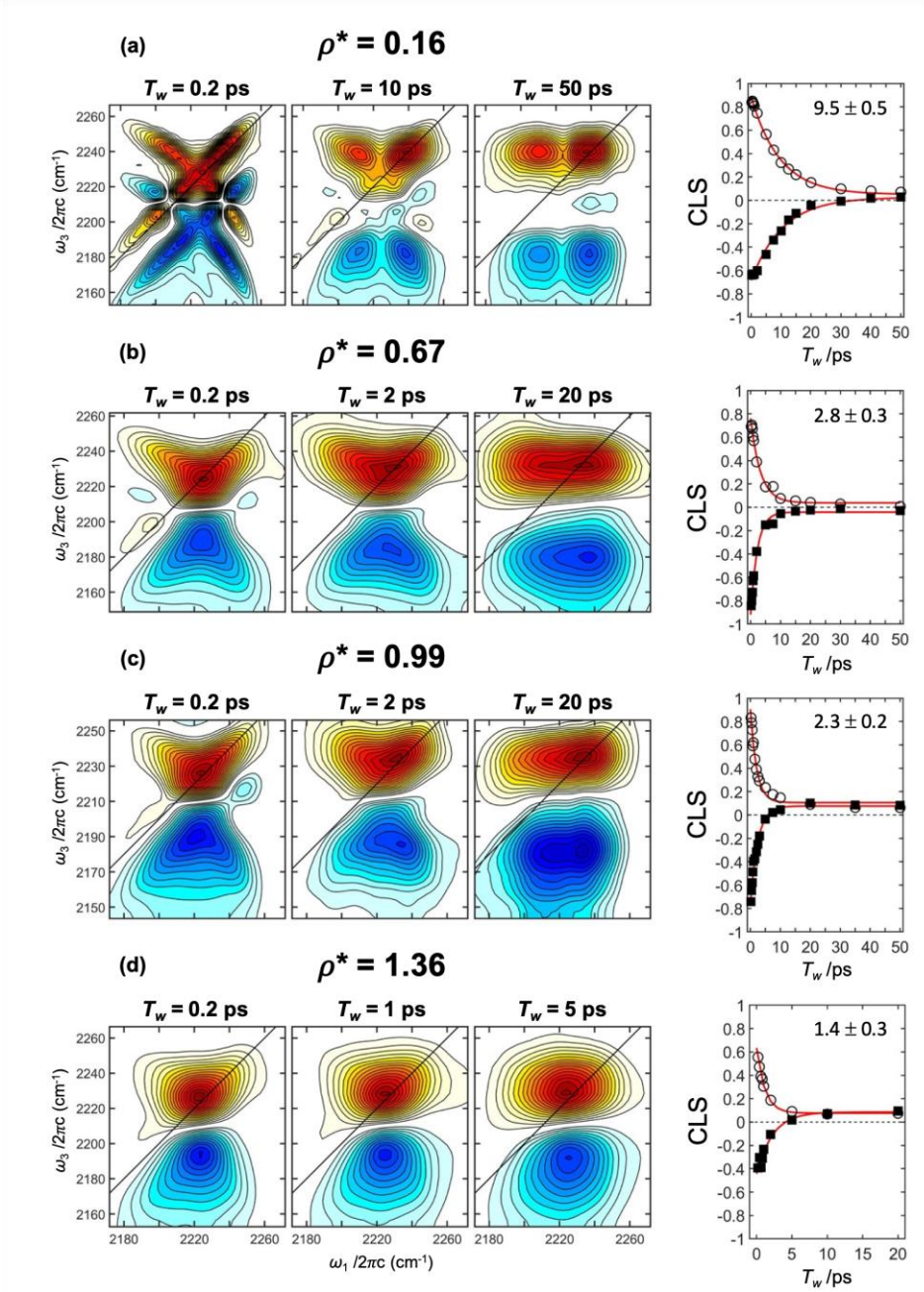

Figure 4.2 - 2DIR spectra of N_2O ν_3 in SF_6 at three representative waiting times (T_w) for the non-liquid state points corresponding to (a) $\rho^* = 0.16$[6], (b) $\rho^* = 0.67$, (c) $\rho^* = 0.99$, and (d) $\rho^* = 1.36$ SF_6 densities and corresponding CLS decays are shown. Red contours denote positive-going GSB-SE signals and blue contours denote negative-going ESA signals. See Ref. 6 for $\rho^* = 0.30$ and SI for $\rho^* = 0.86$ corresponding 2DIR spectra.

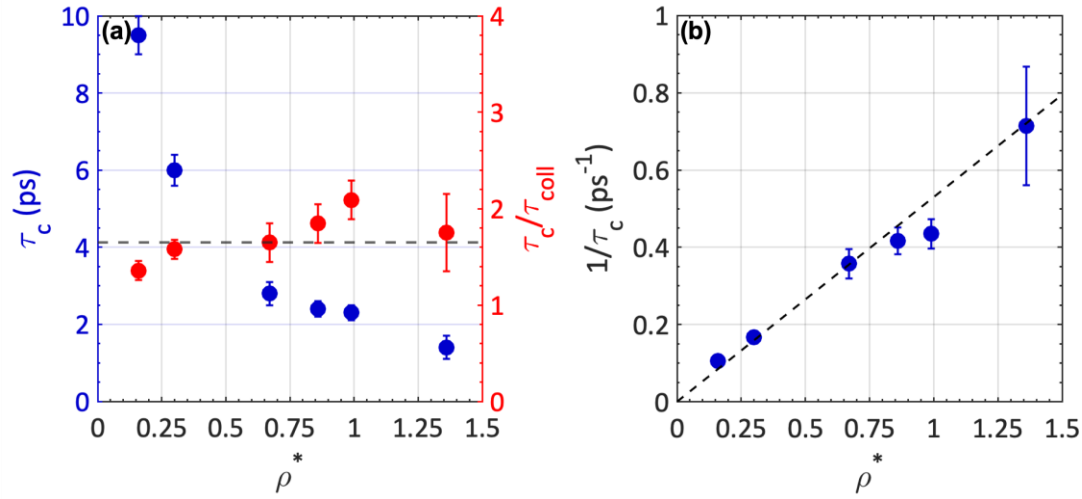

Figure 4.3 - (a) The observed CLS decay time (τ_c) at each gas and supercritical ρ^* in ps are the blue data points (LHS scale. This same rotational energy relaxation time is given in terms of mean free time between hard-sphere collisions, $Z_{rot} = \tau_c/\tau_{coll}$ (RHS scale, red points). (b) A plot of ν_3 rotational energy fluctuation rate, $1/\tau_c$, as a function of ρ^*.

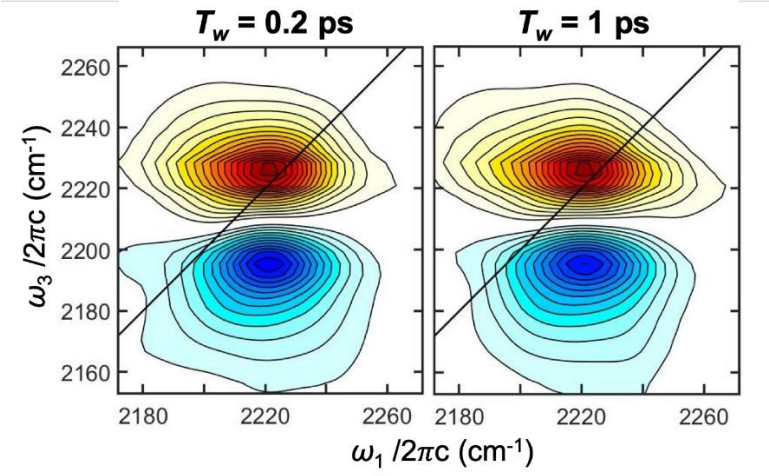

Figure 4.4 – 2DIR spectrum of the N_2O ν_3 asymmetric stretch in liquid SF_6 (ρ^* = 1.87). No anti-diagonal features are observed and no CLS decay is detected indicating τ_c << 200 fs.

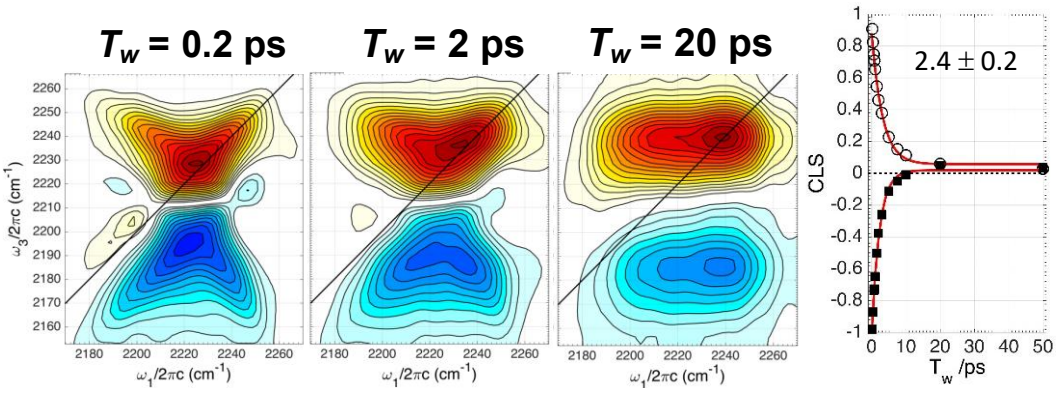

Figure 4.5 - 2DIR spectra and corresponding CLS decays of N_2O □$_3$ in SF_6 at ρ^* = 0.86. Red contours denote positive-going GSB-SE signals and blue contours denote negative-going ESA signals.

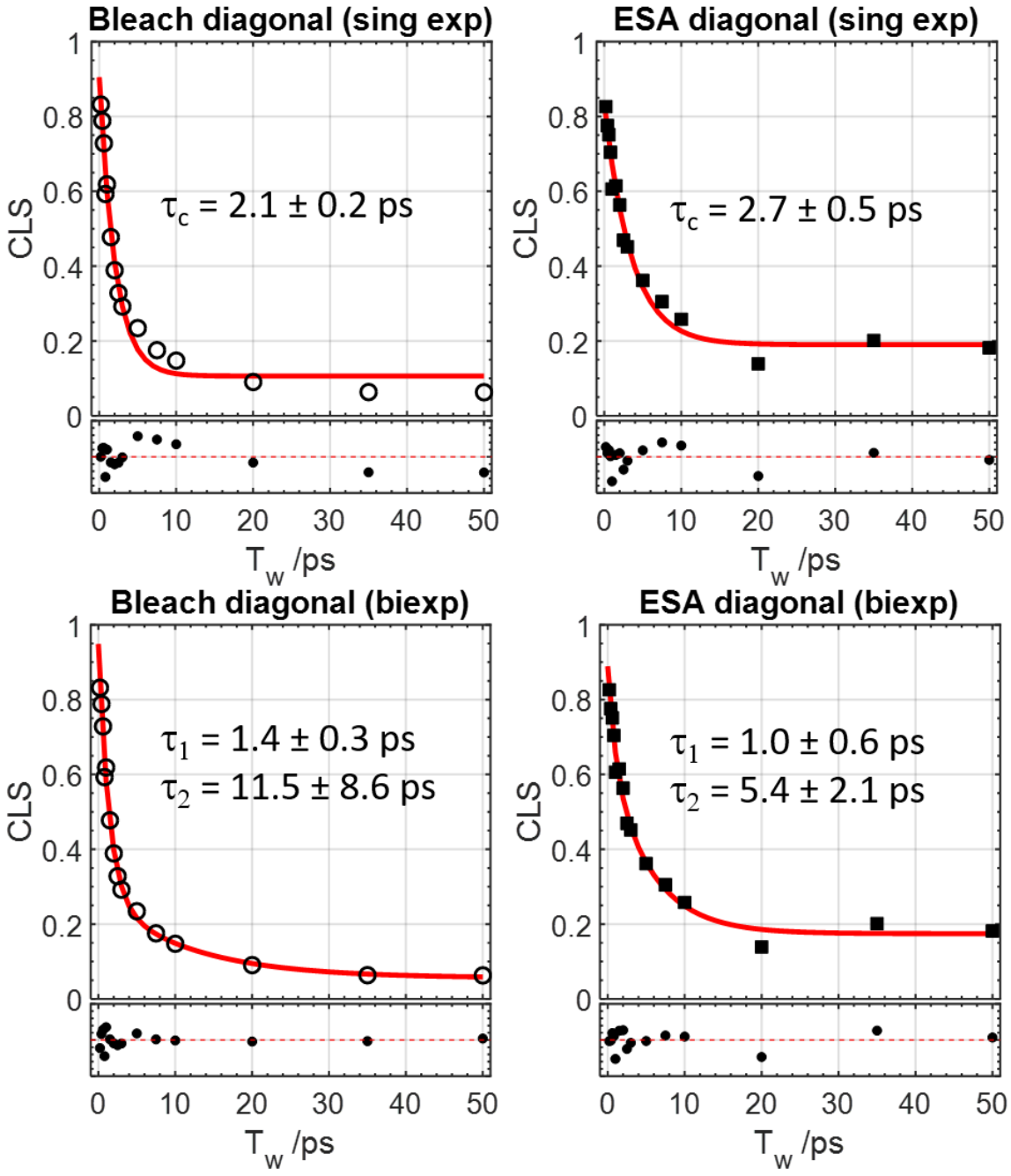

Figure 4.5 – CLS Decays for ρ* ~ 1 for the GSB and ESA diagonal peaks. The CLS decays are fit to both a single exponential and a double exponential to show the accuracy in fitting and timescales determined from each method.

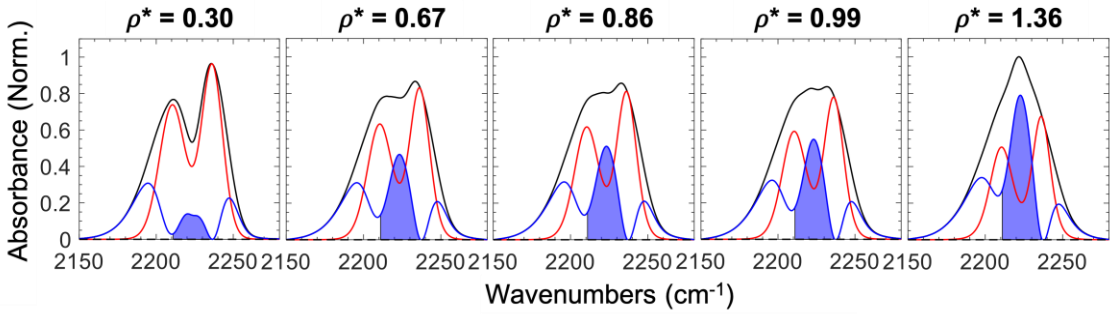

Figure 4.6 - Normalized difference spectra (blue trace) between calculated gas-phase spectra (red trace) and experimental FTIR spectra (black trace). The blue highlighted region of this difference spectrum spans 2211-2236 cm^{-1} and represents the growth of liquid-like vibrational transition character in the forbidden "*Q*-branch" region as SF_6 density increases. Absorption spectra are calculated using the low pressure D_{10}^{P}, D_{10}^{R} widths and the fluctuation times, τ_c, obtained from the 2DIR. (See Ref. 6 for more details.)

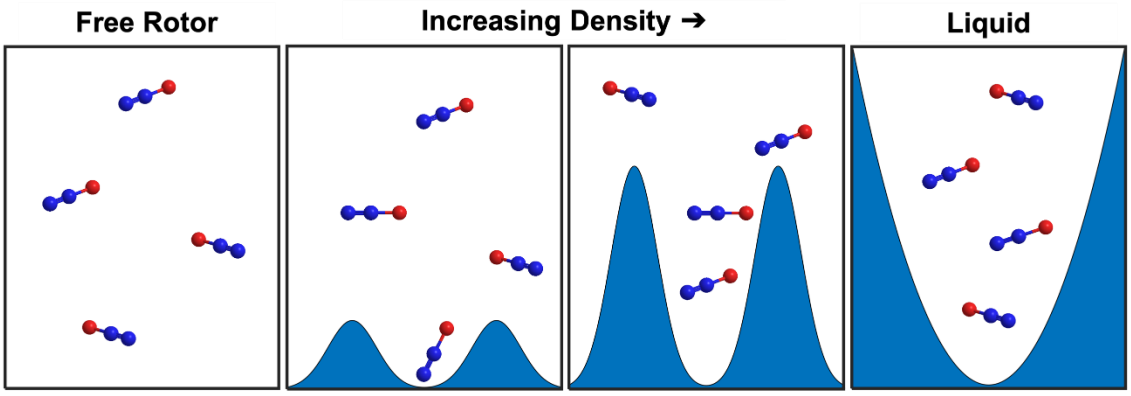

Figure 4.7 - Illustrative representation of the rotational potential barrier due to rotor-bath interactions as a function of solvent/bath density

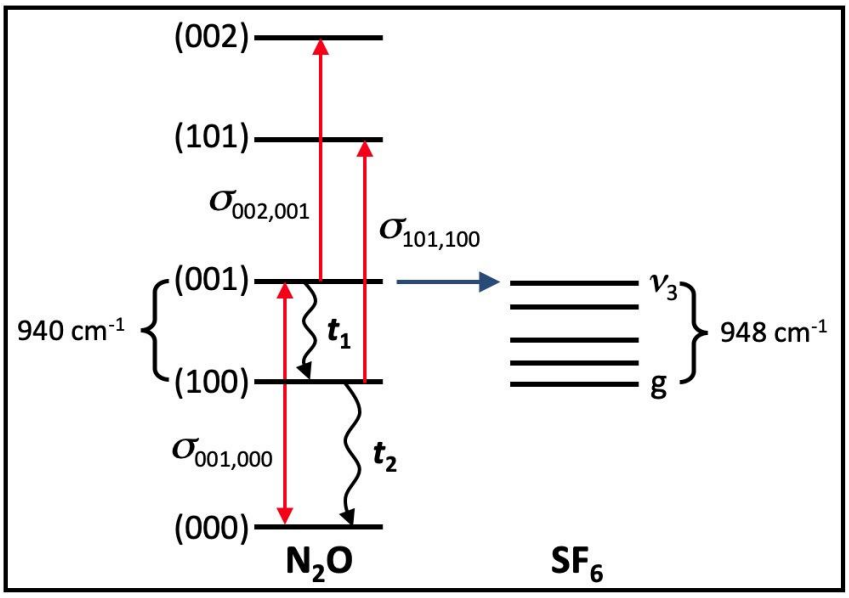

Figure 4.8 – N_2O and SF_6 vibrational energy level diagram that summarizes the kinetic model used to best-fit the N_2O ν_3 pump-probe *ΔOD(t)* response.

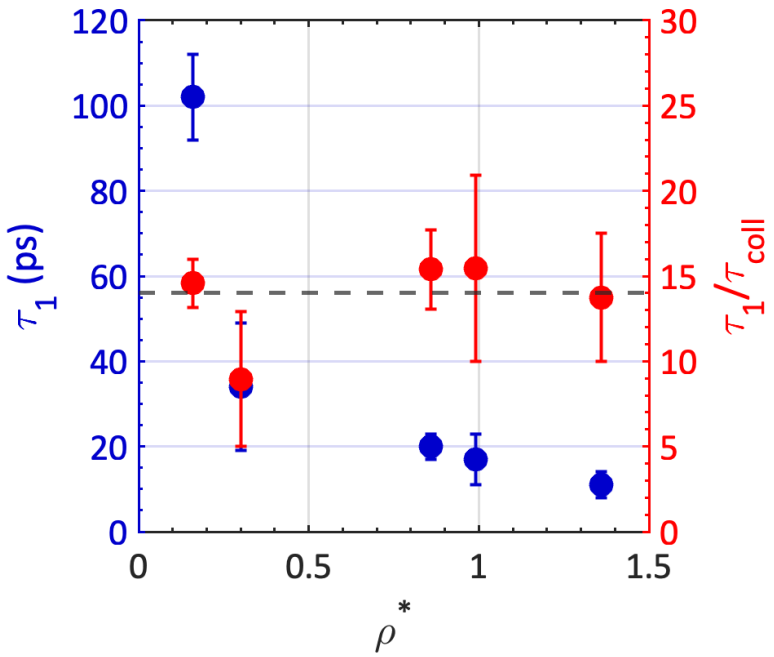

Figure 4.9 - Plot of N_2O ν_3 lifetime (τ_1) in ps (LHS scale, blue points) and in terms of number of bath collisions, τ_1/τ_{coll}, (RHS scale, red points) as a function of SF_6 reduced density.

Table 4.1. Rotational equilibration times determined by 2DIR CLS decay times (τ_c) and number of collisions ($Z_{rot} = \tau_c/\tau_{coll}$) as a function of SF_6 reduced densities in the gas and supercritical phases.

SF_6 density[a]	**τ_c /ps[b]**	**τ_{coll} /ps**	**$Z_{rot} = \tau_c/\tau_{coll}$**
$\rho^* = 0.16$[91]	9.5 ± 0.5	7.0	1.4
$\rho^* = 0.30$[91]	6.0 ± 0.4	3.8	1.6
$\rho^* = 0.67$	2.8 ± 0.3	1.7	1.6
$\rho^* = 0.86$	2.4 ± 0.2	1.3	1.8
$\rho^* = 0.99$	2.3 ± 0.2	1.1	2.0
$\rho^* = 1.36$	1.4 ± 0.3	0.8	1.8

[a]Density given in reduced density units relative to SF_6 critical point density: $\rho^* = \rho/\rho_c$
[b]Average of diagonal and antidiagonal CLS decay constants.

Table 4.2. N_2O ν_3 VER kinetics determined by fits to a bi-exponential fit to ΔOD responses.*

	$\rho^* = 0.16$[91]	**$\rho^* = 0.30$[91]**	**$\rho^* = 0.86$**	**$\rho^* = 0.99$**	**$\rho^* = 1.36$**	**$\rho^* = 1.87$**
C_1/C_2	2.0	1.9	1.8	1.8	1.8	1.8
τ_1 /ps	102 ± 10	34 ± 15	20 ± 3	17 ± 6	11 ± 3	6 ± 1
τ_2 /ps	≫1000	>1000	590 ± 130	>1000	490 ± 80	200 ± 20

*Precision estimates given by determining the limits of the two lifetimes, τ_1 and τ_2, for which the sum of squared residuals (SSR) are ≤ 1.5× that of the best fit, such that a systematic distribution of residuals was not observed.

References

(1) Helbing, J.; Hamm, P., Compact implementation of Fourier transform two-dimensional IR spectroscopy without phase ambiguity. *Journal of the Optical Society of America B* **2010,** *28* (1), 171.

(2) Shattuck, J.; Shah, P.; Erramilli, S.; Ziegler, L. D., Structure Making and Breaking Effects of Cations in Aqueous Solution: Nitrous Oxide Pump–Probe Measurements. *The Journal of Physical Chemistry B* **2016,** *120* (40), 10569-10580.

(3) Wiggins, P. M., Role of water in some biological processes. *Microbiological Reviews* **1990,** *54*, 432-449.

(4) Hofmesiter, F., Zur Lehre von der wirkung der salze. *Naunyn-Schmiedeberg's Archives of Pharmacology* **1888,** *24*, 247-260.

(5) Cacace, M. G.; Landau, E. M.; Ramsden, J. J., The Hofmeister series: salt and solvent effects on interfacial phenomena. *Quarterly Reviews of Biophysics* **1997,** *30* (3), 241-277.

(6) Collins, K. D., Ions from the Hofmeister series and osmolytes: effects on proteins in solution and in the crystallization process. *Methods* **2004,** *34* (3), 300-11.

(7) Collins, K., Washabaugh, M., The Hofmeister effect and the behaviour of water at interfaces. *Quarterly Reviews of Biophysics* **1985,** *18* (4), 323-422.

(8) Marcus, Y., *Ion solvation*. Wiley: Chichester, U.K., 1985.

(9) Marcus, Y., Effect of Ions on the Structure of Water: Structure Making and Breaking. *Chemical Reviews* **2009,** *109*, 1346-1370.

(10) Gurney, R. W., *Ionic Process in Solution*. McGraw-Hill: New York, 1953.

(11) K. Buijs, G. R. C., Near-Infrared Studies of the Structure of Water. II. Ionic Solutions. *The Journal of Chemical Physics* **1963,** *39* (8), 2042-2050.

(12) Lyubartsev, A. P.; Laasonen, K.; Laaksonen, A., Hydration of Li+ ion. An ab initio molecular dynamics simulation. *The Journal of Chemical Physics* **2001,** *114* (7), 3120-3126.

(13) Millero, F. J., Molal volumes of electrolytes. *Chemical Reviews* **1971,** *71*, 147-176.

(14) Jenkins, H. D. B. M., Y., Viscosity B-coefficients of ions in solution. *Chemical Reviews* **1995,** *95*, 2695-2724.

(15) Marcus, Y., Viscosity B-coefficients, structural entropies and heat capacities, and the effects of ions on the structure of water. *Journal of Solution Chemistry* **1994,** *23* (7), 831-848.

(16) Henry S. Frank, M. W. E., Free Volume and Entropy in Condensed Systems III. Entropy in Binary Liquid Mixtures; Partial Molal Entropy in Dilute Solutions; Structure and Thermodynamics in Aqueous Electrolytes. *The Journal of Chemical Physics* **1945,** *13* (11), 507-532.

(17) Chaplin, M. Water structure and science. http://www1.lsbu.ac.uk/water/hofmeister_series.html.

(18) Ben-Naim, A., Structure-breaking and structure-promoting processes in aqueous solutions. *Journal of Physical Chemistry* **1975,** *79*, 1268-1274.

(19) Tielrooij, K. J.; van der Post, S. T.; Hunger, J.; Bonn, M.; Bakker, H. J., Anisotropic water reorientation around ions. *The Journal of Physical Chemistry B* **2011,** *115* (43), 12638-47.

(20) Bakker, H. J., Structural dynamics of aqueous salt solutions. *Chemical Reviews* **2008,** *108*, 1456-1473.

(21) Zhang, Y.; Cremer, P. S., Interactions between macromolecules and ions: The Hofmeister series.*Current Opinion in Chemical Biology* **2006,** *10* (6), 658-63.

(22) Tobias, D. J. H., J. C., Getting Specific About Specific Ion Effects. *Science* **2008,** *319*, 1197-1198.

(23) Tielrooij, K. J. G.-A., N.; Bonn, M.; Bakker, H. J., Cooperativity in Ion Hydration. *Science* **2010,** *328*, 1006-1009.

(24) Sacco, A. W., H.; Braun, B. M.; Holz, M., Study of the structure-breaking effect in aqueous CsCl solutions based on H2O/D2O isotope effects on transport coefficients and microdynamical properties. *Journal of the Chemical Society* **1994,** *90*, 849-853.

(25) Ohtaki, H. R., T., Structure and dynamics of hydrated ions. *Chemical Reviews* **1993,** *93*, 1157-1204.

(26) G. Engel, H. G. H., On the Negative Hydration. A Nuclear Magnetic Relaxation Study. *Berichte der Bunsengesellschaft für physikalische Chemie* **1968,** *72* (7), 808-834.

(27) Bouazizi, S. N., S.; Jaîdane, N.; Bellissent-Funel, M.-C., Local order in aqueous NaCl solutions and pure water: X-ray scattering and molecular dynamics simulations study. *Journal of Physical Chemistry B* **2006,** *110*, 23515-23523.

(28) Ildiko Harsanyi, P. J., Gy. Mészáros, Laszlo Pusztai, Philippe A. Bopp, Neutron and X-ray diffraction studies of aqueous rubidium bromide solutions. *Journal of Molecular Liquids* **2007,** *131-132*, 60-64.

(29) Badyal, Y. S. B., A. C.; Cuello, G. J.; Simonson, J. M., Understanding the effects of concentration on the solvation structure of Ca2+ in aqueous solution. II: Insights into longer range order from neutron diffraction isotope substitution. *Journal Of Physical Chemistry A* **2004,** *108*, 11819-11827.

(30) Soper, A. K.; Weckstrom, K., Ion solvation and water structure in potassium halide aqueous solutions. *Biophysical Chemistry* **2006,** *124* (3), 180-91.

(31) Mancinelli, R.; Botti, A.; Bruni, F.; Ricci, M. A.; Soper, A. K., Perturbation of water structure due to monovalent ions in solution. *Physical Chemistry Chemical Physics* **2007,** *9* (23), 2959-67.

(32) David A. Turton, J. H., Glenn Hefter, Richard Buchner, Klaas Wynne, Glasslike behavior in aqueous electrolyte solutions. *The Journal of Chemical Physics* **2008,** *128* (16), 161102.

(33) Foggi, P. B., M.; Kien, D. P.; Vercuque, I.; Righini, R., Relaxation dynamics of water and HCl aqueous solutions measured by time-resolved optical kerr effect. *Journal of Physical Chemistry A* **1997,** *101*, 7029-7035.

(34) Walrafen, G. E., Raman Spectral Studies of Water Structure. *The Journal of Chemical Physics* **1964,** *40* (11), 3249-3256.

(35) Walrafen, G. E., Raman spectral studies of the effects of electrolytes on water. *The Journal of Chemical Physics* **1962,** *36* (4), 1035-1042.

(36) Wachter, W. K., W.; Buchner, R.; Hefter, G., Is there an anionic Hofmeister effect on water dynamics? Dielectric spectroscopy of aqueous solutions of NaBr, NaI, NaNO3, NaClO4, and NaSCN. *Journal of Physical Chemistry A* **2005,** *109*, 8675-8683.

(37) Kumar, R.; Keyes, T., Classical simulations with the POLIR potential describe the vibrational spectroscopy and energetics of hydration: divalent cations, from solvation to coordination complex. *The Journal of the American Chemical Society* **2011,** *133* (24), 9441-50.

(38) Laage, D.; Hynes, J. T., Reorientional dynamics of water molecules in anionic hydration shells. *Proceedings of the National Academy of Sciences of the United States of America* **2007,** *104* (27), 11167-72.

(39) Lin, Y. S.; Auer, B. M.; Skinner, J. L., Water structure, dynamics, and vibrational spectroscopy in sodium bromide solutions. *The Journal of Chemical Physics* **2009,** *131* (14), 144511.

(40) Lightstone, F. C. S., E.; Hood, R. Q.; Gygi, F.; Galli, G., A first principles molecular dynamics simulation of the hydrated magnesium ion. *Chemical Physics Letters* **2001,** *343*, 549-555.

(41) Istvan Mayer, I. L., T. Radnai, Hydration of cations: H-bond shortening as an electrostatic effect. *Chemical Physics Letters* **1992,** *188* (5-6), 595-598.

(42) Tongraar, A. L., K. R.; Rode, B. M., Born−Oppenheimer ab Initio QM/MM dynamics simulations of Na+ and K+ in water: From structure making to structure breaking effects. *Journal of Physical Chemistry A 102*, 10340-10347.

(43) Sheng-Bai Zhu, G. W. R., Molecular-dynamics computer simulation of an aqueous NaCl solution: Structure. *The Journal of Chemical Physics* **1992,** *97* (6), 4336-4348.

(44) Bernal-Uruchurtu, M. I. O.-B., I., A refined Monte Carlo study of Mg^{2+} and Ca^{2+} hydration. *Journal of Physical Chemistry* **1995,** *103*, 1588-1598.

(45) Omta, A. W. K., M. F.; Woutersen, S.; Bakker, H. J., Negligible Effect of Ions on the Hydrogen-Bond Structure in Liquid Water. *Science* **2003,** *301*, 347-349.

(46) Omta, A. W. K., M. F.; Woutersen S.; Bakker, H. J. , Influence of ions on the hydrogen-bond structure in liquid water. *The Journal of Chemical Physics* **2003,** *119* (23), 12457-12461.

(47) Bakker, H. J.; Kropman, M. F.; Omta, A. W., Effect of ions on the structure and dynamics of liquid water. *Journal of Physics: Condensed Matter* **2005,** *17* (45), S3215-S3224.

(48) Kropman, M. F. B., H. J, Vibrational relaxation of liquid water in ionic solvation shells. *Chemical Physics Letters* **2003,** *370* (5-6), 741-746.

(49) Janusz Stangret, T. G., Ionic Hydration Behavior Derived from Infrared Spectra in HDO. *Journal of Physical Chemistry* **2002,** *106*, 5393-5402.

(50) Piatkowski, L.; Bakker, H. J., Vibrational dynamics of the bending mode of water interacting with ions. *The Journal of Chemical Physics* **2011,** *135* (21), 214509.

(51) Mobley, D. L.; Baker, J. R.; Barber, A. E., 2nd; Fennell, C. J.; Dill, K. A., Charge asymmetries in hydration of polar solutes. *The Journal of Physical Chemistry B* **2008,** *112* (8), 2405-14.

(52) Kropman, M. F. B., H. J., Effect of Ions on the Vibrational Relaxation of Liquid Water. *The Journal of the American Chemical Society* **2004,** *126*, 9135-9141.

(53) Giammanco, C. H.; Wong, D. B.; Fayer, M. D., Water dynamics in divalent and monovalent concentrated salt solutions. *The Journal of Physical Chemistry B* **2012,** *116* (46), 13781-92.

(54) Park, S.; Fayer, M. D., Hydrogen bond dynamics in aqueous NaBr solutions. *Proceedings of the National Academy of Sciences of the United States of America* **2007,** *104* (43), 16731-8.

(55) Kropman, M. F.; Nienhuys, H. K.; Bakker, H. J., Real-time measurement of the orientational dynamics of aqueous solvation shells in bulk liquid water. *Physical Review Letters* **2002,** *88* (7), 077601.

(56) van der Post, S. T.; Bakker, H. J., The combined effect of cations and anions on the dynamics of water. *Physical Chemistry Chemical Physics* **2012,** *14* (18), 6280-8.

(57) Bian, H.; Chen, H.; Zhang, Q.; Li, J.; Wen, X.; Zhuang, W.; Zheng, J., Cation effects on rotational dynamics of anions and water molecules in alkali (Li+, Na+, K+, Cs+) thiocyanate (SCN-) aqueous solutions. *The Journal of Physical Chemistry B* **2013,** *117* (26), 7972-84.

(58) van der Vegt, N. F.; Haldrup, K.; Roke, S.; Zheng, J.; Lund, M.; Bakker, H. J., Water-Mediated Ion Pairing: Occurrence and Relevance. *Chemical Reviews* **2016,** *116* (13), 7626-41.

(59) Shulman, R. G. D., B. P.; Townes, C. H., Molecular dipole moments and stark effects. III. Dipole moment determinations. *Physical Review* **1950,** *72* (2), 145-148.

(60) Shattuck, J. T.; Schneck, J. R.; Chieffo, L. R.; Erramilli, S.; Ziegler, L. D., Dispersed three-pulse infrared photon echoes of nitrous oxide in water and octanol. *The Journal of Physical Chemistry B* **2013,** *117* (49), 15774-85.

(61) Chieffo, L.; Shattuck, J.; Amsden, J. J.; Erramilli, S.; Ziegler, L. D., Ultrafast vibrational relaxation of liquid H2O following librational combination band excitation. *Chemical Physics* **2007,** *341* (1-3), 71-80.

(62) Walrafen, G. E. B., L. A, Weak Raman bands from water. *The Journal of Chemical Physics* **1973,** *59* (5), 2646-2650.

(63) Chieffo, L. R.; Shattuck, J. T.; Pinnick, E.; Amsden, J. J.; Hong, M. K.; Wang, F.; Erramilli, S.; Ziegler, L. D., Nitrous oxide vibrational energy relaxation is a probe of interfacial water in lipid bilayers. *The Journal of Physical Chemistry B* **2008,** *112* (40), 12776-82.

(64) Walrafen, G. E., Raman Spectral Studies of the Effects of Temperature on Water and Electrolyte Solutions. *The Journal of Chemical Physics* **1966,** *44* (4), 1546-1558.

(65) Li, R. J., Z.; Chen, F.; Yang, H.; Guan, Y., Hydrogen bonded structure of water and aqueous solutions of sodium halides: a Raman spectroscopic study. *Journal of Molecular Structure* **2004,** *707*, 83-88.

(66) Mahler, J.; Persson, I., A study of the hydration of the alkali metal ions in aqueous solution. *Inorganic Chemistry* **2012,** *51* (1), 425-38.

(67) Martí, J., Analysis of the hydrogen bonding and vibrational spectra of supercritical model water by molecular dynamics simulations. *The Journal of Chemical Physics* **1999,** *110*, 6876-6886.

(68) Chandra, A., Effects of ion atmosphere on hydrogen-bond dynamics in aqueous electrolyte solutions. *Physical Review Letters* **2000,** *85* (4), 768-771.

(69) Guardia, E. L., D.; Martí, J., Hydrogen bond structure and dynamics in aqueous electrolytes at ambient and supercritical conditions. *Journal of Physical Chemistry B 110*, 6332-6338.

(70) Concentrative properties of aqueous solutions: Density, refractive index, freezing point depression, and viscosity. http://chemistry.mdma.ch/hiveboard/rhodium/pdf/chemical-data/prop_aq.pdf (accessed September 21).

(71) Novotny, O. S. u. P., *Densities of Aqueous Solutions of Inorganic Substances*. Elsevier: Amsterdam, 1985.

(72) Tan, H.-S. P., I. R.; Fayer, M. D., Polarization selective spectroscopy experiments: methodology and pitfalls. *Journal of the Optical Society of America B* **2005,** *22*, 2009-2017.

(73) Fayer, M. D.; Moilanen, D. E.; Wong, D.; Rosenfeld, D. E.; Fenn, E. E.; park, S., Water Dynamics in Salt Solutions Studied with Ultrafast Two-Dimensional Infrared (2D IR) Vibrational Echo Spectroscopy. *Accounts of Chemical Research* **2009,** *42* (9), 1210-1219.

(74) Ganz, E., Über das Absorptionsspektrum von flüssigem Wasser zwischen 2,5µ und 6,5µber das Absorptionsspektrum von flüssigem Wasserzwischen 2,5µ und 6,5µ. *Annalen der Physik* **1937,** *420* (5), 445-457.

(75) Williams, D. M., W., The effects of various ions on the infrared absorption of water. *Physical Review* **1944,** *66*, 6-8.

(76) Max, J.-J.; Blois, S. d.; Veilleux, A.; Chapados, C., IR Spectroscopy of aqueous alkali halides. Factor analysis. *Canadian Journal of Chemistry* **2001,** *79* (1), 13-21.

(77) Huse, N.; Ashihara, S.; Nibbering, E. T. J.; Elsaesser, T., Ultrafast vibrational relaxation of O–H bending and librational excitations in liquid H2O. *Chemical Physics Letters* **2005,** *404* (4-6), 389-393.

(78) Moskovits, M. M., K. H., A reinvestigation of the Raman spectrum of water. *The Journal of Chemical Physics* **1978,** *69* (6), 2306-2311.

(79) Walrafen, G. E. H., M. S.; Yang, W. H., Raman investigation of the temperature dependence of the bending ν2 and combination ν2 + νL bands from liquid water. *Journal of Physical Chemistry* **1988,** *92*, 2433-2438.

(80) Oxtoby, D. W., Vibrational population relaxation in liquids. *Advances in Chemical Physics* **1981,** *47*, 487-519.

(81) Owrutsky, J. C. R., D.; Hochstrasser, R. M., Vibrational relaxation dynamics in solutions. *Annual Review of Physical Chemistry* **1994,** *45*, 519-555.

(82) Aubuchon, C. M. R., K. D.; Holmes, W.; Fayer, M. D., Nitro group asymmetric stretching mode lifetimes of molecules used in energetic materials. *Chemical Physics Letters* **1999,** *299*, 84-90.

(83) Kenkre, V. M. T., A.; Fayer, M. D., Theory of vibrational relaxation of polyatomic molecules in liquids. *The Journal of Chemical Physics* **1994,** *101*, 10618-10629.

(84) Moore, P.; Tokmakoff, A.; Keyes, T.; Fayer, M. D., The low frequency density of states and vibrational population dynamics of polyatomic molecules in liquids. *The Journal of Chemical Physics* **1995,** *103* (9), 3325-3334.

(85) Laage, D.; Hynes, J. T., Do more strongly hydrogen-bonded water molecules reorient more slowly ? *Chemical Physics Letters* **2006,** *433* (1-3), 80-85.

(86) Nigro, B. R., S.; Laage, D.; Rey, R.; Hynes, J. T., On the ultrafast infrared spectroscopy of anion hydration shell hydrogen bond dynamics. *Journal of Physical Chemistry A* **2009,** *110*, 11237-11243.

(87) Millero, F. J., Molal volumes of electrolytes. *Chemical Reviews* **1971,** *71* (2), 147-176.

(88) Jenkins, H. D. B.; Marcus, Y., Viscosity B-Coefficients of Ions in Solution. *Chemical Reviews* **1995,** *95* (8), 2695-2724.

(89) Marcus, Y., Effect of Ions on the Structure of Water: Structure Making and Breaking. *Chemical Reviews* **2009,** *109* (3), 1346-1370.

(90) Chaplin, M., Water Structure and Science, http://www1.lsbu.ac.uk/water/hofmeister_series.html#prop.

(91) Mandal, A.; Ng Pack, G.; Shah, P. P.; Erramilli, S.; Ziegler, L. D., Ultrafast Two-Dimensional Infrared Spectroscopy of a Quasifree Rotor: *J* Scrambling and Perfectly Anticorrelated Cross Peaks. *Physical Review Letters* **2018,** *120* (10), 103401.

(92) Hamm, P.; Zanni, M., *Concepts and methods of 2D infrared spectroscopy*. Cambridge University Press: 2011.

(93) Cho, M., Coherent two-dimensional optical spectroscopy. *Chemical reviews* **2008,** *108* (4), 1331-1418.

(94) Fayer, M. D.; Moilanen, D. E.; Wong, D.; Rosenfeld, D. E.; Fenn, E. E.; Park, S., Water Dynamics in Salt Solutions Studied with Ultrafast 2D IR Vibrational Echo Spectroscopy. *Accounts of Chemical Research* **2009,** *42* (9), 1210.

(95) Roberts, S. T.; Ramasesha, K.; Tokmakoff, A., Structural Rearrangements in Water Viewed Through Two-Dimensional Infrared Spectroscopy. *Accounts of Chemical Research* **2009,** *42* (9), 1239-1249.

(96) Ramasesha, K.; De Marco, L.; Mandal, A.; Tokmakoff, A., Water vibrations have strongly mixed intra-and intermolecular character. *Nature Chemistry* **2013,** *5* (11), 935-940.

(97) Mandal, A.; Ramasesha, K.; De Marco, L.; Tokmakoff, A., Collective vibrations of water-solvated hydroxide ions investigated with broadband 2DIR spectroscopy. *The Journal of Chemical Physics* **2014,** *140* (20), 204508.

(98) Thämer, M.; De Marco, L.; Ramasesha, K.; Mandal, A.; Tokmakoff, A., Ultrafast 2D IR spectroscopy of the excess proton in liquid water. *Science* **2015,** *350* (6256), 78-82.

(99) Mandal, A.; Tokmakoff, A., Vibrational dynamics of aqueous hydroxide solutions probed using broadband 2DIR spectroscopy. *The Journal of Chemical Physics* **2015,** *143* (19), 194501.

(100) Elsaesser, T., Two-dimensional infrared spectroscopy of intermolecular hydrogen bonds in the condensed phase. *Accounts of Chemical Research* **2009,** *42* (9), 1220-1228.

(101) Fayer, M., Dynamics of liquids, molecules, and proteins measured with ultrafast 2D IR vibrational echo chemical exchange spectroscopy. *Annual Review of Physical Chemistry* **2009,** *60*, 21-38.

(102) Baiz, C. R.; McRobbie, P. L.; Anna, J. M.; Geva, E.; Kubarych, K. J., Two-dimensional infrared spectroscopy of metal carbonyls. *Accounts of Chemical Research* **2009,** *42* (9), 1395-1404.

(103) Zanni, M. T.; Hochstrasser, R. M., Two-dimensional infrared spectroscopy: a promising new method for the time resolution of structures. *Current Opinion in Structural Biology* **2001,** *11* (5), 516-522.

(104) Woutersen, S.; Hamm, P., Nonlinear two-dimensional vibrational spectroscopy of peptides. *Journal of Physics: Condensed Matter* **2002,** *14* (39), R1035.

(105) Ganim, Z.; Chung, H. S.; Smith, A. W.; DeFlores, L. P.; Jones, K. C.; Tokmakoff, A., Amide I two-dimensional infrared spectroscopy of proteins. *Accounts of Chemical Research* **2008,** *41* (3), 432-441.

(106) Peng, C. S.; Jones, K. C.; Tokmakoff, A., Anharmonic vibrational modes of nucleic acid bases revealed by 2D IR spectroscopy. *Journal of the American Chemical Society* **2011,** *133* (39), 15650-15660.

(107) Giammanco, C. H.; Kramer, P. L.; Yamada, S. A.; Nishida, J.; Tamimi, A.; Fayer, M. D., Carbon dioxide in an ionic liquid: Structural and rotational dynamics. *The Journal of Chemical Physics* **2016,** *144* (10), 104506.

(108) Perakis, F.; Widmer, S.; Hamm, P., Two-dimensional infrared spectroscopy of isotope-diluted ice Ih. *The Journal of Chemical Physics* **2011,** *134* (20), 204505.

(109) Kwak, K.; Park, S.; Finkelstein, I. J.; Fayer, M. D., Frequency-frequency correlation functions and apodization in two-dimensional infrared vibrational echo spectroscopy: a new approach. *The Journal of Chemical Physics* **2007,** *127* (12), 124503.

(110) Helbing, J.; Hamm, P., Compact implementation of Fourier transform two-dimensional IR spectroscopy without phase ambiguity. *Journal of the Optical Society of America B* **2011,** *28* (1), 171-178.

(111) Herzberg, G., *Infrared and Raman spectroscopy of Polyatomic Molecuoles*. Van Ostrand: 1954.

(112) G. Herzberg, L. H., Rotation-Vibration Spectra of Diatomic and Simple Polyatomic Molecules with Long Absorbing Paths VI. The Spectrum of Nitrous Oxide (N2O) below 1.2μ. *The Journal of Chemical Physics* **1950,** *18* (12), 1551-1561.

(113) Loparo, J. J.; Roberts, S. T.; Tokmakoff, A., Multidimensional infrared spectroscopy of water. I. Vibrational dynamics in two-dimensional IR line shapes. *The Journal of Chemical Physics* **2006,** *125* (19), 194521.

(114) Steinel, T.; Asbury, J. B.; Zheng, J.; Fayer, M. D., Watching Hydrogen Bonds Break: A Transient Absorption Study of Water. *Journal of Physical Chemistry A* **2004,** *108*, 10957-10964.

(115) Ghosh, A.; Remorino, A.; Tucker, M. J.; Hochstrasser, R. M., 2D IR photon echo spectroscopy reveals hydrogen bond dynamics of aromatic nitriles. *Chemical Physics Letters* **2009,** *469* (4-6), 325-330.

(116) Nydegger, M. W.; Dutta, S.; Cheatum, C. M., Two-dimensional infrared study of 3-azidopyridine as a potential spectroscopic reporter of protonation state. *The Journal of Chemical Physics* **2010,** *133* (13), 134506.

(117) Khalil, M.; Demirdöven, N.; Tokmakoff, A., Coherent 2D IR spectroscopy: Molecular structure and dynamics in solution. *The Journal of Physical Chemistry A* **2003,** *107* (27), 5258-5279.

(118) Nien-Hui Ge, M. T. Z., and Robin M. Hochstrasser, Effects of Vibrational Frequency Correlations on Two-Dimensional Infrared Spectra. *Journal of Physical Chemistry A* **2002,** *106*, 962-972.

(119) Chen, P. C., High Resolution Coherent 2D Spectroscopy. *Journal of Physical Chemistry A* **2010,** *114*, 11365-11375.

(120) Kwak, K.; Zheng, J.; Cang, H.; Fayer, M. D., Ultrafast Two-Dimensional Infrared Vibrational Echo Chemical Exchange Experiments and Theory. *The Journal of Physical Chemistry B* **2006,** *110* (40), 19998-20013.

(121) D. Lee, A. C. A., *Advances in infrared and Raman Spectroscopy*. John Wiley & Sons: New York, 1985.

(122) Khalil, M.; Tokmakoff, A., Signatures of vibrational interactions in coherent two-dimensional infrared spectroscopy. *Chemical Physics* **2001,** *266*, 213-230.

(123) Kwon, Y.; Lee, C.; Park, S., Effect of ion–molecule interaction on fermi-resonance in acetonitrile studied by ultrafast vibrational spectroscopy. *Chemical Physics* **2014,** *445*, 38-45.

(124) Ramasesha, K.; De Marco, L.; Horning, A. D.; Mandal, A.; Tokmakoff, A., A phenomenological approach to modeling chemical dynamics in nonlinear and two-dimensional spectroscopy. *The Journal of Chemical Physics* **2012,** *136* (13), 134507.

(125) Sung, J.; Silbey, R. J., Four wave mixing spectroscopy for a multilevel system. *The Journal of Chemical Physics* **2001,** *115*, 9266-9287.

(126) Mukamel, S., *Nonlinear Optical Spectroscopy*. Oxford University Press: Oxford, 1995.

(127) Kubo, R., *Advances in Chemical Physics*. John Wiley & Sons, Inc. : New York, 1969.

(128) Demirdöven, N.; Khalil, M.; Tokmakoff, A., Correlated vibrational dynamics revealed by two-dimensional infrared spectroscopy. *Physical Review Letters* **2002,** *89* (23), 237401.

(129) Demirdöven, N.; Khalil, M.; Golonzka, O.; Tokmakoff, A., Correlation effects in the two-dimensional vibrational spectroscopy of coupled vibrations. *The Journal of Physical Chemistry A* **2001,** *105* (34), 8025-8030.

(130) Technology, N. I. o. S. a. NIST Chemistry WebBook. http://webbook.nist.gov/chemistry/.

(131) Jameson, C. J.; Jameson, A. K., Effective collision cross sections for SF6 from nuclear magnetic relaxation. *The Journal of Chemical Physics* **1988,** *88*, 7448.

(132) Yardley, J., *Introduction to Molecular Energy Transfer*. Academic Press: New York, 1980.

(133) Gordon, R. G.; Klemperer, W.; Steinfeld, J. I., Vibratioal and Rotational Relaxation. *Annual Review of Physical Chemistry* **1968,** *19*, 215-250.

(134) Cheo, P. K.; Abrams, R. L., Rotational relaxation rate of CO2 Laser Levels. *Applied Physics Letters* **1969,** *14*, 47.

(135) DeZwaan, J.; Jonas, J., Density and temperature effects on motional dynamics of SF6 in the supercritical dense fluid region. *The Journal of Chemical Physics* **1975,** *63* (11), 4606-4612.

(136) Yamaguchi, T.; Matubayasi, N.; Nakahara, M., NMR Study on the Reorientational Relaxation in Supercritical Alcohols. *The Journal of Physical Chemistry A* **2004,** *108* (8), 1319-1324.

(137) Herzberg, G., *Infrared and Raman Spectroscopy of Polyatomic Molecules*. Van Nostrand: New York, 1954.

(138) Burshtein, A. I.; Temkin, S. I., *Spectroscopy of Molecular Rotation in Gases and Liquids*. Cambridge University Press: Cambridge, 1994.

(139) Hamm, P.; Zanni, M. T., *Concepts and Methods of 2D Infrared Spectroscopy*. Cambridge: 2011.

(140) Cheo, P. K.; Abrams, R. L., ROTATIONAL RELAXATION RATE OF CO2 LASER LEVELS. *Applied Physics Letters* **1969,** *14* (2), 47-49.

(141) Foster, J.; Miller, R. S., Fundamentals of High Pressure Combustion. In *High Pressure Processes in Chemical Engineering*, Lackner, M., Ed. ProcessEng Engineering GmbH: 2010; pp 53–75.

(142) Grubb, M. P.; Coulter, P. M.; Marroux, H. J. B.; Hornung, B.; McMullen, R. S.; Orr-Ewing, A. J.; Ashfold, M. N. R., Translational, rotational and vibrational relaxation dynamics of a solute molecule in a non-interacting solvent. *Nature Chemistry* **2016,** *8*, 1042.

(143) Kajimoto, O., Solvation in Supercritical Fluids: Its Effects on Energy Transfer and Chemical Reactions. *Chemical Reviews* **1999,** *99* (2), 355-390.

(144) DeSimone, J. M., Practical Approaches to Green Solvents. *Science* **2002,** *297* (5582), 799.

(145) Leitner, W., Supercritical Carbon Dioxide as a Green Reaction Medium for Catalysis. *Accounts of Chemical Research* **2002,** *35* (9), 746-756.

(146) Peach, J.; Eastoe, J., Supercritical carbon dioxide: a solvent like no other. *Beilstein The Journal of Organic Chemistry* **2014,** *10*, 1878-1895.

(147) Maddox, M. W.; Goodyear, G.; Tucker, S. C., Origins of Atom-Centered Local Density Enhancements in Compressible Supercritical Fluids. *The Journal of Physical Chemistry B* **2000,** *104* (26), 6248-6257.

(148) Heitz, M. P.; Bright, F. V., Probing the Scale of Local Density Augmentation in Supercritical Fluids: A Picosecond Rotational Reorientation Study. *The Journal of Physical Chemistry* **1996,** *100* (17), 6889-6897.

(149) Song, W.; Biswas, R.; Maroncelli, M., Intermolecular Interactions and Local Density Augmentation in Supercritical Solvation: A Survey of Simulation and Experimental Results. *The Journal of Physical Chemistry A* **2000,** *104* (30), 6924-6939.

(150) Wada, N.; Saito, M.; Kitada, D.; Smith, R. L.; Inomata, H.; Arai, K.; Saito, S., Local Excess Density about Substituted Benzene Compounds in Supercritical CO2 Based on FT-IR Spectroscopy. *The Journal of Physical Chemistry B* **1997,** *101* (50), 10918-10922.

(151) Tucker, S. C., Solvent Density Inhomogeneities in Supercritical Fluids. *Chemical Reviews* **1999,** *99* (2), 391-418.

(152) Tucker, S. C.; Maddox, M. W., The Effect of Solvent Density Inhomogeneities on Solute Dynamics in Supercritical Fluids: A Theoretical Perspective. *The Journal of Physical Chemistry B* **1998,** *102* (14), 2437-2453.

(153) Maddox, M. W.; Goodyear, G.; Tucker, S. C., Effect of Critical Slowing Down on Local-Density Dynamics. *The Journal of Physical Chemistry B* **2000,** *104* (26), 6266-6270.

(154) Heitz, M. P.; Maroncelli, M., Rotation of Aromatic Solutes in Supercritical CO2: Are Rotation Times Anomalously Slow in the Near Critical Regime? *The Journal of Physical Chemistry A* **1997,** *101* (33), 5852-5868.

(155) Goodyear, G.; Tucker, S. C., Glass-like behavior in supercritical fluids: The effect of critical slowing down on solute dynamics. *The Journal of Chemical Physics* **1999,** *111* (21), 9673-9677.

(156) Das, M.; Green, J. R., Critical fluctuations and slowing down of chaos. *Nature Communications* **2019,** *10* (1), 2155-2155.

(157) Urdahl, R. S.; Myers, D. J.; Rector, K. D.; Davis, P. H.; Cherayil, B. J.; Fayer, M. D., Vibrational lifetimes and vibrational line positions in polyatomic supercritical fluids near the critical point. *The Journal of Chemical Physics* **1997,** *107* (10), 3747-3757.

(158) Myers, D. J.; Shigeiwa, M.; Fayer, M. D.; Cherayil, B. J., Density dependent vibrational relaxation in supercritical fluids. *Chemical Physics Letters* **1999,** *313* (3), 592-599.

(159) Myers, D. J.; Shigeiwa, M.; Fayer, M. D.; Cherayil, B. J., Vibrational Lifetimes and Spectral Shifts in Supercritical Fluids as a Function of Density: Experiments and Theory. *The Journal of Physical Chemistry B* **2000,** *104* (10), 2402-2414.

(160) Schwarzer, D.; Lindner, J.; Vöhringer, P., OH-Stretch Vibrational Relaxation of HOD in Liquid to Supercritical D2O. *The Journal of Physical Chemistry A* **2006,** *110* (9), 2858-2867.

(161) Czurlok, D.; von Domaros, M.; Thomas, M.; Gleim, J.; Lindner, J.; Kirchner, B.; Vohringer, P., Femtosecond 2DIR spectroscopy of the nitrile stretching vibration of thiocyanate anions in liquid-to-supercritical heavy water. Spectral diffusion and libration-induced hydrogen-bond dynamics. *Physical Chemistry Chemical Physics* **2015,** *17* (44), 29776-29785.

(162) Simeoni, G. G.; Bryk, T.; Gorelli, F. A.; Krisch, M.; Ruocco, G.; Santoro, M.; Scopigno, T., The Widom line as the crossover between liquid-like and gas-like behaviour in supercritical fluids. *Nature Physics* **2010,** *6*, 503.

(163) Gallo, P.; Corradini, D.; Rovere, M., Widom line and dynamical crossovers as routes to understand supercritical water. *Nature Communications* **2014,** *5*, 5806.

(164) Xu, L.; Kumar, P.; Buldyrev, S. V.; Chen, S. H.; Poole, P. H.; Sciortino, F.; Stanley, H. E., Relation between the Widom line and the dynamic crossover in systems with a liquid–liquid phase transition. *Proceedings of the National Academy of Sciences of the United States of America* **2005,** *102* (46), 16558.

(165) Hestand, N. J.; Strong, S. E.; Shi, L.; Skinner, J. L., Mid-IR spectroscopy of supercritical water: From dilute gas to dense fluid. *The Journal of Chemical Physics* **2019,** *150* (5), 054505.

(166) Gorelli, F. A.; Bryk, T.; Krisch, M.; Ruocco, G.; Santoro, M.; Scopigno, T., Dynamics and Thermodynamics beyond the critical point. *Scientific Reports* **2013,** *3*, 1203.

(167) Brazhkin, V. V.; Fomin, Y. D.; Lyapin, A. G.; Ryzhov, V. N.; Tsiok, E. N.; Trachenko, K., ``Liquid-Gas'' Transition in the Supercritical Region: Fundamental Changes in the Particle Dynamics. *Physical Review Letters* **2013,** *111* (14), 145901.

(168) Fomin, Y. D.; Ryzhov, V. N.; Tsiok, E. N.; Brazhkin, V. V., Thermodynamic properties of supercritical carbon dioxide: Widom and Frenkel lines. *Physical Review E* **2015,** *91* (2), 022111.

(169) Bulanin, M. O.; Orlova, N. D., *Optical Spectroscopy* **1958,** *4*.

(170) Turrell, G. C.; Vu, H.; Vodar, B., Induced Q Branch in the Vibration-Rotation Spectrum of HCl Pressurized with Ar. *The Journal of Chemical Physics* **1960,** *33* (1), 315-316.

(171) Kwok, J.; Robinson, G. W., Spectroscopy in Liquid-Rare-Gas Solvents. Infrared Spectra of CH4 in Argon and of HCl in Xenon. *The Journal of Chemical Physics* **1962,** *36* (12), 3137-3140.

(172) Goldring, H.; Kwok, J.; Robinson, G. W., Infrared Spectra and Intensity Enhancements in Solutions of Hydrogen Halides in Liquid Xenon. *The Journal of Chemical Physics* **1965,** *43* (9), 3220-3228.

(173) Bratož, S.; Martin, M. L., Infrared Spectra of Highly Compressed Gas Mixtures of the Type HCl+X. A Theoretical Study. *The Journal of Chemical Physics* **1965,** *42* (3), 1051-1062.

(174) Robert, D.; Galatry, L., Calculation of infrared band shapes in liquid solutions of diatomic polar molecules in nonpolar solvents. *Chemical Physics Letters* **1967,** *1* (9), 399-403.

(175) Perez, J.; Velasco, S.; White, J. A.; Hernández, A. C., Infrared spectra of HCl, HBr and HI dissolved in liquid xenon. *Journal of Molecular Liquids* **1990,** *45* (1), 71-76.

(176) Medina, A.; Roco, J. M. M.; Calvo Hernández, A.; Velasco, S.; Bulanin, M. O.; Herrebout, W. A.; van der Veken, B. J., Vibration-rotation spectra of HCl in rare-gas liquid mixtures: Molecular dynamics simulations of Q-branch absorption. *The Journal of Chemical Physics* **2002,** *116* (12), 5058-5065.

(177) Medina, A.; Roco, J. M. M.; Calvo Hernández, A.; Velasco, S., Infrared Q-branch absorption and rotationally-hindered species in liquids. *The Journal of Chemical Physics* **2003,** *119* (10), 5176-5184.

(178) Medina, A.; Roco, J. M. M.; Calvo Hernández, A.; Velasco, S., Infrared spectral profiles in liquids and atom-diatom interactions. *The Journal of Chemical Physics* **2004,** *121* (13), 6353-6360.

(179) Medina, A.; Roco, J. M. M.; Hernández, A. C.; Velasco, S., Dynamical characterization of rotationally hindered species in liquids. *The Journal of Chemical Physics* **2005,** *123* (23), 234509.

(180) Bulanin, M. O.; Kerl, K.; Padilla, A.; Hernández, A. C.; Pérez, J., Infrared fundamental bandshape of HCl in fluid SF6: A modified-rotor description. *Physical Chemistry Chemical Physics* **2003,** *5* (2), 285-293.

(181) Padilla, A.; Pérez, J.; Kerl, K.; Bulanin, M. O., Vibration–rotation spectra of HCl solutions in SF6 at isochoric conditions. *Journal of Molecular Structure* **2003,** *651-653*, 561-566.

(182) Pérez, J.; Padilla, A.; Herrebout, W. A.; Van der Veken, B. J.; Hernández, A. C.; Bulanin, M. O., Experimental analysis and modified rotor description of the infrared fundamental band of HCl in Ar, Kr, and Xe solutions. *The Journal of Chemical Physics* **2005,** *122* (19), 194507.

(183) Padilla, A.; Pérez, J.; Herrebout, W. A.; Van der Veken, B. J.; Bulanin, M. O., A simulation study of the vibration–rotational spectra of HCl diluted in Ar: Rotational dynamics and the origin of the Q-branch. *Journal of Molecular Structure* **2010,** *976* (1), 42-48.

(184) Padilla, A.; Pérez, J., Non-Markovian near-infrared Q branch of HCl diluted in liquid Ar. *The Journal of Chemical Physics* **2013,** *139* (8), 084505.

(185) Padilla, A.; Pérez, J., Mixed classical-quantum simulation of vibro-rotational absorption spectra of HCl diluted in dense Ar: Anisotropic interaction and the Q-branch. *Journal of Molecular Spectroscopy* **2015,** *316*, 22-31.

(186) Herzberg, G.; Herzberg, L., Rotation-Vibration Spectra of Diatomic and Simple Polyatomic Molecules with Long Absorbing Paths VI. The Spectrum of Nitrous

Oxide (N2O) below 1.2μ. *The Journal of Chemical Physics* **1950,** *18* (12), 1551-1561.

(187) Roberts, S. T.; Ramasesha, K.; Tokmakoff, A., Structural rearrangements in water viewed through two-dimensional infrared spectroscopy. *Accounts of Chemical Research* **2009,** *42* (9), 1239-1249.

(188) Schmitz, A. J.; Hogle, D. G.; Gai, X. S.; Fenlon, E. E.; Brewer, S. H.; Tucker, M. J., Two-Dimensional Infrared Study of Vibrational Coupling between Azide and Nitrile Reporters in a RNA Nucleoside. *The Journal of Physical Chemistry. B* **2016,** *120* (35), 9387-9394.

(189) Kim, Y. S.; Hochstrasser, R. M., Chemical exchange 2D IR of hydrogen-bond making and breaking. *Proceedings of the National Academy of Sciences of the United States of America* **2005,** *102* (32), 11185.

(190) Chieffo, L.; Amsden, J.; Shattuck, J.; Hong, M. K.; Ziegler, L.; Erramilli, S., Femtosecond infrared vibrational lifetime measurements of the anesthetic gas nitrous oxide in membranes." arXiv:0705.0835v1 *Biophysical Review Letters* **2006,** *1*, 309-316.

(191) Dong, A.; Huang, P.; Zhao, X. J.; Sampath, V.; Caughey, W. S., Characterization of sites occupied by the anesthetic nitrous oxide within proteins by infrared spectroscopy. *Journal of Biological Chemistry* **1994,** *269* (39), 23911-23917.

(192) Chieffo, L. R.; Shattuck, J. T.; Pinnick, E.; Amsden, J. J.; Hong, M. K.; Wang, F.; Erramilli, S.; Ziegler, L. D., Nitrous Oxide Vibrational Energy Relaxation Is a

Probe of Interfacial Water in Lipid Bilayers. *The Journal of Physical Chemistry B* **2008,** *112* (40), 12776-12782.

(193) Gorga, J. C.; Hazzard, J. H.; Caughey, W. S., Determination of anesthetic molecule environments by infrared spectroscopy: I. Effects of solvating molecule structure on nitrous oxide spectra. *Archives of Biochemistry and Biophysics* **1985,** *240* (2), 734-746.

(194) Kubo, R., A Stochastic Theory of Line Shape. In *Advances in Chemical Physics*, John Wiley & Sons, Inc.: 2007; pp 101-127.

(195) Kwak, K.; Park, S.; Finkelstein, I. J.; Fayer, M. D., Frequency-frequency correlation functions and apodization in two-dimensional infrared vibrational echo spectroscopy: A new approach. *The Journal of Chemical Physics* **2007,** *127* (12), 124503.

(196) Howdle, S. M.; Bagratashvili, V. N., The effects of fluid density on the rotational Raman spectrum of hydrogen dissolved in supercritical carbon dioxide. *Chemical Physics Letters* **1993,** *214* (2), 215-219.

(197) Shattuck, J. T.; Schneck, J. R.; Chieffo, L. R.; Erramilli, S.; Ziegler, L. D., Dispersed Three-Pulse Infrared Photon Echoes of Nitrous Oxide in Water and Octanol. *The Journal of Physical Chemistry B* **2013,** *117* (49), 15774-15785.

(198) Aubuchon, C. M.; Rector, K. D.; Holmes, W.; Fayer, M. D., Nitro group asymmetric stretching mode lifetimes of molecules used in energetic materials. *Chemical Physics Letters* **1999,** *299* (1), 84-90.

(199) Cottrell, T. L.; McCoubrey, J. C., *Molecular Energy Transfer in Gases*. Butterworths: London, 1961.

(200) Yardley, J. T.; Moore, C. B., Vibrational Energy Transfer in Methane. *The Journal of Chemical Physics* **1968,** *49* (3), 1111-1125.

(201) Flynn, G. W.; Parmenter, C. S.; Wodtke, A. M., Vibrational Energy Transfer. *The Journal of Physical Chemistry* **1996,** *100* (31), 12817-12838.

(202) Kenkre, V. M.; Tokmakoff, A.; Fayer, M. D., Theory of vibrational relaxation of polyatomic molecules in liquids. *The Journal of Chemical Physics* **1994,** *101* (12), 10618-10629.

(203) Polanyi, J. C.; Woodall, K. B., Mechanism of Rotational Relaxation. *The Journal of Chemical Physics* **1972,** *56* (4), 1563-1572.

(204) Gordon, R. G.; Klemperer, W.; Steinfeld, J. I., Vibrational and Rotational Relaxation. *Annual Review of Physical Chemistry* **1968,** *19* (1), 215-250.

(205) Holmes, R.; Jones, G. R.; Lawrence, R., Rotational Relaxation in Carbon Dioxide and Nitrous Oxide. *The Journal of Chemical Physics* **1964,** *41* (9), 2955-2956.

(206) Jacobs, R. R.; Pettipiece, K. J.; Thomas, S. J., Rotational relaxation rate constants for CO2. *Applied Physics Letters* **1974,** *24* (8), 375-377.

(207) Hinchen, J. J.; Hobbs, R. H., Rotational relaxation studies of HF using ir double resonance. *The Journal of Chemical Physics* **1976,** *65* (7), 2732-2739.

(208) Nicolaisen, H.-W.; Mäder, H., Rotational relaxation rates for the J = 0–1 transition of N2O by self-collisions and foreign gas collisions. *Molecular Physics* **1991,** *73* (2), 349-358.

(209) Steinfeld, J. I.; Klemperer, W., Energy-Transfer Processes in Monochromatically Excited Iodine Molecules. I. Experimental Results. *The Journal of Chemical Physics* **1965,** *42* (10), 3475-3497.

(210) Park, C., Rotational Relaxation of N2 Behind a Strong Shock Wave. *Journal of Thermophysics and Heat Transfer* **2004,** *18* (4), 527-533.

(211) Holmes, R.; Jones, G. R.; Lawrence, R., Vibrational-rotational-translational energy exchange in some polyatomic molecules. *Transactions of the Faraday Society* **1966,** *62* (0), 46-53.

(212) Holmes, R.; Jones, G. R.; Pusat, N., Combined viscothermal and thermal relaxation in polyatomic gases. *Transactions of the Faraday Society* **1964,** *60* (0), 1220-1229.

CURRICULUM VITAE